

2008

# Intraocular pressure (IOP) passive sensor modeling, design, fabrication and measurement

Haibo Cao

*Iowa State University*

Follow this and additional works at: <https://lib.dr.iastate.edu/etd>

 Part of the [Electrical and Computer Engineering Commons](#)

## Recommended Citation

Cao, Haibo, "Intraocular pressure (IOP) passive sensor modeling, design, fabrication and measurement" (2008). *Graduate Theses and Dissertations*. 10899.

<https://lib.dr.iastate.edu/etd/10899>

This Dissertation is brought to you for free and open access by the Iowa State University Capstones, Theses and Dissertations at Iowa State University Digital Repository. It has been accepted for inclusion in Graduate Theses and Dissertations by an authorized administrator of Iowa State University Digital Repository. For more information, please contact [digirep@iastate.edu](mailto:digirep@iastate.edu).

**Intraocular pressure (IOP) passive sensor modeling, design, fabrication and  
measurement**

by

**Haibo Cao**

A dissertation submitted to the graduate faculty  
in partial fulfillment of the requirements for the degree of  
**DOCTOR OF PHILOSOPHY**

Major: Electrical Engineering

Program of Study Committee:  
Robert J. Weber, Major Professor  
Mani Mina  
Gary L. Tuttle  
Akhilesh Tyagi  
Stephen B. Vardeman

Iowa State University

Ames, Iowa

2008

Copyright © Haibo Cao, 2008. All rights reserved.

*To My Parents and Siyuan*

*To My Grandfather Haiyuan, Who Lost His Vision for 5 Years Because of Glaucoma*

## TABLE OF CONTENTS

LIST OF FIGURES	v
LIST OF TABLES	viii
ABSTRACT	ix
CHAPTER 1. INTRODUCTION	1
1.1 Background	1
1.2 Literature Review	2
Inductive Coupled Telemetry	2
Wired Sensing Techniques	6
Other Techniques	6
1.3 Project Motivation	7
1.4 Project Accomplishment	7
1.5 Organization of This Thesis	9
CHAPTER 2. INTRAOCULAR PRESSURE (IOP) SENSOR MODELING	10
2.1 Deformation of a Circular Diaphragm [16]	10
2.1.1 Stress and Strain	10
2.1.2 Relationships Between Stress and Strain	12
2.1.3 Deformation of a Circular Diaphragm	14
2.2 Capacitance Calculation of a Circular Diaphragm by Method of Moments (MOM)	17
2.2.1 Method of Moments (MOM)	17
2.2.2 Circular Ring of Charge Modeling	18
2.2.3 Capacitance Calculation	20
CHAPTER 3. INTRAOCULAR PRESSURE (IOP) SENSOR DESIGN	24
3.1 Structure Consideration	24
3.1.1 Membrane	24
3.1.2 Inductor	25
3.2 Material Consideration	26
3.3 Size and Dimension Consideration	31
3.4 Mask Consideration	36
3.5 Fabrication Consideration	44
3.5.1 Residual Stress	44
3.5.2 HF Vapor Sacrificial Etching	45
3.5.3 Critical Point Drying (CPD)	47
CHAPTER 4. INTRAOCULAR PRESSURE (IOP) SENSOR FABRICATION	50
4.1 Introduction	50
4.2 Insulation Layer ( $\text{Si}_3\text{N}_4$ ) Deposition and Pattern	52
4.3 Sacrificial Layer (PSG) Deposition and Pattern	54
4.4 Structure Layer (Phos-poly) Deposition and Pattern	56
4.5 HF Vapor Sacrificial Etching	62
4.6 Critical Point Drying (CPD)	63
4.7 Cavity Sealing ( $\text{SiO}_2$ )	69

4.8 Metal Contact (Aluminum)	72
CHAPTER 5. INTRAOCULAR PRESSURE (IOP) SENSOR MEASUREMENT	77
5.1 Study of Detector and Sensor Coil	77
5.2 Measurement Setup	85
5.3 Probe Measurement	87
5.4 Remote Measurement	91
CHAPTER 6. FUTURE WORK AND CONCLUSION	103
6.1 Discussion	103
Biocompatible Coating	103
Calibration	103
Implantation	103
Size	104
6.2 Contributions	105
6.3 Future Work	106
Fabrication Control	107
Parasitic Model	107
Improved Measurement	107
Detector Circuitry	108
Body Environment	108
APPENDIX A. METHOD OF MOMENTS MATLAB CODE	110
APPENDIX B. INTRAOCULAR PRESSURE (IOP) SENSOR FABRICATION FLOW	113
BIBLIOGRAPHY	118
ACKNOWLEDGEMENTS	123

## LIST OF FIGURES

Fig. 1. Schematic presentation of a system for inductive coupled telemetry of a passive IOP device.	4
Fig. 2. Stress-strain curve.	13
Fig. 3. An edge-fixed circular diaphragm.	15
Fig. 4. The deformation for a polysilicon diaphragm under 760mmHg.	16
Fig. 5. The equivalent model of a diaphragm above a ground due to Image Theory.	18
Fig. 6. Circular ring of charge with a small but finite skin depth.	19
Fig. 7. The MOM model for this project.	20
Fig. 8. Comparison of the capacitance calculation between the MOM (MATLAB) algorithm and the HFSS simulation for a flat circular diaphragm.	23
Fig. 9. A proposed IOP sensor membrane array with inductor attaching pads.	26
Fig. 10. Capacitance calculation for a flat circular membrane with different radii and different materials.	28
Fig. 11. Q-factor for a single circular membrane with different radii.	33
Fig. 12. The deformation and charge density for a Phos-poly diaphragm.	35
Fig. 13. 8-layer mask design for IOP sensor.	37
Fig. 14. Alignment marker A.	39
Fig. 15. Alignment marker B.	40
Fig. 16. Alignment marker A&B.	41
Fig. 17. Mask 1-4 synthesized into the first mask.	42
Fig. 18. Mask 5-8 synthesized into the second mask.	43
Fig. 19. Polysilicon cantilever with different type of stresses.	45
Fig. 20. The collapse of a thin cantilever beam due to stiction.	47
Fig. 21. Carbon dioxide supercritical drying.	49
Fig. 22. Substrate electrode defined by LPCVD $\text{Si}_3\text{N}_4$ .	53
Fig. 23. Sacrificial layer defined by LPCVD PSG.	55
Fig. 24. Polysilicon membrane layer stack up.	56
Fig. 25. Phos-Poly membrane array with PSG etching channels.	59
Fig. 26. One Phos-Poly membrane with PSG etching channels.	60
Fig. 27. Surface portfolio of one Phos-Poly membrane taken by confocal microscope.	61
Fig. 28. A 3D view of one Phos-Poly membrane taken by confocal microscope.	62
Fig. 29. Released Phos-Poly membrane.	64
Fig. 30. Released Phos-Poly membrane array.	65
Fig. 31. Unreleased polysilicon membrane with PSG underneath.	65
Fig. 32. Broken Phos-Poly membranes with no PSG underneath.	67
Fig. 33. Released Phos-Poly membrane taken by confocal microscope.	68
Fig. 34. A 3D view of released Phos-Poly membrane taken by confocal microscope.	69
Fig. 35. Sealed membranes.	71
Fig. 36. One membrane after Al pattern.	73
Fig. 37. Membrane array after Al pattern.	74
Fig. 38. IOP sensor fabrication flow.	76
Fig. 39. Detector #1.	78

Fig. 40. Detector #2.	78
Fig. 41. Detector #3.	79
Fig. 42. Sensor #1.	80
Fig. 43. Sensor #2.	80
Fig. 44. Sensor #3.	81
Fig. 45. Sensor #4.	81
Fig. 46. Measurement for different sensors using detector #1 (distance=1mm).	83
Fig. 47. Measurement for detector #1 and sensor #3 with different distances.	84
Fig. 48. Measurement for sensor #3 with different detectors (distance=1mm).	84
Fig. 49. Measurement for detector #3 and sensor #1 and #3 at the same height.	85
Fig. 50. A capacitor array integrated with a 6 turn enamel coil.	86
Fig. 51. Diagram of the variable pressure system for IOP sensor measurement.	86
Fig. 52. The variable pressure system setup.	87
Fig. 53. Cascade ACP40-m-GSG-100 probe tip.	88
Fig. 54. A 2 by 2 membrane array.	88
Fig. 55. The probe measurement and MOM calculation (without parasitics) for a 2 by 2 membrane array.	89
Fig. 56. Probe measurement of an array of 32 membranes with a 0403 1.9mH high-Q inductor (Coilcraft Qmin=40).	90
Fig. 57. An array of 11 membranes (7 malfunctioned).	90
Fig. 58. Probe measurement of an array of 11 membranes (7 malfunctioned).	91
Fig. 59. IOP sensor is detected by a coil detector with high permeability half cylinder core.	92
Fig. 60. The measurement return loss of a coil detector detecting an IOP sensor with the sensing distance is almost 0.	93
Fig. 61. The measurement phase of a coil detector detecting an IOP sensor with the sensing distance is almost 0.	94
Fig. 62. The measurement phase of a coil detector detecting an IOP sensor with the sensing distance is 1mm.	94
Fig. 63. The measurement phase of a coil detector detecting an IOP sensor with the sensing distance is 1.5mm.	95
Fig. 64. The measurement phase of a coil detector detecting an IOP sensor with the sensing distance is 2.77mm.	95
Fig. 65. The measurement phase of a coil detector detecting an IOP sensor with the sensing distance is 3.405mm.	96
Fig. 66. The measurement phase of a coil detector detecting an IOP sensor with the sensing distance is 4.04mm.	96
Fig. 67. The telemetry configuration using a secondary resonator.	98
Fig. 68. The telemetry configuration using a secondary resonator in realistic daily use.	99
Fig. 69. Measurement setup of the telemetry configuration using a secondary resonator.	100
Fig. 70. The measurement phase (fitting) of a primary coil detector detecting an IOP sensor by using a secondary resonator with the sensing distance is 1cm.	101
Fig. 71. The measurement phase (fitting) of a primary coil detector detecting an IOP sensor by using a secondary resonator with the sensing distance is 1.5cm.	102
Fig. 72. A proposed IOP sensor structure.	105

Fig. 73. The remote measurement with sensor #1 immersed into a small portion of water.

109

**LIST OF TABLES**

Table 1. Summary of developing Inductive Coupled Telemetry Passive IOP Devices.	5
Table 2. Mechanical properties of polysilicon and selected materials.	30
Table 3. Electrical and mechanical properties for a single circular membrane with different radii and cavity heights.	32
Table 4. Phos-poly deposition time.	56
Table 5. Detector Details.	77
Table 6. Sensor Kit Details.	79
Table 7. Measurements of an IOP sensor with 32 membranes and 6 turn AWG38 enamel coil, the detector is a coil detector with high permeability half cylinder core.	93

## ABSTRACT

This work describes a miniaturized implantable passive pressure sensor and a remote sensing technique for pressure measurement. The sensor device consists of a capacitor array and a coil inductor, which form a high-Q LC type resonator. The capacitor array, which is also membrane structures, is fabricated by surface micromachining technique. The deflection of the membrane depends on the pressure applied to it. The higher the pressure, the larger the deflection, and the larger the capacitor is. This change of the capacitance will also change the resonant frequency of the LC resonator, and it can be detected by various types of coil detectors. One detecting prototype using a secondary resonator is proposed in this work, the sensing distance can be improved to about 1.5cm, which is larger than most of the publication work in this area. This large sensing distance will allow the detector to be integrated into a spectacles frame. It has more accurate results than prior works. The sensor itself can be smaller than 1.5mm×1.5mm×1mm, and after biocompatible material coating, the sensor can be implanted into the human body. This sensor was particularly designed for intraocular pressure (IOP) measurement. It can provide multiple and continuous IOP readouts under everyday conditions, which is desired to monitor any fluctuations of IOP, and it is very useful for glaucoma diagnosis. The sensor can also be implanted into any other part of human body to remotely measure any pressure of a tissue or inside a chamber, e.g. the pulmonary artery.

## CHAPTER 1. INTRODUCTION

### 1.1 Background

Glaucoma is a category of eye diseases characterized by an increase in intraocular pressure (IOP). Worldwide, an estimated 67 million people suffer from glaucoma [1], and in the United States, over 3 million people have this disease. Glaucoma is often referred to as the “silent theft of sight,” because most types typically cause no pain and no symptoms at the beginning. For this reason, glaucoma often progresses undetected until the optic nerve already has been irreversibly damaged, with varying degrees of permanent vision loss. Normal IOP is in the range of 10-21mmHg (millimeters of mercury) [2], [3]. Among glaucoma patients, most of the cases the IOP increase to above 30mmHg, and some even higher than 100mmHg. The conventional way to measure the IOP relies of the use of applanation and non-contact tonometry, which measures the external deformation of the cornea. However, the reliability of tonometry is affected by fluctuations of the IOP during different days, and the measurement is always under artificial and expensive conditions of hospitalization or the other clinical settings. Multiple or continuous IOP measurements under everyday conditions are desirable to diagnose and monitor those fluctuations, and an implantable device is also desirable for the people who are not able to visit the ophthalmologist very frequently.

## 1.2 Literature Review

Continuous IOP sensing devices can be categorized by their sensing techniques as Inductive Coupled Telemetry, Wired Sensing Techniques and other techniques. For some of those techniques, the device can become either an active or passive sensing device. The following discussion will only focus on passive type devices due to their small size and low power consumption.

### Inductive Coupled Telemetry

Among the above techniques, the Inductive Coupled Telemetry Passive Devices have gained more attention due to their low power consumption, low noise, high sensitivity and good long-term stability [4]. One implantable device often consists of thin membranes (capacitive) and metal inductor. One side of the membranes is a vacuum cavity with the other side exposed to the pressure to be measured, the membranes deform due to different pressure and give different capacitance. The inductor is excited by an external coil (reader or detector) which can be integrated into the spectacles. The resonant frequency (Eq. 1) of the LC resonator changes in response to variations of pressure, and this change can be monitored by measuring the impedance of the external coil (Fig. 1). Collins developed the earliest passive LC type sensor [5], and up to now several groups have been working toward to the development of this type of device. This type of sensor is also the focus of this work.

$$f_0 = \frac{1}{2\pi} \frac{1}{\sqrt{LC}}. \quad (1)$$

Rosengren *et al.* [6] used 6 to 12 turns 50um gold wire coil with diameter of 5mm and bonded to the capacitive element, which is a silicon diaphragm. After encapsulating in

silicone, the overall size became 5mm diameter×2mm thickness. It has a sensitivity of 4mV/mmHg and the sensing distance was reported as a few millimeters. Puers, Coosemans *et al.* [7], [8] fabricated the inductor by electrodeposition of copper on a pressure sensitive diaphragm, the size was reported as 4mm×4mm×1mm and the sensor can be excited at 20-40MHz. The mutual coil separation distance was reported as 7.5mm. Abita *et al.* [9] bonded a wire coil to a silicon diaphragm with a thin layer of gold deposited. The sensor has a resonant frequency about 122MHz and a sensitivity of 6.1kHz/mmHg, no detailed sensing distance was reported. Akar *et al.* [10] fabricated an absolute capacitive pressure sensor with an electroplated gold coil inside the sealed cavity of the capacitor, the sensor has a size of 2.6mm×1.6mm, and the pressure range and sensitivity are reported as 0-50mmHg and 120kHz/mmHg, respectively. The sensing distance was only 2mm due to the low-Q for the spiral inductor. Chen *et al.* [11] reported an implantable sensor with Ti/Au spirals and Parylene diaphragm for biocompatible purpose. The sensor has a sensitivity of 1140kHz/mmHg and a size of 4mm×1mm. However the sensing distance is less than 2mm due to the low-Q of the resonator. Petersen *et al.* [12] reported a relatively easy method to fabricate this type of sensor. They electrodeposited metal spirals on a thin layer biocompatible material such as silicon or polyimide and used an assembly jig to fold the diaphragms and bonded them together. However, no detailed measurement result was reported from this work. The Inductive Coupled Telemetry Passive Device works are summarized in Table I. Most of those works suffer from weak coupling between the external coil and the sensor due to the low Q-factor of the LC resonator. This is also the main research focus of this work to improve the sensing distance and accuracy for LC type passive pressure sensors.

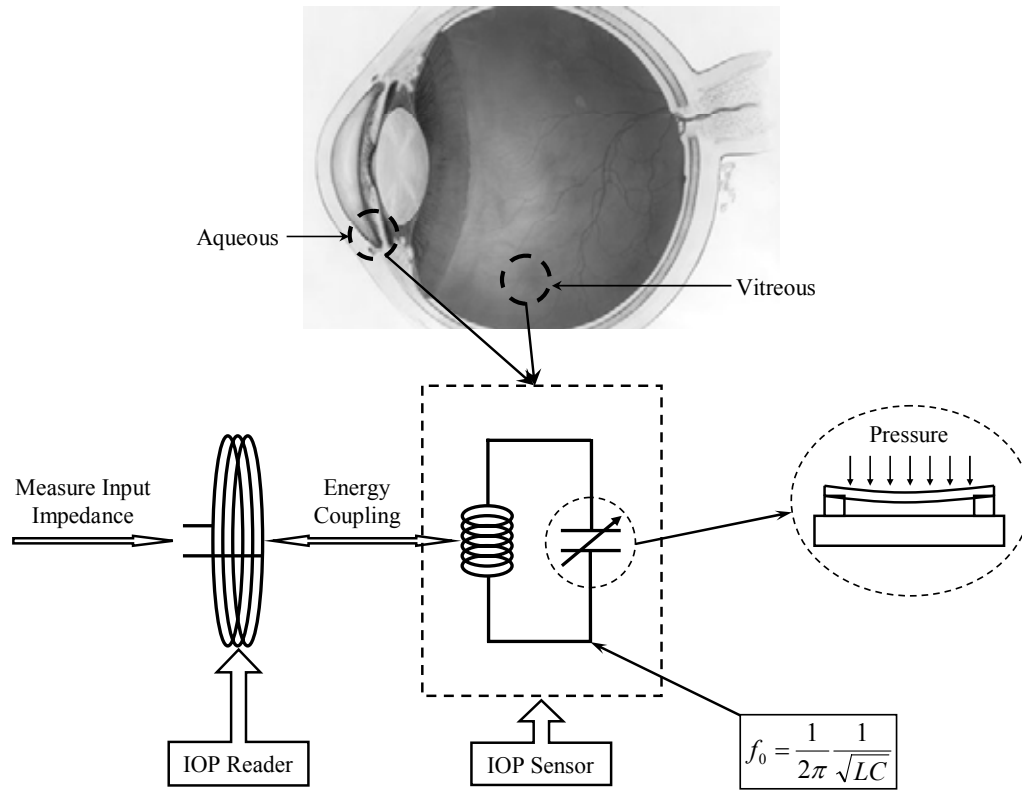


**Fig. 1. Schematic presentation of a system for inductive coupled telemetry of a passive IOP device\* .**

\* Eye diagram source: [http://www.nysoa.org/index.php?page\\_id=131](http://www.nysoa.org/index.php?page_id=131)

Reference	Membrane	Inductor	Resonant Frequency (MHz)	Pressure Sensitivity (kHz/mmHg)	Sensor Size	Q Factor	Sensing Distance
[6]	Silicon	Gold Wire Coil	40	1	5mm diameter ×2mm	NA	Few mm
[7], [8]	Silicon	Electroplated copper spiral	20-40	NA	4×4×0.7 mm <sup>3</sup>	NA	NA
[9]	Silicon/ thin gold	Coil	~122	~6.1	4.5mm diameter	NA	NA
[10]	P+ Silicon	Electroplated gold spiral	70-76	120	2.6mm× 1.6mm	<8	<2mm
[11]	Parylene/ titanium/ gold/parylene	titanium/ gold spiral	150	1140	4mm× 1mm	~5	2mm

**Table 1. Summary of developing Inductive Coupled Telemetry Passive IOP Devices.**

## Wired Sensing Techniques

Walter *et al.* [13] reported a way using a small sensitive piezoresistive strain gauge element mounted in a curved semirigid holder, which serves to position the planar strain gauge in contact with the eyeball surface. The deformation of the strain gauge element due to its contact with the eyeball produces an output signal corresponding to the IOP, this signal was recorded by a monitoring circuitry by wire leads from the strain gauge through the lower eyelid. Similar to the above work, Leonardi *et al.* [14] built a soft contact lens embedded with a microfabricated strain gauge in a Wheatstone bridge configuration. The gauge was placed on the cornea of the eye, and behaves like a partial spherical shell subjected to a uniform edge moment. The sensitivity of 8.36 $\mu$ V/mmHg was reported by testing the sensor on porcine eyes.

For these wired sensing techniques, the accuracy of the pressure measurement is affected by rigidity, eye size, and other physical condition such as eye movement and lid pressure.

## Other Techniques

Chen *et al.* [15] fabricated a passive pressure transducer which is completely mechanical. A 1mm radius spiral was fabricated and sealed in a parylene-C polymer tube and pressurized to 1 atmosphere internally. The outside pressure on the tube causes the tube to elongate circumferentially, and the tip rotation of the spiral was optically tracked externally. For this design, the location of the external sensing optics to the implant will be crucial in the measurement.

### 1.3 Project Motivation

It is a primary object of this project to provide an implantable and miniaturized Inductive Coupled Telemetry passive pressure sensor with improved sensing distance to continuously measure the IOP. The sensor should have a high Q factor in order to reduce the electrical energy loss. The sensor should also be able to measure the pressure of a tissue, fluid or gas inside a human chamber.

It is another object of this project to provide a remote telemetry technique which facilitates continuous and stable measurement of the IOP under everyday conditions without interfering with individual activity or changing the IOP.

It is another object of this project to develop an algorithm which is able to determine both mechanical deformation and electrical charge distribution and capacitance of a circular membrane structure or array.

It is another object of this project to build a lab set-up cooperating with microwave testing equipments such as a Network Analyzer and probe station.

Other objects also include minimizing the sensor size, improving the sensing sensitivity and reducing manufacture cost.

### 1.4 Project Accomplishment

This project provides detailed solutions for the Inductive Coupled Telemetry passive pressure sensor modeling, design, fabrication and measurement. The sensor consists of a capacitor array and a coil inductor, which form a high-Q LC resonator. The capacitor array is fabricated by a surface micromachining technique and is bonded to a small coil inductor using high conductivity epoxy. The capacitor array is a membrane structure with a vacuum cavity

inside, and having electrode plates deformed due to any pressure changing in the outside environment. The resonant frequency can be detected by multiple types of reader sensors such as a high permeability core coil reader, or regular coil reader. The sensor itself can be detected at a range of 4mm, but using a secondary resonating coil, the sensing distance can be improved to 1.5cm.

The size of the sensor in this invention can be reduced to  $1.5\text{mm}\times 1.5\text{mm}\times 1\text{mm}$ , and can be reduced more by reducing the capacitor array elements and the size of the inductor coil. After using a biocompatible material coating, the sensor is implantable in the anterior chamber, posterior chamber or vitreous body of human eyes. The secondary resonator can be integrated into a contact lens and the coil reader can be integrated into a spectacles frame. This sensing system has the ability to provide continuous and stable measurement of the IOP without influencing of the individual activity over a large sensing distance.

The Method of Moments (MOM) algorithm provides a fast and accurate way to calculate the capacitance of membrane structures with any deformation (pressure), it avoids the singularity problem and the need to use an expensive microwave modeling package such as Ansoft Corporation's HFSS<sup>TM</sup>. This design provides a low cost and high performance solution for a passive IOP sensor. The fabrication techniques used in this work can be done in most silicon facility research centers. Considerations have been paid to low energy loss and to high Q-factor to improve the remote sensing distance. The fabrication process first provides a novel technique using HF vapor for sacrificial release of the suspended membrane structures [15]. As the surface layers are pile up, difficulty rises in step coverage for device layer and photoresist spinning. The design flow put careful attention on MEMS layer coverage, and the mask design compensates for all the undercut which could happen during the processing.

Many experiments have been conducted in the lab for the best fabrication profile, such as photoresist coverage and etching.

The pressure sensor has been tested in a variable pressure environment from 0mmHg-80mmHg (differential to the normal atmosphere pressure). A HP Network Analyzer was used to read the input impedance of the coil reader. In addition, different type of coil readers were also tested and studied for this system, detailed results are shown in the following chapters.

## 1.5 Organization of This Thesis

Chapter 2 of this thesis covers the mechanical and electrical models for a circular membrane structure, and the algorithm used to calculate the capacitance using Method of Moments (MOM). Chapter 3 covers the design details for the IOP sensor. Chapter 4 covers the fabrication details of the IOP sensors, which include layer deposition, sacrificial etching, critical point drying, cavity sealing and metal contact. Chapter 4 covers the measurement set-up and results for testing the IOP sensor with various types of detectors. It also introduces the improved sensing telemetry using a secondary resonator. Chapter 5 is the conclusion of this project and contains future work suggestions.

## **CHAPTER 2. INTRAOCULAR PRESSURE (IOP) SENSOR MODELING**

The pressure sensing element for the present IOP sensor is circular diaphragm or membrane. The structure deforms due to pressure change, and gives different capacitance accordingly. Both mechanical and electrical properties are considered during the modeling process in this project. This chapter discusses how a circular diaphragm deforms under a uniform load condition and how the capacitance is calculated by using Method of Moments (MOM). In the present invention, this variable capacitor design presents a challenge to calculate the capacitance and the rate of capacitance change in respect to the pressure applied. This procedure used induces a small amount of distance from the bottom surface of the plate to the electrical charges to avoid any singularity problem. The Image Theory and Method of Moments (MOM) are used in this invention to derive an algorithm, which has been implemented into MATLAB. The calculated results agree with the simulations from HFSS very well, the charge density can also be obtained from this algorithm.

### **2.1 Deformation of a Circular Diaphragm [16]**

#### **2.1.1 Stress and Strain**

Stress and strain are concepts of paramount importance to a comprehension of the mechanics of materials. Stress is a measure of the average amount of force exerted per unit area. It is a measure of the intensity of the total internal forces acting within a body across imaginary internal surfaces, as a reaction to external applied forces and body forces. In general, stress is expressed as

$$\sigma = \frac{F}{A}, \quad (2)$$

where  $\sigma$  is the average stress and  $F$  is the force acting of area  $A$ .

Strain is the geometrical measure of deformation representing the relative displacement between particles in the material body, i.e. a measure of how much a given displacement differs locally from a rigid-body displacement.

The small displacements of points in a deformed body will be resolved into components  $u$ ,  $v$ , and  $w$  parallel to the  $x$ -,  $y$ -, and  $z$ -axes. Therefore the normal strain in the  $x$ -direction is

$$\varepsilon_x = \lim_{\Delta x \rightarrow 0} \frac{\Delta u}{\Delta x} = \frac{\partial u}{\partial x}. \quad (3)$$

Similarly, the normal strains in the  $y$ - and  $z$ -directions are, respectively,

$$\varepsilon_y = \frac{\partial v}{\partial y}, \quad (4)$$

and

$$\varepsilon_z = \frac{\partial w}{\partial z}. \quad (5)$$

The three-dimensional strain components relationships can be derived as (Cauchy's equations)

$$\begin{cases} \varepsilon_x = \frac{\partial u}{\partial x} & \gamma_{xy} = \frac{\partial u}{\partial y} + \frac{\partial v}{\partial x} \\ \varepsilon_y = \frac{\partial v}{\partial y} & \gamma_{yz} = \frac{\partial v}{\partial z} + \frac{\partial w}{\partial y} \\ \varepsilon_z = \frac{\partial w}{\partial z} & \gamma_{zx} = \frac{\partial w}{\partial x} + \frac{\partial u}{\partial z} \end{cases}, \quad (6)$$

and the strain tensor is given by

$$\begin{pmatrix} \varepsilon_x & \gamma_{xy} & \gamma_{xz} \\ \gamma_{yx} & \varepsilon_y & \gamma_{yz} \\ \gamma_{zx} & \gamma_{zy} & \varepsilon_z \end{pmatrix}, \quad (7)$$

which is a symmetric tensor since

$$\begin{cases} \gamma_{xy} = \gamma_{yx} \\ \gamma_{yz} = \gamma_{zy} \\ \gamma_{zx} = \gamma_{xz} \end{cases} \quad (8)$$

### 2.1.2 Relationships Between Stress and Strain

The relationship between stress and strain can be graphically represented in Fig. 2 as a stress and strain curve – stress, derived from measuring the load applied on the sample, and strain, derived from measuring the deformation of the sample, i.e. elongation, compression, or distortion. Most structural materials have an initial region of the stress-strain curve in which the material behaves both elastically and linearly up to a well defined yield point (point 2). Before this point, the linear elasticity is a highly significant property of many engineering materials. For this portion, the stress is directly proportional to the strain:

$$\sigma = E\varepsilon. \quad (9)$$

The above relationship is known as Hooke's Law. The constant  $E$  is called the modulus of elasticity, or Young's modulus. As  $\varepsilon$  is a dimensionless quantity,  $E$  has the units of  $\sigma$ . The present project is interested in this linear elastic region where the material behaves elastically with pressure. Prior to the yield point the material will deform elastically and will return to its original shape when the applied stress is removed. Once the yield point is passed some fraction of the deformation will be permanent and non-reversible, one material can be either permanently deformed or broken.

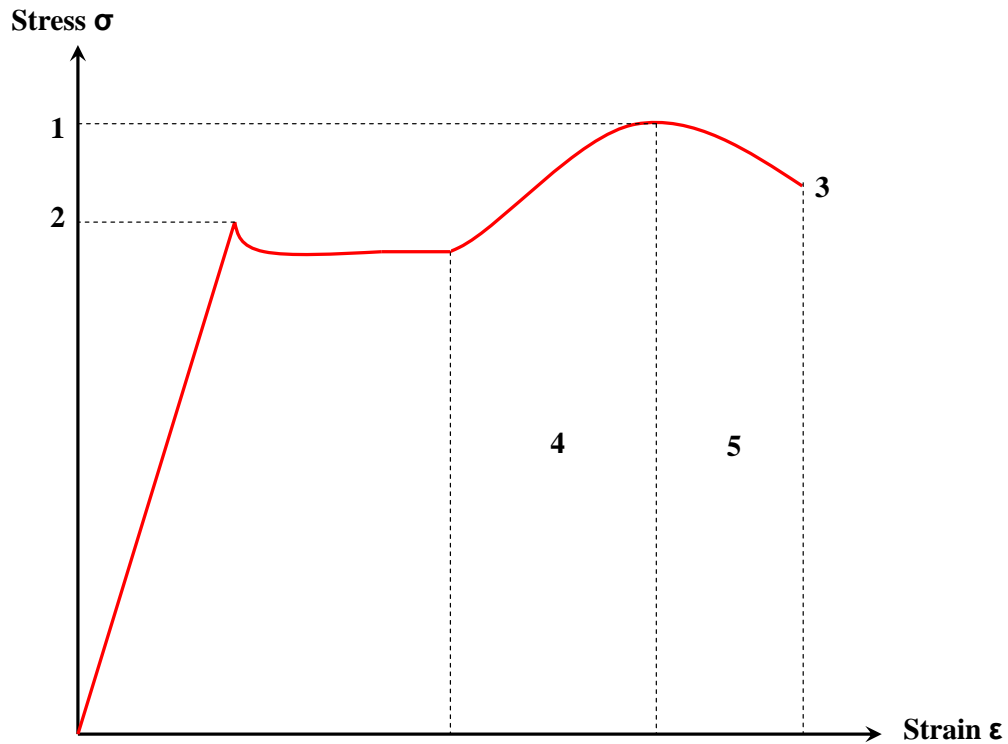


**Fig. 2. Stress-strain curve.**

In this elastic range, the ratio of the lateral strain to the axial strain is a constant and known as Poisson's ratio, denoted by  $\nu$ :

$$\nu = -\frac{\text{lateral strain}}{\text{axial strain}}, \quad (10)$$

where the minus sign indicates that the lateral strain is in the sense opposite to that of the axial strain.

If we assume the desired characteristics of a material body are elastic and homogeneous, the material can be specified by the above two constants: Young's modulus and Poisson's ratio. They can also be expressed as

$$G = \frac{E}{2(1+\nu)}. \quad (11)$$

The constant  $G$  is termed the modulus of rigidity, or shear modulus of elasticity.

### 2.1.3 Deformation of a Circular Diaphragm

The equilibrium equation for a thin, flat plate, first obtained by Lagrange is

$$\frac{\partial^4 w}{\partial x^4} + 2 \frac{\partial^4 w}{\partial x^2 \partial y^2} + \frac{\partial^4 w}{\partial y^4} = \frac{1-\nu^2}{EI} p_0, \quad (12)$$

where  $w$  represents the displacement of a generic point of the middle surface of the plate,  $I=t^3/12$  the moment of inertia,  $t$  the thickness of the plate,  $E$  and  $\nu$  Young's modulus and Poisson's ratio, respectively. For the plate,  $p_0$  is the load per unit area which can also be denoted as pressure.

In the case of the present project, the diaphragm of the IOP sensor can be considered as a thin plate with the edge fixed and uniformly loaded with pressure  $p_0$  (Fig. 3). Due to the boundary condition, the deformation of a generic point of the middle surface of the diaphragm can be calculated as

$$w = \frac{P_0}{64D} (a^2 - r^2)^2, \quad (13)$$

where  $D$  is the flexural rigidity written as  $D=Et^3/12(1-\nu^2)$ . Here  $p_0$  is the pressure applied on the diaphragm,  $a$  is the radius of the diaphragm,  $r$  is the radius of the position one wants to calculate,  $E$  is the Young's Modulus,  $\nu$  is the Poisson's ratio and  $t$  is the thickness of the plate respectively. From Eq. 13, the deformation of a polysilicon circular diaphragm under

---

\* Detailed derivation can be found in reference [16].

atmosphere pressure (760mmHg) can be modeled in MATLAB as given in Appendix A and the results are shown in Fig. 4.

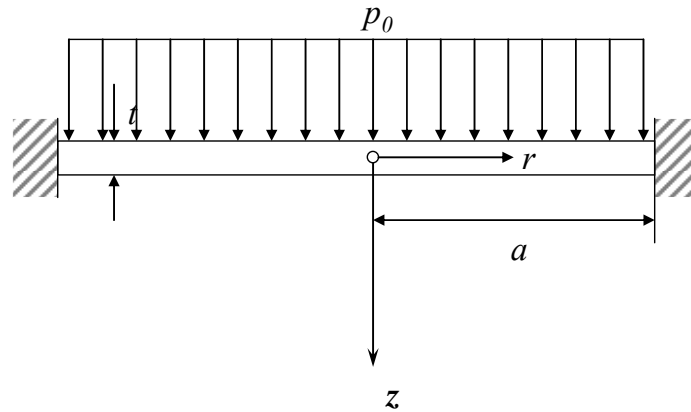
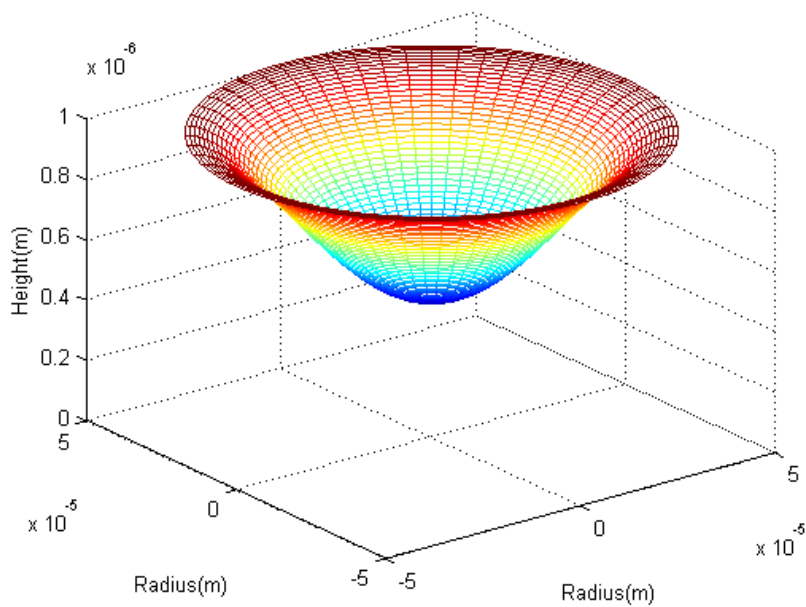
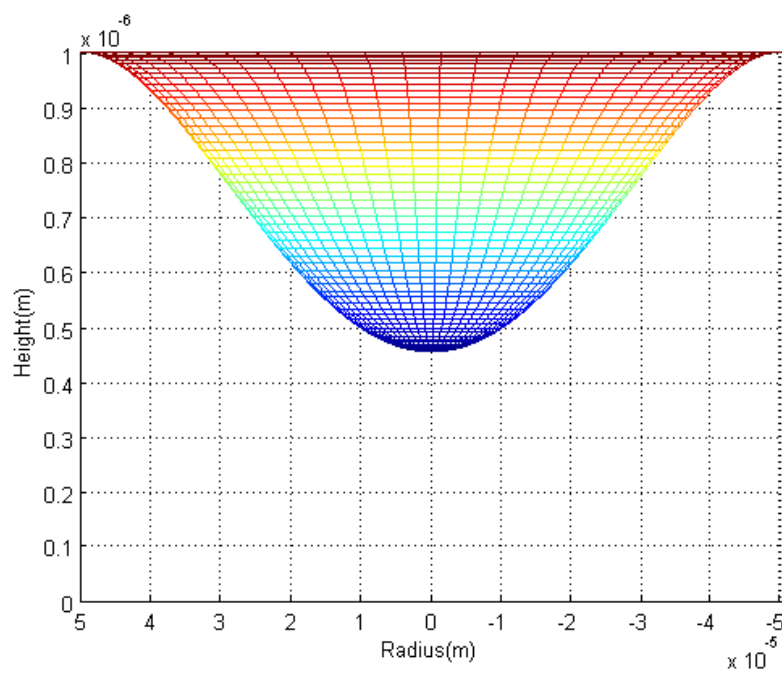


**Fig. 3. An edge-fixed circular diaphragm.**



(a)



(b)

**Fig. 4. The deformation for a polysilicon diaphragm under 760mmHg ( $a=50\mu\text{m}$ ,  $E=120\text{GPa}$ ,  $\nu=0.22$  [17],  $t=1.2\mu\text{m}$ ), (a) 3-D view, (b) Side-view**

## 2.2 Capacitance Calculation of a Circular Diaphragm by Method of Moments (MOM)

### 2.2.1 Method of Moments (MOM)

The Method of Moments (MOM) is a numerical procedure for solving a linear operator equation by transforming it to a system of simultaneous linear algebraic equations, commonly referred to as a matrix equation. It can be applied in many areas of engineering and science including fluid mechanics, acoustics, electromagnetics, and fracture mechanics.

The Method of Moments (MOM) works by constructing a ‘mesh’ over the modeled surface, this process is commonly referred to as ‘meshing’. By applying certain boundary conditions for each mesh element, the MOM generates a set of integral equations which can be reduced to a matrix equation. By solving the matrix equation, the desired values at the interested points of interest in the ‘mesh’ can be obtained numerically. The MOM is often more efficient than other methods, including finite elements, in terms of computational resources for problems where there is a small surface/volume ratio.

The present project is considered as a quasi-electrostatic problem. Under this assumption, and due to the axial-symmetric property, the deformed circular diaphragm is modeled as multiple axial-symmetric charge rings with different charge densities. The diaphragm is an electrical conductive plate and it is placed above the ‘infinite’ ground plane. Due to the Image Theory, the effect of the ground can be replaced by using an image diaphragm with opposite type of charges and the same distance from the ground plane (Fig. 5). The boundary condition for each mesh of this problem is each ring of charge has the same electrical potential as they are physically on the same electrical conductive plate. Then the

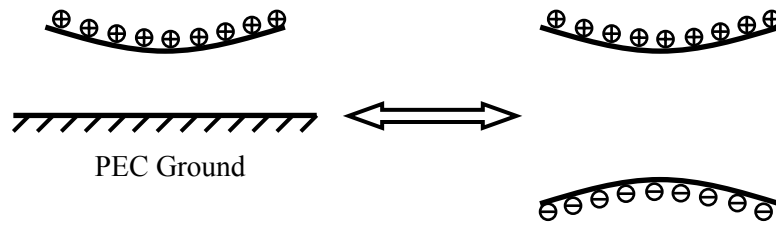


**Fig. 5. The equivalent model of a diaphragm above a ground due to Image Theory.**

moment matrix can be obtained and the charge densities for each charge ring can be solved. By knowing the amount of electric charge stored for the circular diaphragm, the capacitance can be easily calculated.

### 2.2.2 Circular Ring of Charge Modeling

There are several ways to model the circular diaphragm, but due to the axial-symmetric property, the best way is to model it as multiple charge belts or charge rings. The charge belt method assumes each belt has a finite width, which induces the complexity of integrating along the radius for each belt. The charge ring method assumes each ring has infinitesimal width, and if the number of rings is large enough, this method is accurate enough to model the whole circular diaphragm.

When calculating the diagonal elements of the moment matrix, a singularity appears for elliptic integration when putting the calculation points in/on the meshing elements. This is also a modeling problem for a former Master student's thesis [18]. Weber [19] introduced a concept of using a small but finite distance between the calculation point and the charge ring,

permitting a definition of capacitance and this can also be understood as a skin depth in RF applications [20] (Fig. 6).

In the current project, the circular diaphragm with an initial radius  $a$  is divided into  $m$  charge rings, a small but finite skin depth distance  $s$  is introduced between the charge rings and the bottom of the diaphragm. The boundary condition for the moment elements is that all the charge rings have an equal electrical potential as they are electrically conducted. Due to Image Theory, an image diaphragm with an opposite sign of charges is placed by double the distance between the top diaphragm and the ground, the electrical potential is 1Volt and -1Volt for the top and the image diaphragm respectively, then the ground is removed (Fig. 7).

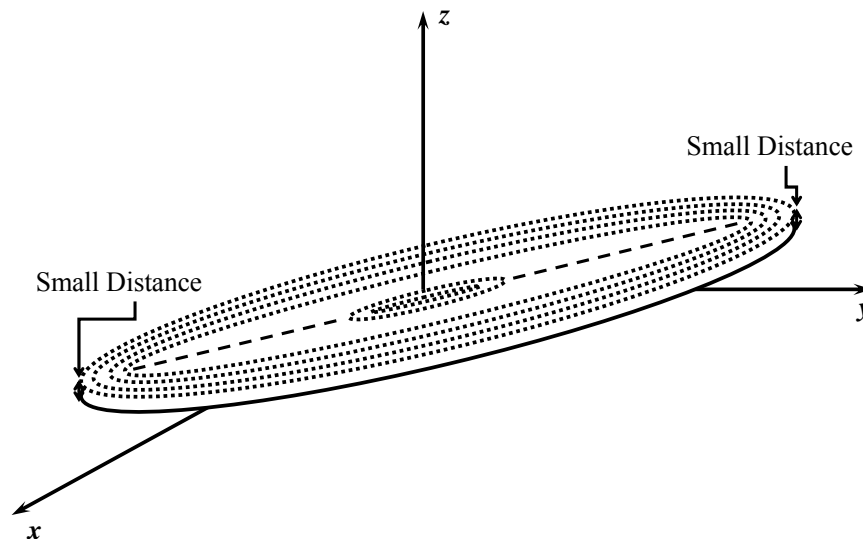


**Fig. 6. Circular ring of charge with a small but finite skin depth.**

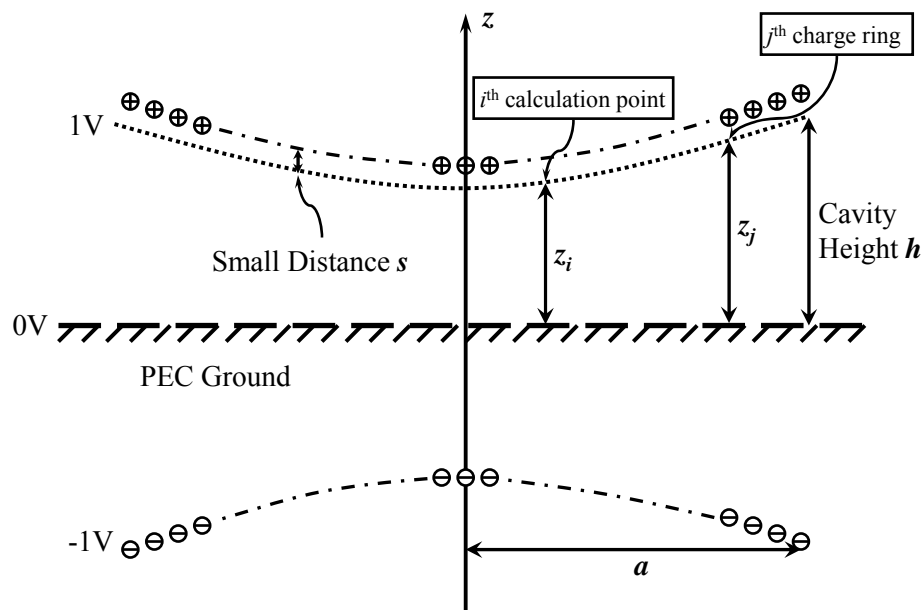


Fig. 7. The MOM model for this project.

### 2.2.3 Capacitance Calculation

If the charge density of the  $j^{\text{th}}$  charge ring is  $\sigma_j$ , then the element charge is  $dq_j = \sigma_j \cdot r_j \cdot d\theta$ , where  $r_j$  is the radius for the  $j^{\text{th}}$  charge ring,  $\theta$  is the angle on the  $x$ - $y$  plane. Due to the axial-symmetric property, the charges are uniformly distributed along the charge ring, so the calculation point can be chosen anywhere along another ring with a small but finite distance from the charge ring plane. Here the calculation points are on the  $x$ -axis.

In free space, the electric potential at one point due to a point charge  $Q$  with a distance  $d$  can be expressed as

$$V = \frac{Q}{4\pi\epsilon_0 d}, \quad (14)$$

so at the  $i^{\text{th}}$  calculation point, the electric potential due to the  $j^{\text{th}}$  charge ring is

$$V_{ij} = \frac{dq_j}{4\pi\epsilon_0|\mathbf{d}_i - \mathbf{d}_j|} = \frac{\sigma_j r_j}{4\pi\epsilon_0} \int_0^{2\pi} \frac{d\theta}{\sqrt{r_i^2 + r_j^2 - 2r_i \cdot r_j \cos \theta + (z_i - z_j - s)^2}} \quad (0 < i, j < m), \quad (15)$$

here  $z_i$  denotes the distance between the  $i^{\text{th}}$  calculation point and the ground plane, and it can be calculated from Eq. 13 as  $z_i = h - w_i$ .

Now taking the image ring into consideration, the electric potential due to both the  $j^{\text{th}}$  charge ring and its image ring can be expressed as

$$V'_{ij} = \frac{dq_j}{4\pi\epsilon_0|\mathbf{d}_i - \mathbf{d}_j|} - \frac{dq'_j}{4\pi\epsilon_0|\mathbf{d}_i - \mathbf{d}'_j|}$$

$$= \frac{\sigma_j r_j}{4\pi\epsilon_0} \left[ \int_0^{2\pi} \frac{d\theta}{\sqrt{r_i^2 + r_j^2 - 2r_i \cdot r_j \cos \theta + (z_i - z_j - s)^2}} - \int_0^{2\pi} \frac{d\theta}{\sqrt{r_i^2 + r_j^2 - 2r_i \cdot r_j \cos \theta + (z_i + z_j + s)^2}} \right] \quad (16)$$

So the electric potential at the  $i^{\text{th}}$  calculation point due to the top diaphragm and its image is

$$V'_i = \sum_{j=1}^m V'_{ij}$$

$$= \sum_{j=1}^m \frac{\sigma_j r_j}{4\pi\epsilon_0} \left[ \int_0^{2\pi} \frac{d\theta}{\sqrt{r_i^2 + r_j^2 - 2r_i \cdot r_j \cos \theta + (z_i - z_j - s)^2}} - \int_0^{2\pi} \frac{d\theta}{\sqrt{r_i^2 + r_j^2 - 2r_i \cdot r_j \cos \theta + (z_i + z_j + s)^2}} \right] \quad (17)$$

If assuming the top diaphragm has an electric potential of 1 Volt and the image diaphragm has an electric potential of -1 Volt, then

$$\sum_{j=1}^m \sigma_j \cdot M_{ij} = 1, \quad (18)$$

where

$$M_{ij} = \frac{r_j}{4\pi\epsilon_0} \left[ \int_0^{2\pi} \frac{d\theta}{\sqrt{r_i^2 + r_j^2 - 2r_i \cdot r_j \cos \theta + (z_i - z_j - s)^2}} - \int_0^{2\pi} \frac{d\theta}{\sqrt{r_i^2 + r_j^2 - 2r_i \cdot r_j \cos \theta + (z_i + z_j + s)^2}} \right] \quad (19)$$

is the moment matrix. Here we should note that if the small distance  $s$  is not used, the first elliptic integration has singularity problem when  $z_i=z_j$  (diagonal elements).

Using  $R_{ji}=M_{ij}^{-1}$ , the charge density for the  $j^{\text{th}}$  charge ring is

$$\sigma_j = \sum_{i=1}^m R_{ji} . \quad (20)$$

The total charge on the top diaphragm is

$$Q = \sum_{j=1}^m 2\pi \cdot r_j \sigma_j . \quad (21)$$

Then the capacitance equals to

$$C = \sum_{j=1}^m 4\pi \cdot r_j \sigma_j . \quad (22)$$

This algorithm can provide the capacitance of a circular diaphragm above a ground plane with different deformations. The algorithm is implanted into MATLAB and the detailed code can be found in Appendix A. Good agreement up to 10GHz can be observed between the algorithm and the HFSS simulation for a flat circular conductor for different radii (Fig. 8). The difficulty arises in HFSS for deformed diaphragm since it is impossible to construct a 3-D model for all the deformed cases. However the MOM algorithm calculates both the physical and electrical results at the same time and can produce faster results than HFSS.

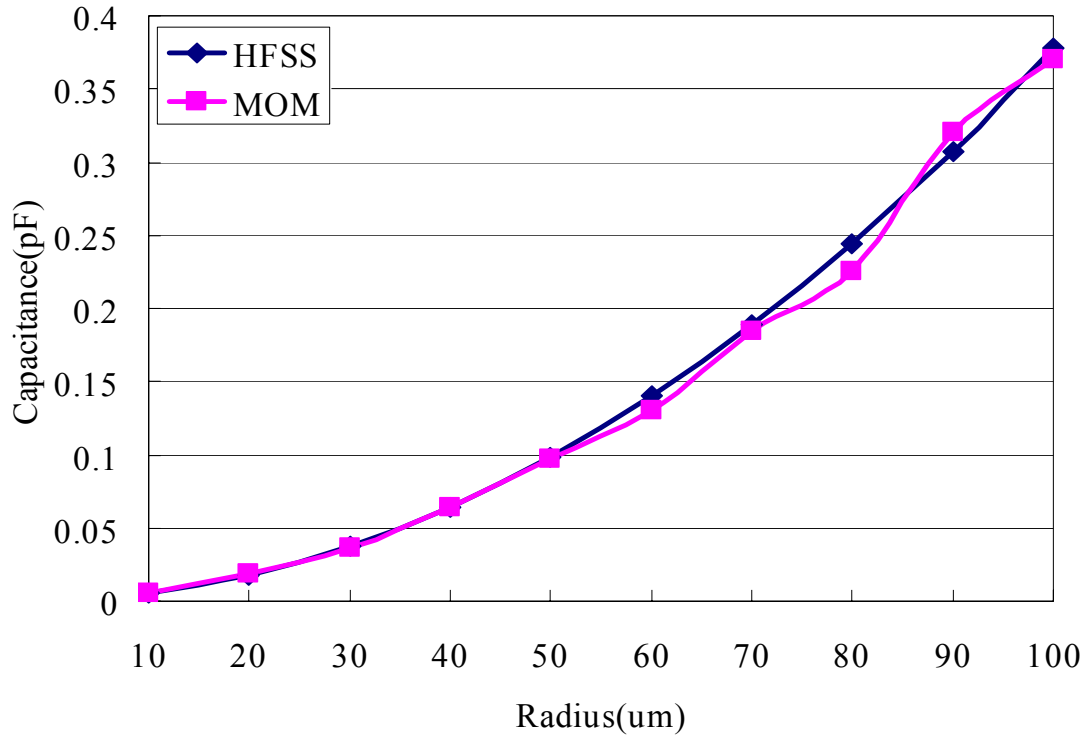


**Fig. 8.** Comparison of the capacitance calculation between the MOM (MATLAB) algorithm and the HFSS simulation for a flat circular diaphragm.

## **CHAPTER 3. INTRAOCULAR PRESSURE (IOP) SENSOR DESIGN**

This chapter discusses several issues which need to be taken care of during the IOP sensor design. The design steps focus on a high-Q (low electrical loss) solution, minimizing the sensor size, high sensitivity, as well as low fabrication cost. For the present project, both mechanical and electrical properties are considered for layer materials, and several issues are addressed which are also common concerns for most of the MEMS fabrication work: high-Q on-chip inductor, stiction, sacrificial etching, critical point drying, step coverage, residual stress release, and channel sealing. The mask design integrates an 8 layer process into a 2 layer mask, which reduces the manufacture cost for the research project.

### **3.1 Structure Consideration**

#### **3.1.1 Membrane**

As discussed in the previous chapters, the pressure sensing element for the IOP sensor is the circular membrane. The circular shape has a larger sensitivity than other shapes such as rectangular or triangle, and it also allows the stress to be distributed uniformly on the edge. Also a membrane array is preferred to improve the sensitivity.

A vacuum cavity is also preferred to improve the sensitivity. If an air cavity is presented, as the external pressure changes, the volume of the cavity changes and compresses the air inside. The inside pressure increases as well which tends to reduce the deformation of the membrane, and also reduces the sensitivity. Also an air cavity will have thermal issues if the temperature of the environment varies.

### 3.1.2 Inductor

The inductor works not only as the resonant element for the LC resonator, but also as the coupling element of the sensor which is detected by an external coil. On-chip spiral inductors are not preferred due to their low-Q and poor coupling effects [7], [8], [10], [11], [18].

Although a lot of effort has been put to reduce the electrical loss for on-chip inductors and to improve their Q factor [21], [22], those designs always involve complicated structures or fabrication processes, that are unrealistic for the IOP sensor design.

The present project uses a small size coil inductor or enamel coil bonded with the membrane array. The value of the coil inductor and diameter of the enamel coil can be well controlled as well as the number of turns. A proposed IOP sensor is shown in Fig. 9. The pads are for bonding purposes.

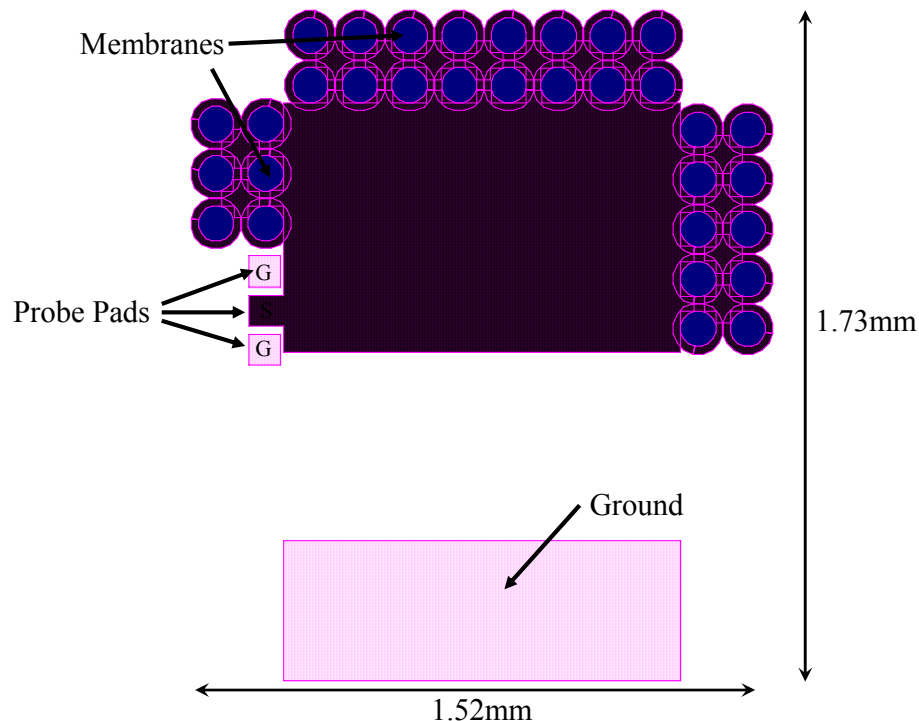


**Fig. 9. A proposed IOP sensor membrane array with inductor attaching pads.**

### 3.2 Material Consideration

The wafer substrate acts as the ground signal return path. In order to make a high-Q LC resonator, the wafer needs to be low resistive in order to reduce the electrical loss. A <100> phosphorus doped (n-type) 4" low resistance (0.001-0.002Ohm-cm) wafer was used in this project.

Between the membrane and the wafer substrate, an insulation layer is needed to separate the two electrodes. Silicon Nitride ( $\text{Si}_3\text{N}_4$ ) has been chosen as the insulation layer due to its many superior properties. It has a really high electrical resistivity ( $>10^{15}\text{Ohm-cm}$ ) which provides a good insulation between the membrane and the substrate electrode. It provides an excellent barrier to the diffusion of water and ions such as sodium. Its ultrastrong resistance to

oxidation and many etchants such as a HF solution makes it survive during the other process steps.  $\text{Si}_3\text{N}_4$  is usually deposited by low-pressure chemical vapor deposition (LPCVD) at about  $800^\circ\text{C}$ . Such a high temperature prevents its properties from changing due to other high temperature processing steps, and makes  $\text{Si}_3\text{N}_4$  a really stable layer.

In order to build up a free standing membrane structure, a sacrificial etching technique is designated to be used in the present processing. The sacrificial components are usually made of phosphosilicate glass (PSG) or  $\text{SiO}_2$  deposited on a substrate by LPCVD techniques. This design chooses PSG to be the sacrificial layer due to its high etching rate in HF solutions.

The membrane layer works as the pressure sensing element, so both the mechanical and electrical properties need to be considered. First of all, the IOP sensor is designed to work in the pressure range of 0~80mmHg (relative to atmosphere pressure). As discussed in Section 2.1.2, at the highest pressure, this layer should still work in the elastic range, otherwise the membrane will deform permanently. Secondly, in order to get a high-Q resonator, the membrane layer should have a low electrical resistivity. Thirdly, this layer should have a relatively low etching rate in HF solution because it will go through the sacrificial etching process. This layer should also be able to retain the same properties for any further fabrication process. Polycrystalline silicon (polysilicon) is chosen as the membrane layer for this IOP sensor fabrication. Firstly, the mechanical properties of polysilicon and other selected materials are list in Table 2 [23], from here we can see polysilicon has a relatively high yield strength. Secondly, polysilicon can be formed by LPCVD at about  $600^\circ\text{C}$  or  $650^\circ\text{C}$ . This can assure that polysilicon retains its property in other high temperature process rather than using metal layers, since metals will be oxidized during high temperature environment. Thirdly, polysilicon can be doped by phosphorus or boron to become a conductor [24], thus making

polysilicon a good choice to form a high-Q resonator. In this project the polysilicon is doped by phosphorus and becomes an n-type polysilicon (Phos-poly). By using the algorithm derived in chapter 3 and HFSS, the capacitance for a flat circular membrane with different radii and materials can be calculated as in Fig. 10, the MOM algorithm agrees with HFSS very well and the capacitance for doped polysilicon membrane only degrades a little from perfect electrical conductor (PEC) case. Fourthly, the polysilicon (structural layer) and PSG (sacrificial layer) is a good pair for sacrificial etching, since polysilicon has a very low etching rate in HF solutions [25]. Lastly, polysilicon is a good biocompatible material that does not need any coating for implantation [26].

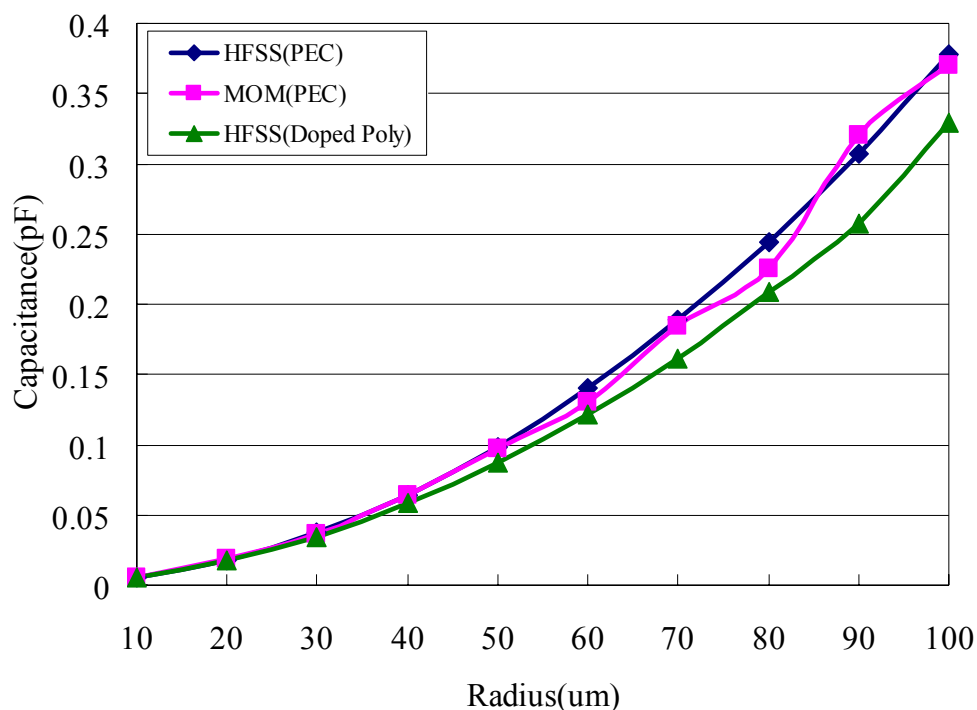


**Fig. 10. Capacitance calculation for a flat circular membrane with different radii and different materials.**

After sacrificial etching and membrane release, the membrane needs to be sealed by another layer material. As the layers pile up, the cavity's channel height becomes large and

more difficult to be sealed. It requires a technique which has a high deposition rate, and good step coverage property. This project chooses plasma-enhanced chemical vapor deposited (PECVD)  $\text{SiO}_2$  as the sealing material. PECVD  $\text{SiO}_2$  has a faster deposition rate than LPCVD and faster etching rate than PECVD  $\text{Si}_3\text{N}_4$  in HF solutions. Also, PECVD  $\text{SiO}_2$  deposits at a lower temperature  $340^\circ\text{C}$ , and this does not change any properties of the existing layers such as  $\text{Si}_3\text{N}_4$  and polysilicon.

After sealing, all the membranes need to be connected by a high electrical conductive layer to form an array. This layer will be a thick layer since it needs to cover several steps from previous process. Aluminum or titanium can be used, and DC Sputtering technique is chosen as it has a high deposition rate. In this project, the metal contact layer is aluminum.

Material	Density (g/cm <sup>3</sup> )	Yield Strength (GPa)	Knoop Hardness (kg/mm <sup>2</sup> )	Young's Modulus (GPa)	Thermal Expansion Coefficient (10 <sup>-6</sup> /K)	Thermal Conductivity (W/cm-K)
Si	2.3	7.0	850	190	2.3	1.6
SiO <sub>2</sub> (Fibers)	2.5	8.4	820	73	0.55	0.014
Si <sub>3</sub> N <sub>4</sub>	3.1	14	3500	390	0.8	0.19
Diamond	3.5	53	7000	1000	1.0	20
Aluminum	2.7	0.17	130	70	25	2.4
Tungsten	19	4.0	490	410	4.5	1.8
Steel (max.)	7.9	4.2	1500	210	12	0.97
Polysilicon		1.2		170		

**Table 2. Mechanical properties of polysilicon and selected materials [23].**

### 3.3 Size and Dimension Consideration

The IOP sensor is designed to measure a relative pressure range of 0~80mmHg. For the membrane structure, a cavity height (sacrificial etching channel height) of 1um or larger is preferred to retain a shorter sacrificial etching time. The thickness of the membrane should be kept as thin as possible, but should be at least 10% thicker than the sacrificial layer to keep a good step coverage, and also should not touch the substrate at the highest pressure the IOP will measure.

By using the MOM algorithm derived from Chapter 2, the capacitance in respect to different membrane thicknesses, radii and cavity heights can be summarized in Table 3. The Q factor for a single circular membrane with different radii has been calculated as well (Fig. 11). From those results, a circular Phos-poly membrane with a radius of 50um and thickness of 1.12um is chosen, the cavity height (PSG sacrificial layer thickness) is designed as 1um. This structure dimension gives a high Q-factor of 80 at 2GHz and about 155 at 1GHz, it also gives the highest area sensitivity about 0.73593246pF/mm<sup>2</sup>.

Polysilicon usually has a Young's modulus of 120GPa, and a Poisson's ratio of 0.22 [27]. For the circular membrane under different pressures, the maximum stress happens at the edge of the diaphragm [16] as

$$P_{\max} = \frac{3p_0 a^2}{4t^2}, \quad (23)$$

where  $p_0$  it the applied pressure,  $a$  is the radius of the circular diaphragm, and  $t$  is the thickness of the diaphragm.

Radius (um)	Cavity Height (um)	Membrane Thickness (um)	Capacitance under 760mmHg (pF)	Capacitance under 900mmHg (pF)	Delta C (pF)	Delta C/mm <sup>2</sup>	Pmax (Gpa)
30	0.6	0.71	0.05652	0.05813	0.00161	0.56871366	0.16067
40	0.8	0.91	0.08608	0.08953	0.00345	0.68555992	0.17388
50	1	1.12	0.11818	0.12396	0.00578	0.73593246	0.17936
60	1	1.43	0.16759	0.17568	0.00809	0.71531305	0.15843
70	1	1.75	0.22628	0.23743	0.01115	0.72431739	0.14398

**Table 3. Electrical and mechanical properties for a single circular membrane with different radii and cavity heights.**

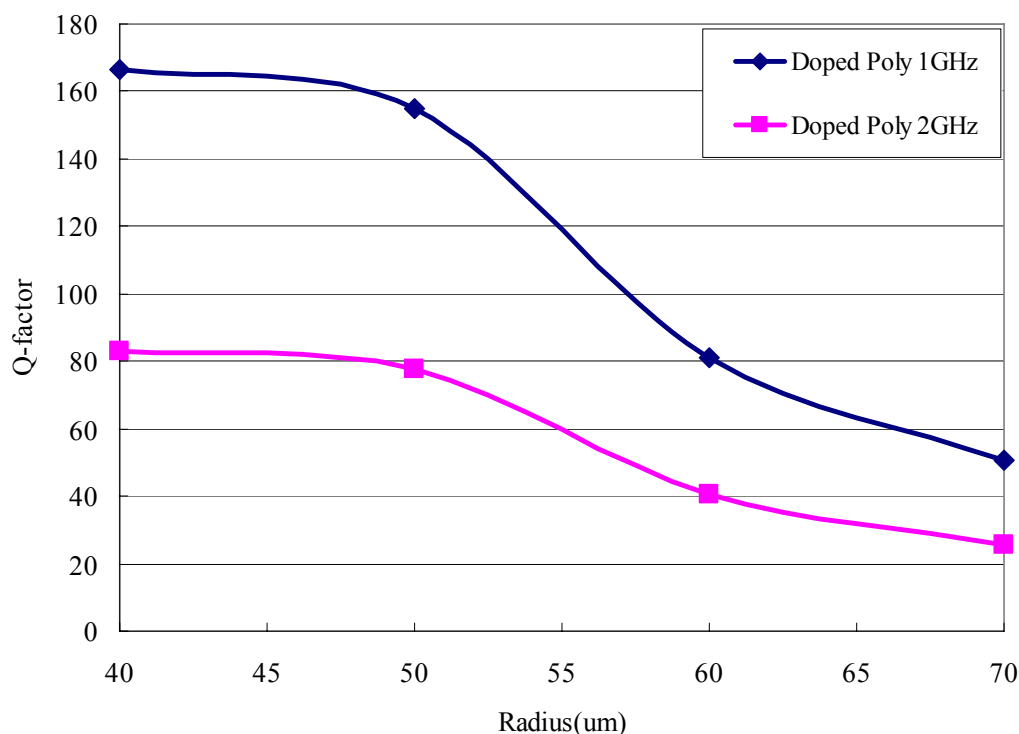
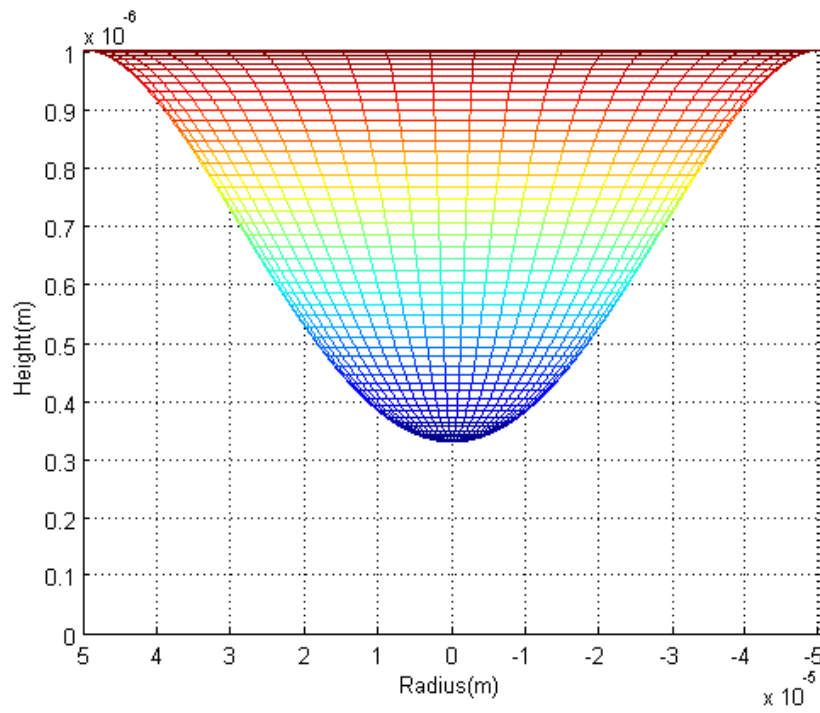
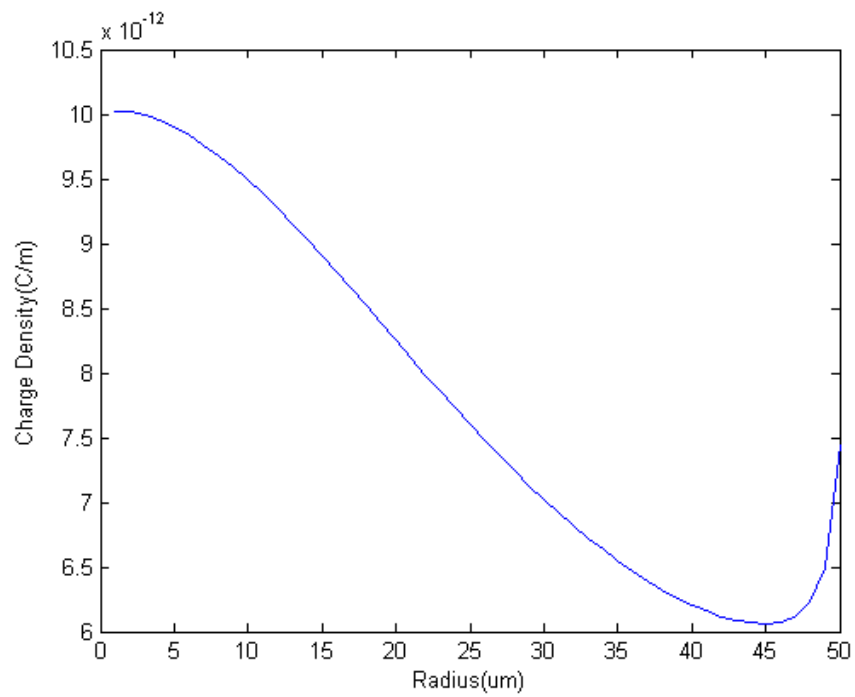


**Fig. 11. Q-factor for a single circular membrane with different radii.**

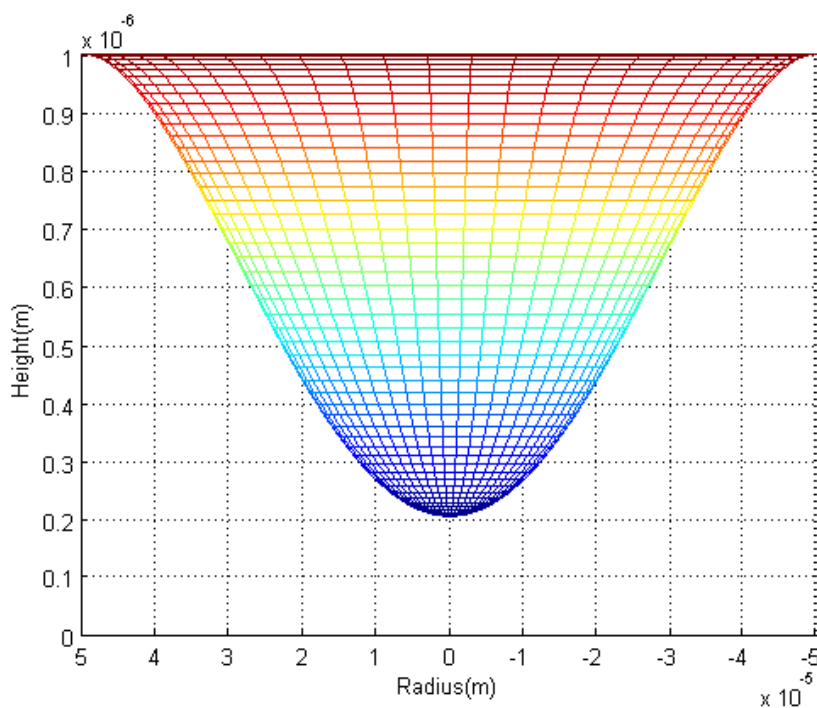
For the current design, when the applied pressure is 90mmHg, the maximum stress at the membrane edge is 0.17936GPa, which is smaller than the yield strength of polysilicon of 1.2GPa. However, the aluminum only has a yield strength of 0.17GPa [23], so if the aluminum is used as the membrane layer, it will be permanently deformed at the highest pressure. For the current design, the deformation and charge density for a membrane with a radius of 50um and a cavity height of 1um under different pressures are shown in Fig. 12. Also, a proposed parallel LC resonator design with 32 membrane structures is demonstrated in Fig. 9 in Section 3.1



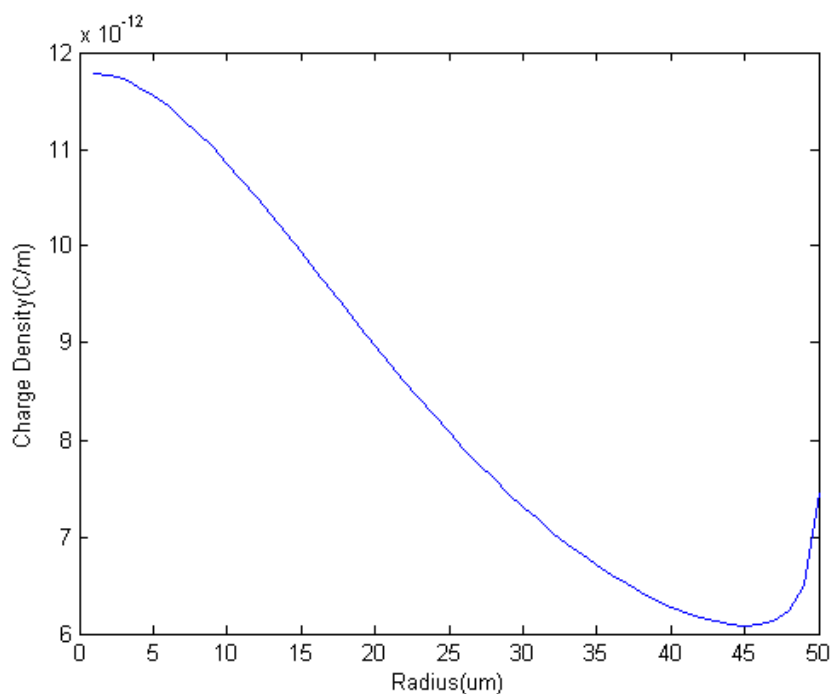
(a)



(b)



(c)



(d)

**Fig. 12.** The deformation and charge density for a Phos-poly diaphragm ( $a=50\mu\text{m}$ ,  $E=120\text{GPa}$ ,  $\nu=0.22$ ,  $t=1.2\mu\text{m}$ ), (a,b) Under 760mmHg, (c,d) Under 900mmHg.

### 3.4 Mask Consideration

An 8-layer bright-field mask design for the membrane structure is shown in Fig.13. Mask 1 has a diameter of 90um and uses negative photoresist to define the substrate electrode, the  $\text{Si}_3\text{N}_4$  layer is designed to have a thickness of about 0.5um. Mask 2 has a diameter of 110um with 8 etching channels with a width of 22um to define the PSG sacrificial layer. The larger diameter than mask 1 takes consideration of any undercut or over-etching for both layer 1 ( $\text{Si}_3\text{N}_4$ ) and layer 2 (PSG), which can prevent the membrane from touching the substrate. The thickness of the PSG is designed as 1~2um to retain shorter sacrificial etching time. Mask 3 defines the polysilicon membrane with a diameter of 130um, the larger diameter provides the membrane stands to support the membrane. Phos-poly is designed to have a thickness about 1.2um. Mask 4 defines a PECVD  $\text{SiO}_2$  seal ring for the cavity, it has an outer diameter of 150um and an inner diameter of 104um, resulting in a width of 23um to seal the channel and taking any undercut into consideration. The thickness of PECVD  $\text{SiO}_2$  is designed to be about 3um in order to cover the larger steps from the channel and membrane. Mask 5 defines a metal contact ring with an outer diameter 130um and inner diameter 90um. This larger width is designed to cover the larger step from PECVD  $\text{SiO}_2$  and maintain the connection among all the membranes to form an array. Mask 6 with a diameter of 132um defines a thin metal layer to cover the polysilicon membrane to improve the Q factor (if necessary). Masks 7 and 8 define biocompatible layers to cover the metal contacts. All the mask designs compensate for the undercuts either from photoresist over exposed/developed or wet etching.

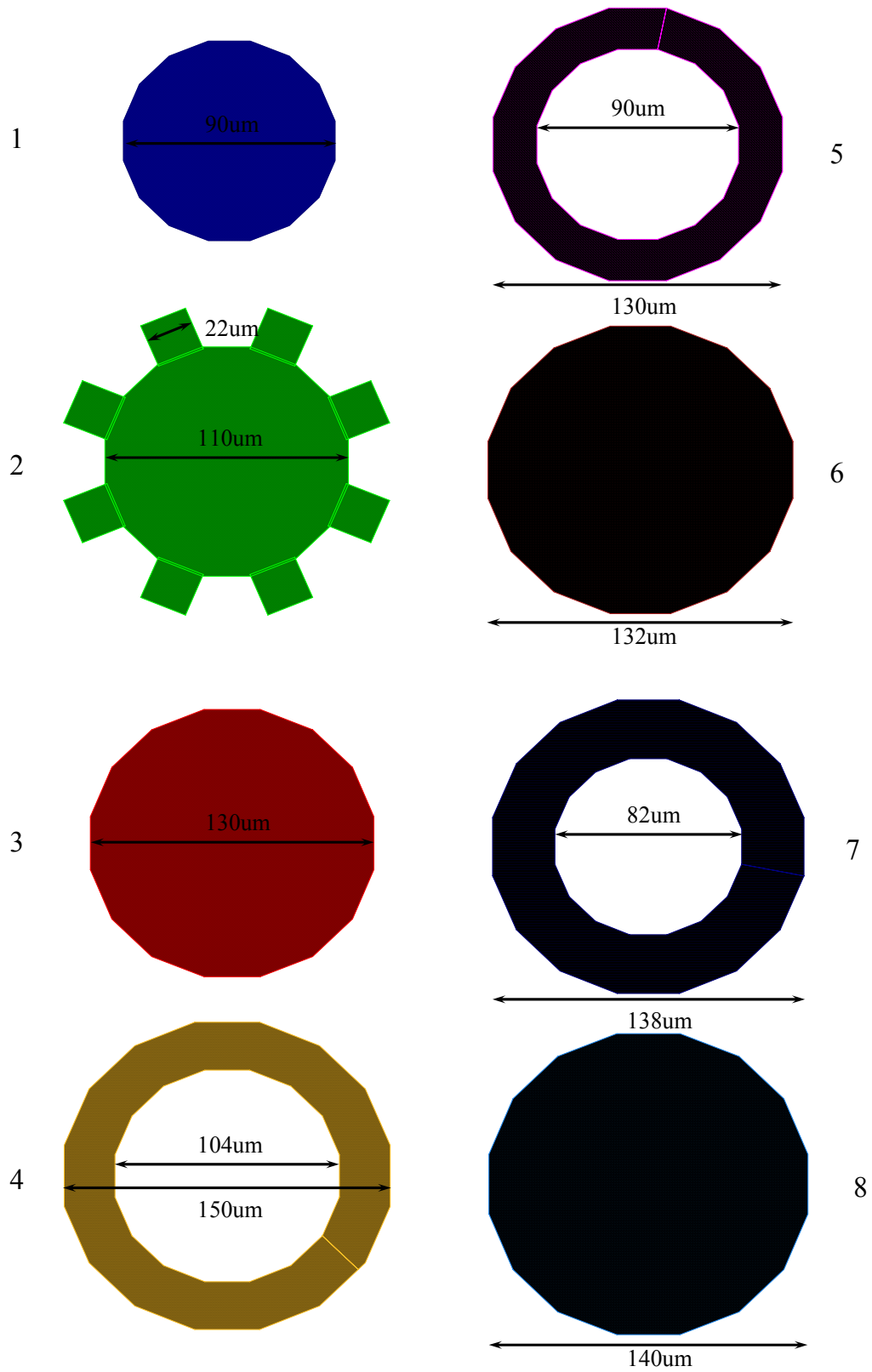


Fig. 13. 8-layer mask design for IOP sensor.

In order to reduce the fabrication budget, this project synthesizes the 8-layer processing mask on a 2-layer processing mask. A set of alignment markers are designed as in Fig. 14 and 15. Alignment markers A and B have their own orientations, and when they combine together, they can also align with each other (Fig. 16). Assign alignment marker A as ♂ and alignment marker B as ♀, the idea is to only use one quadrant on the wafer. And after each mask process, either the wafer or the mask needs to be rotated by  $90^\circ$  for the next lithography step. A Karl Suss MA-6 Aligner can only view alignment markers in a certain area on the  $x$ -axis\*. In Fig. 17 and 18, the alignment markers on  $x$ - and  $y$ - align with each other after rotating, the number denotes the distance from the center of the mask to the alignment marker in micrometer, for example, 100 means 100um from the center of the mask.

---

\* Equipment SOP from Nano Fabrication Center of University of Minnesota, <http://www.nfc.umn.edu>.

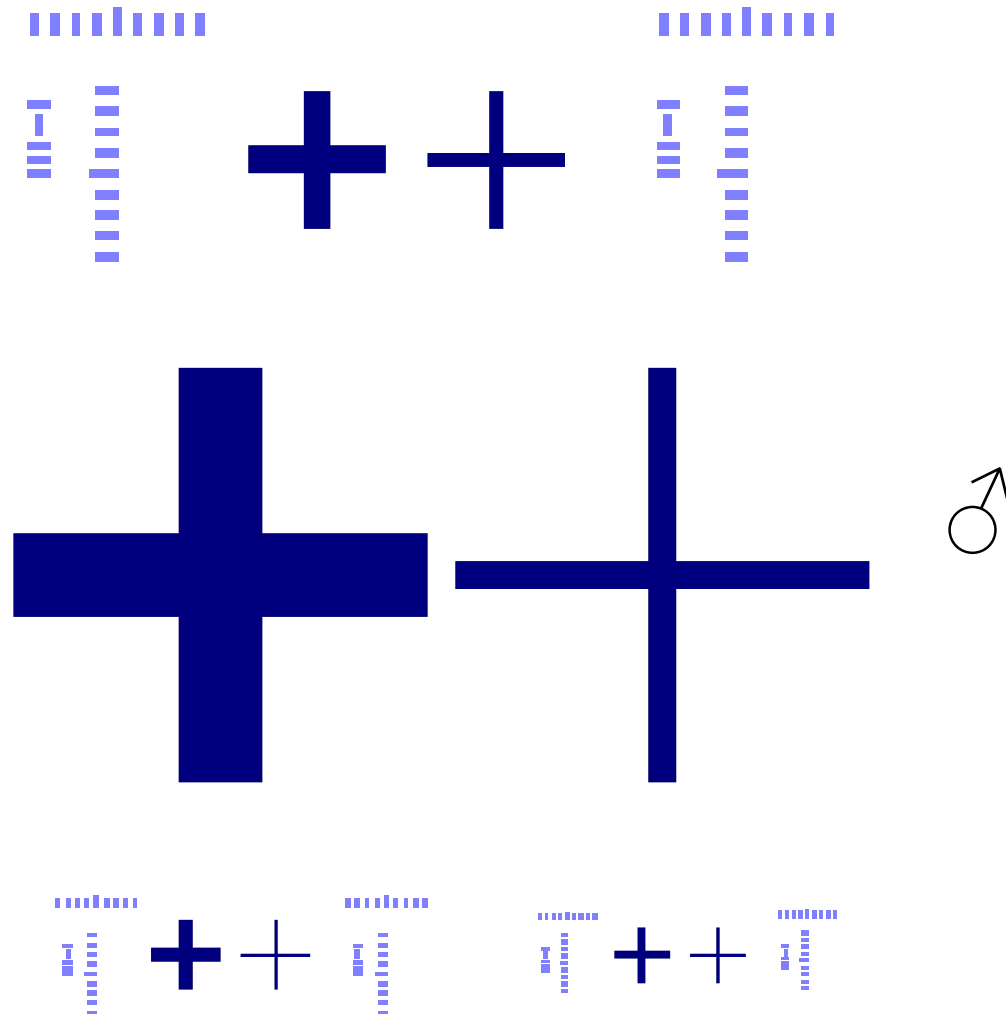


Fig. 14.Alignment marker A.

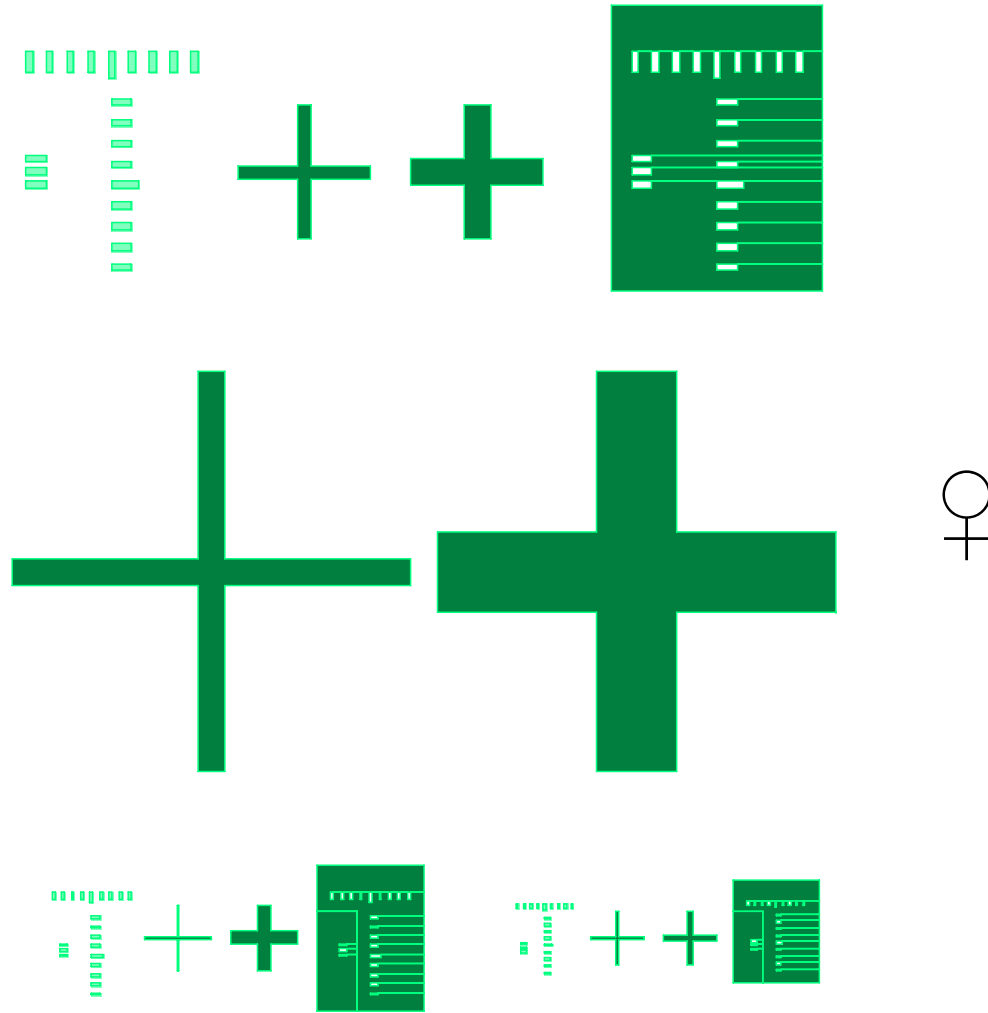


Fig. 15.Alignment marker B.

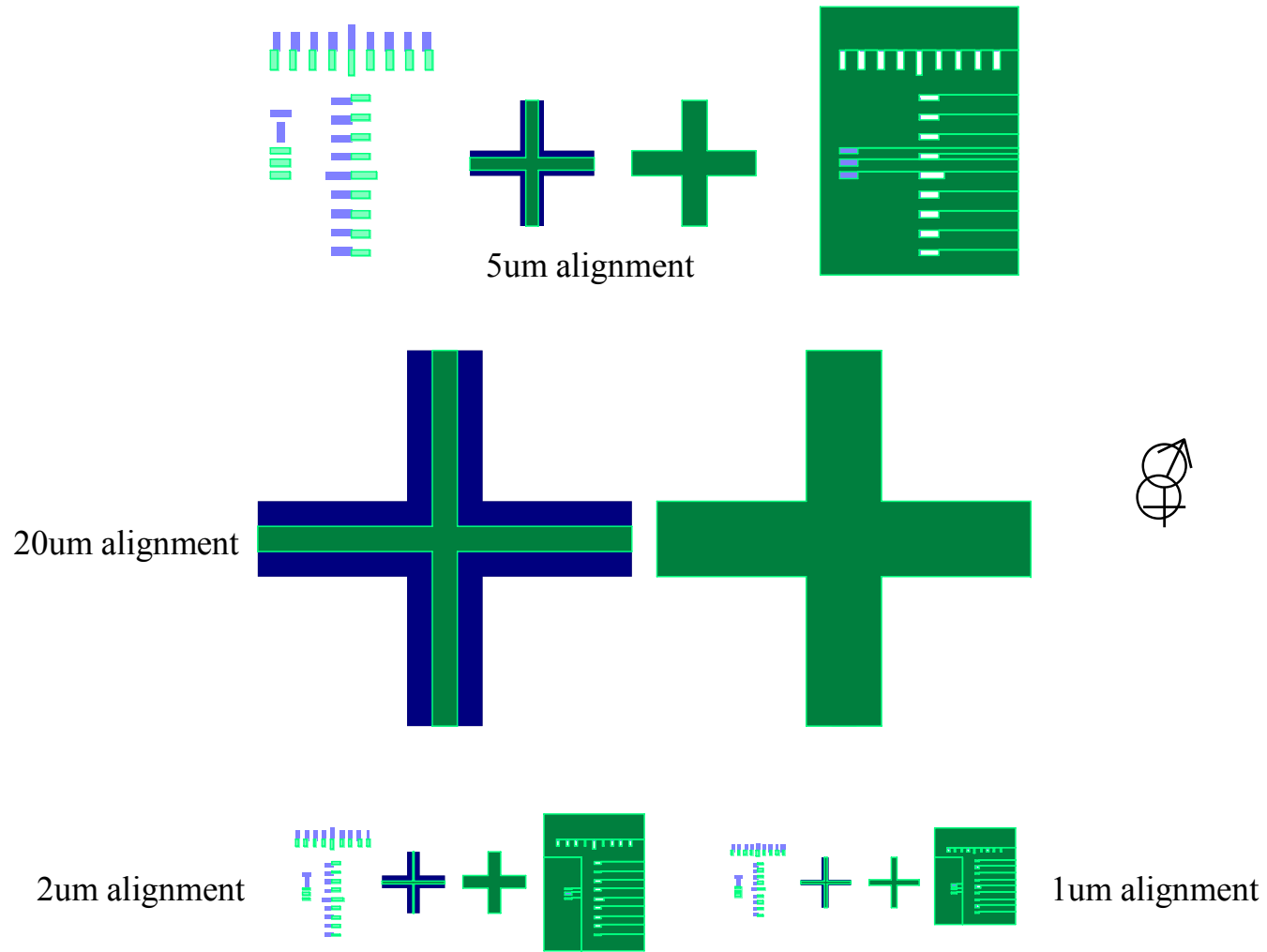


Fig. 16.Alignment marker A&B.

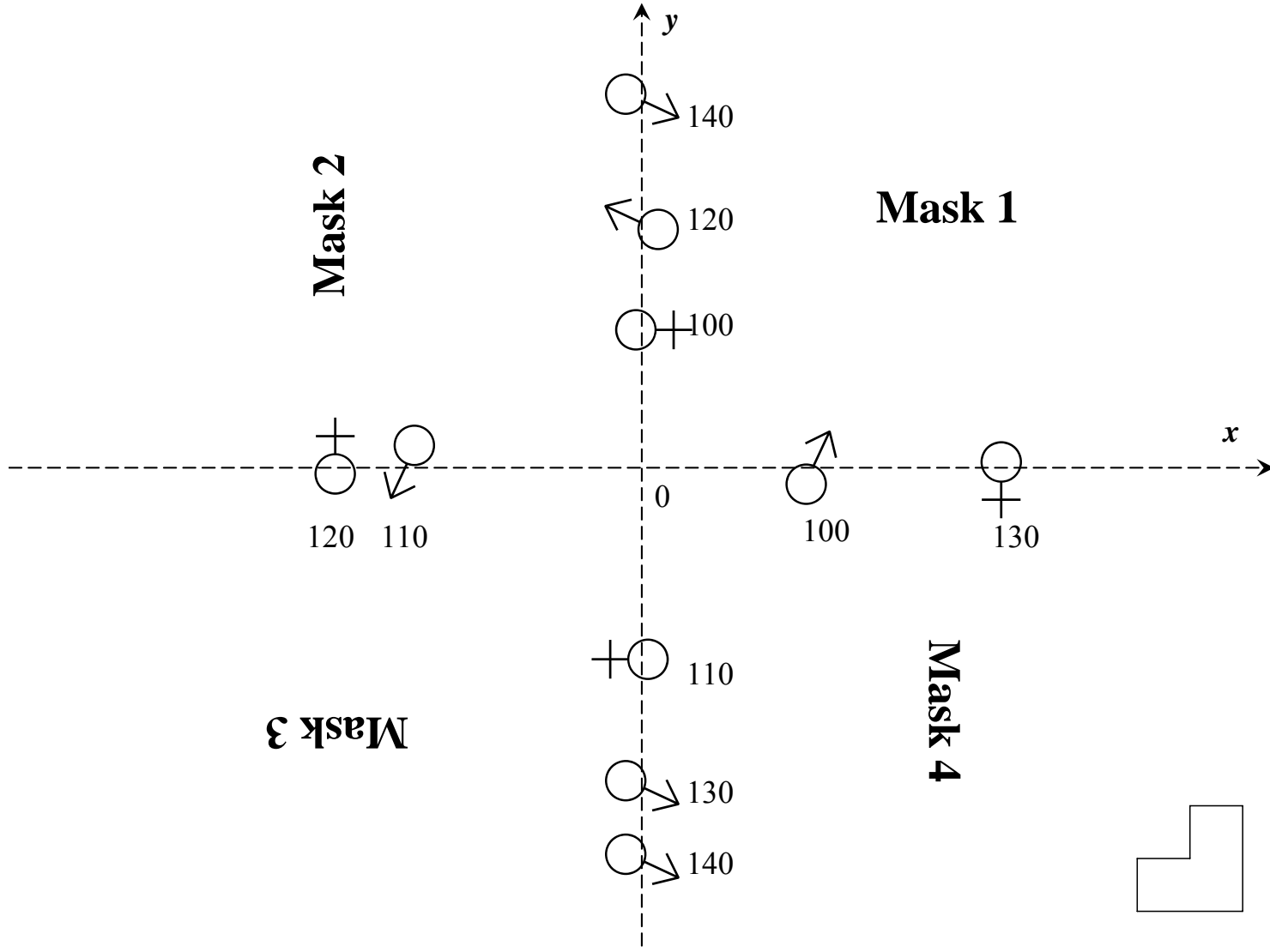


Fig. 17.Mask 1-4 synthesized into the first mask.

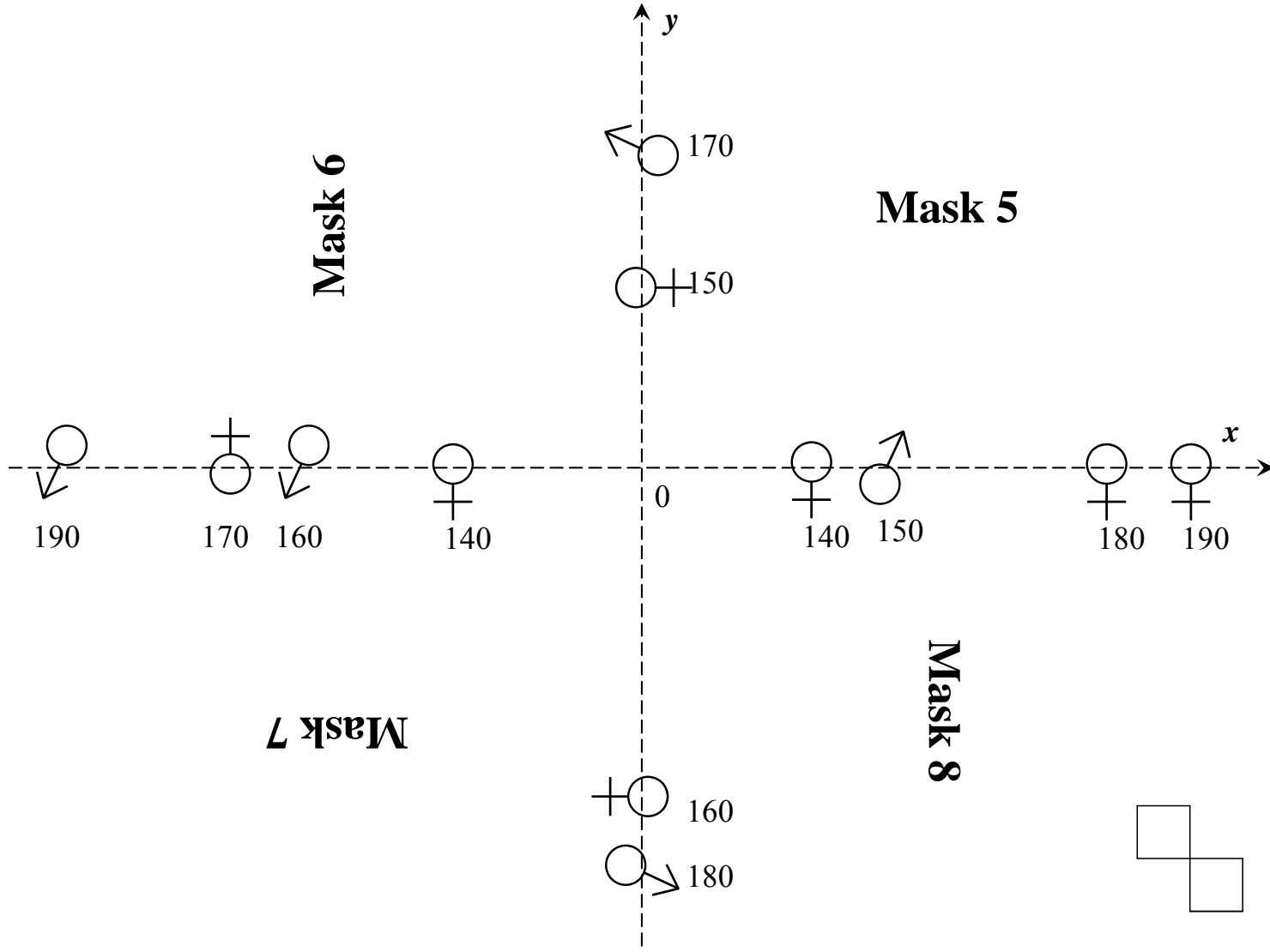


Fig. 18.Mask 5-8 synthesized into the second mask.

### 3.5 Fabrication Consideration

Surface micromachining is characterized by the fabrication of micromechanical structures from deposited thin films. It has become an increasingly popular technology in recent MEMS device fabrication works, with potential advantages over bulk micromachining such as smaller device size and CMOS compatibility [28]. This project uses surface micromachining technology for the IOP sensor fabrication, it includes: LPCVD and PECVD of thin film such as  $\text{Si}_3\text{N}_4$ ,  $\text{SiO}_2$  and polysilicon, a sacrificial etching release suspended structure, cavity sealing, and wet/dry etching. There are several central issues, not only for this project but also for most of the MEMS work, that have been addressed in the fabrication process.

#### 3.5.1 Residual Stress

Polysilicon is used in this project to serve as the mechanical layer. One of the limiting factors in the fabrication of surface micromachining structures is the residual stress development. There are two main sources of stress development. One is the thermal stress due to the mismatch of thermal expansion coefficients between the film and the substrate, accentuated by depositions performed at elevated temperatures. The other is the intrinsic stress mainly originating from nucleation, grain growth and incorporation of impurities during film deposition. The residual stress will cause a layer peeling off from another layer, or cause suspended structure failure, such as cantilever bending [29] (Fig. 19).

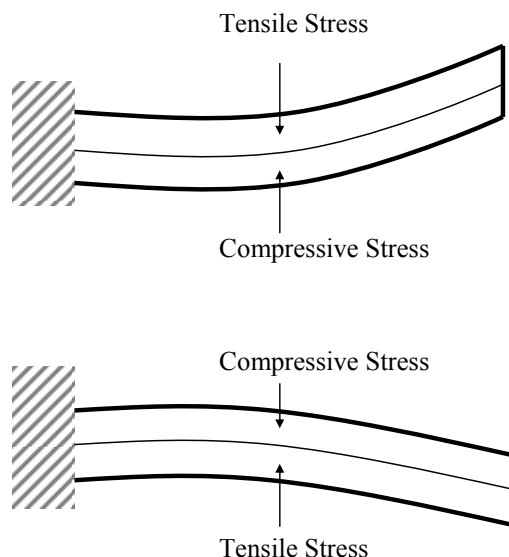


**Fig. 19. Polysilicon cantilever with different type of stresses.**

This project uses stacked un-doped and phosphorous doped polysilicon for the mechanical layer, and this kind of structure usually has a tensile residual stress [29], [30]. The Rapid Thermal Annealing (RTA) is used in the IOP sensor process. During the annealing process, the oxidation of polysilicon film induces a compressive stress and tends to reduce the tensile stress [30]. The using of RTA can also lower the thermal budget.

### 3.5.2 HF Vapor Sacrificial Etching

Surface micromachining techniques exploit a selective sacrificial layer etch scheme to free overlying structural layers. In general, any sacrificial layer that can be etched selectively with respect to the substrate, isolation layer, and structural layer may be used for this process. PSG is commonly used as a sacrificial layer due to its fast etching rate in HF solutions. In this

project, polysilicon,  $\text{Si}_3\text{N}_4$  and silicon substrate all have a relatively lower etching rate in HF solutions.

Although HF can etch PSG really fast, the sacrificial release of large area plates or the removal of sacrificial material inside long and blind channels can be very time consuming. This always ends with the etchant attacking the structural or isolation layers. In this sense, sacrificial etching should be conducted as fast as possible to reduce these risks.

HF vapor has been proven to have a higher etching rate for PSG than the liquid HF solutions such as Buffer Oxide Etchant (BOE) or concentrate HF (49%) [31]. This project uses a Teflon box with concentrated HF (49%) for the HF vapor sacrificial etching process.

Another reason to use vapor phase for the etchant is to avoid stiction. If the wet etching is involved in the sacrificial etching process, it is necessary to dry the wafer afterwards by natural or forced evaporation. As liquid is gradually removed through evaporation, the top surface of a microstructure is exposed to air. A surface tension force develops at the interface of trapped liquid and air acting in the direction that is tangent to the liquid-air interface. For a small gap spacing, the surface tension forces can cause appreciable deformation of the surface microstructures.

This failure mode of microstructures is referred to as stiction. Stiction is the main cause for the large amount of scraps in surface micromachining. One stiction case for cantilever is explained in Fig. 20.

Considerable mechanical forces are required to separate the two stuck layers again and these excessive forces can break the delicate microstructure.

This project eliminates the chance to use liquid sacrificial etching solution. Although HF vapor leaves surface residues after releasing [31], those can be cleaned by dipping into

BOE and solvents. Solvents such as Methanol or Isopropyl Alcohol have a high surface mobility and will clean inside the cavity really well.

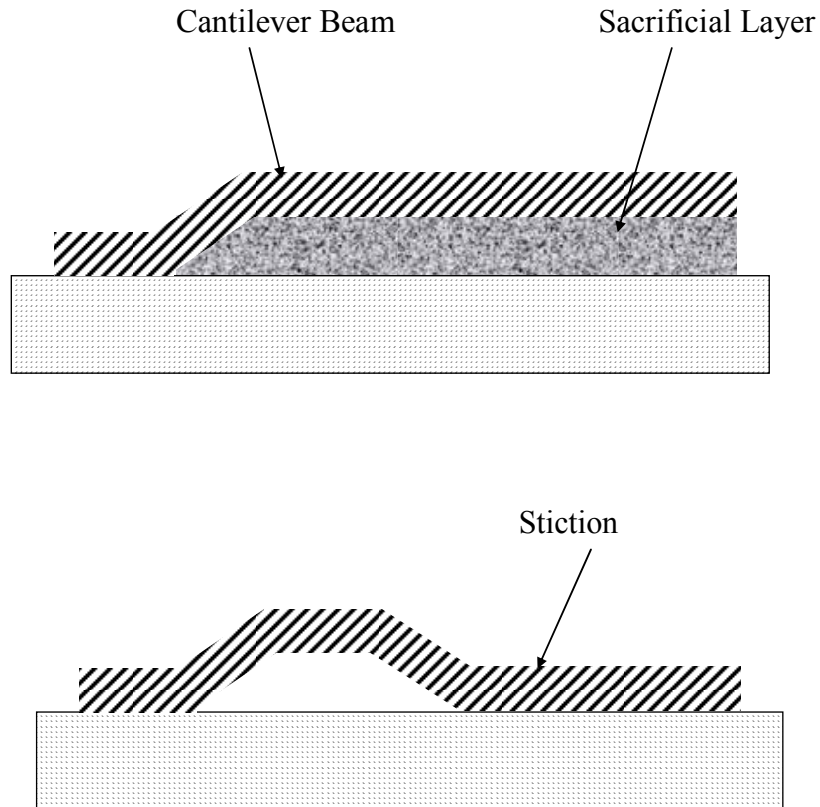


**Fig. 20. The collapse of a thin cantilever beam due to stiction.**

### 3.5.3 Critical Point Drying (CPD)

As discussed above, stiction is induced by the adverse surface tension associated with the liquid-air interface. However, the occurrence of what is known as 'continuity of state' suggests a drying technique for which the surface tension can be reduced to zero. If the temperature of liquefied gas is increased, the meniscus becomes flatter indicating a reduction

in the surface tension. If the surface tension becomes very small the liquid surface becomes very unsteady and ultimately disappears.

When this 'critical point' is reached, it is possible to pass from liquid to gas without any abrupt change in state. If a specimen had been in the liquid it would have experienced a transition to a 'dry' gas environment without being in contact with a surface, avoiding the possibility of the damaging effects of surface tension.

The critical point drying (CPD) starts by immersing the structure in a liquid under moderate pressure and room temperature, this condition is indicated by point 1 in the phase diagram (Fig. 21). Then the temperature is increased while the pressure is maintained constant, the solvent then makes a transition from the liquid phase to the supercritical phase (point 2). The pressure of the supercritical fluid is then dropped, causing the supercritical fluid to turn into a vapor (point 3). Then transformation from liquid to supercritical fluid and then to vapor involves zero surface tension.

This project uses carbon dioxide as the supercritical fluid (critical point 304.25K at 7.39MPa or 31.1°C Celsius at 1072psi).

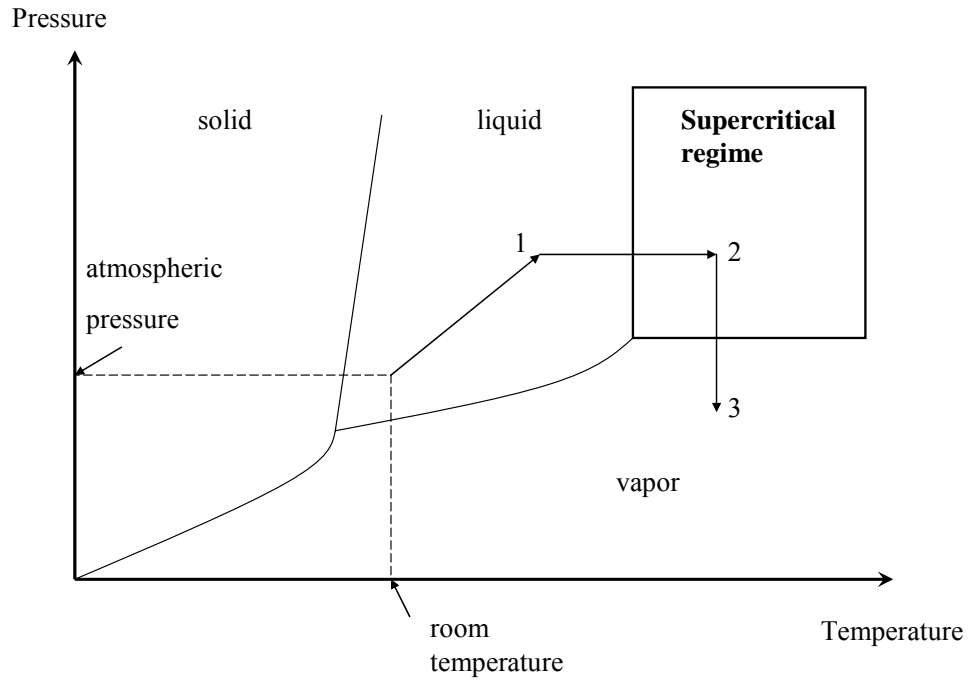


**Fig. 21. Carbon dioxide supercritical drying.**

## **CHAPTER 4. INTRAOCULAR PRESSURE (IOP) SENSOR FABRICATION**

Part of the fabrication work was published in IEEE International Conference on Electro/Information Technology 2008 as “Vapor HF Sacrificial Etching for Phosphorus Doped Polycrystalline Silicon Membrane Structures”.

Haibo Cao, and Robert J. Weber

### **4.1 Introduction**

Membrane or diaphragm structures in Micro Electro Mechanical Systems (MEMS) have been widely used as pressure sensors. The pressure is determined by detecting the capacitance change between the deformed diaphragm and the substrate electrode. This kind of application can be achieved by integrating the membrane structures with a CMOS circuit or inductive elements to obtain wired or wireless read-out [6]-[11], [18], [32], [33].

A sacrificial etching process is a common way to form a suspended structure. The selection of structural and sacrificial layers always requires that the etchant has a high etch rate and high selectivity for the sacrificial layer, and the deposition and etching process for those two layers will not attack, dissolve, or destroy each other. Polycrystalline silicon (Polysilicon, as structural layer) and phosphosilicate glass (PSG, as sacrificial layer) are the most established materials in such applications due to polysilicon’s good mechanical properties [27], and PSG’s high etching rate in HF solutions [31], [34]. However, the mechanical property of polysilicon degrades after being exposed to HF [35], [36], so minimizing the etching time is always desired. Some designs use etching holes on the

structural layer to accelerate sacrificial etching. However, for most applications, this will affect the performance of the device or even cause a malfunction.

In this work, HF vapor is used as the etchant to remove the PSG sacrificial layer. The phosphorus doped polycrystalline silicon (Phos-Poly) circular membrane has a diameter of 106  $\mu\text{m}$ , with 8 etching channels on the edge. In a Teflon box, 15 minutes of etching time proves to be enough to effectively remove the PSG sacrificial layer without attacking the polysilicon structures.

Another big challenge to build up a free standing membrane is to avoid the diaphragm sticking to the substrate while removing liquid etchants after sacrificial material removal. For microscale devices with a small gap spacing, the stiction can cause irreversible damage. A Tousimis Model 915B Automegasamdri® CO<sub>2</sub> Critical Point Dryer (CP Dryer) has been used in this process, the membrane structures have been fully released and no stiction has been observed.

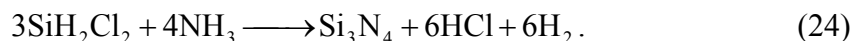
The membrane cavity is sealed by plasma enhanced chemical vapor deposition (PECVD) SiO<sub>2</sub>. Good step coverage is observed during the process and a vacuum cavity is formed. Another thick aluminum layer formed by DC sputtering acts as metal contact and connects membranes into an array system.

This work has been fabricated in the Nano Fabrication Center (NFC) at University of Minnesota. Each process step has been calibrated by test wafers for accurate processing performance.

## 4.2 Insulation Layer (Si<sub>3</sub>N<sub>4</sub>) Deposition and Pattern

New <100> n-type 4" wafers are measured with a Fowler Ultra Digit Mark IV, the average thickness of the wafers is 520um. Then the wafers have been cleaned by RCA solutions and sulfuric acid/hydrogen peroxide solution (piranha, 120°C, 10 minutes) to remove any organic, ionic and metallic contaminants. After rinsing and drying the sheet resistance of the wafers are obtained by 4-point probe as 0.3Ω/□.

The insulation layer Si<sub>3</sub>N<sub>4</sub> was deposited by LPCVD at 840°C. The deposition pressure was set as 300mTorr with 20 standard cubic centimeters (sccm) dichlorosilane (DCS) and 80 sccm ammonia gas (NH<sub>3</sub>), the reactants that can produce the thin silicon nitride film are listed in Eq. 24.



After 130 minutes deposition, the thickness of the Si<sub>3</sub>N<sub>4</sub> film was measured by a Nanospec as 5100Å.

The wafers were prebaked on a hotplate at 115°C for 2 minutes, then they were put into a Teflon box for HMDS vapor for 3 minutes. The negative photoresist Futurrex NR7-1500P has been spun on the wafers at 3000rpm for 30 seconds, which gives a thickness of about 1.2um. Then the wafers are softbaked on a hotplate at 150°C for 90 seconds. The photolithography was performed on the Karl Suss MA-6 Aligner at g-line using hard contact for a dose of 150mJ. Mask 1 was used to define the substrate electrode. The wafers were post baked on a hotplate at 100°C for 90 seconds. The photoresist was developed in RD6 developer for 10 seconds, then the wafers were rinsed in DI water and blow dried with a nitrogen gun. A

residual photoresist clean was performed by an Asher at 150W 150sccm O<sub>2</sub> for 1 minute. After that, the wafers were hardbaked on a hotplate at 120°C for 1 minute.

The Si<sub>3</sub>N<sub>4</sub> insulation layer was etched by a STS plasma etcher, which is characterized as Reactive Ion Etching (RIE). The recipe named PJSNITD has been used and parameters were set as: Ar 50sccm, CF<sub>4</sub> 40sccm, SF<sub>6</sub> 10sccm at 75mTorr, the RF Power was set as 150W. The etching took 8min with a etch rate of ~777Å/min. The an O<sub>2</sub> clean was performed in the STS etcher for 5 minutes.

The photoresist was removed by acetone in an ultrasonic bath for 5 minutes. Then the wafer went through methanol and IPA (isopropyl alcohol) baths for 3 minutes each, and then rinsed and dried. A piranha clean was performed again.

The defined substrate electrode is shown in Fig. 22.

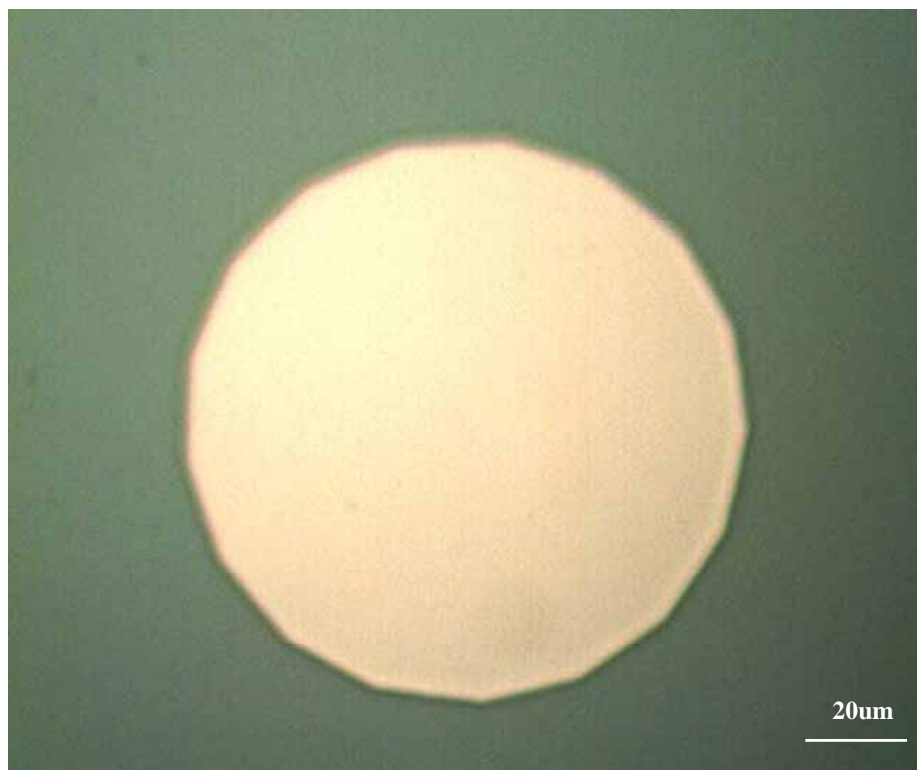
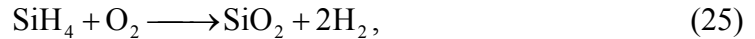


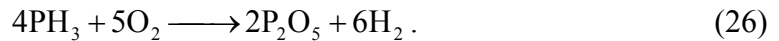
**Fig. 22. Substrate electrode defined by LPCVD Si<sub>3</sub>N<sub>4</sub>.**

### 4.3 Sacrificial Layer (PSG) Deposition and Pattern

The sacrificial layer of LPCVD PSG has been deposited at 425°C. The deposition pressure is 300mTorr with 90 sccm oxygen (O<sub>2</sub>), 70 sccm silane (SiH<sub>4</sub>) and 118 sccm 15% phosphine (PH<sub>3</sub>) in H<sub>2</sub> flow. The chemical reactions are:



and



After 2 hours deposition, the thickness for PSG was measured by a Nanospec at about 2µm. There is about 15% uniformity across the wafer and 4% uniformity across the boat. Since this PSG layer will be covered by a polysilicon layer which is deposited at a higher temperature than the PSG deposition temperature, this PSG layer was annealed at 950°C in a Tylan® Furnace System for 1 hour with 2 sccm nitrogen (N<sub>2</sub>) in order to densify it. After that, the thickness was measured again, and it shrank about 1%. The final thickness is still larger than designed, however then each wafer was etched in BOE for different lengths of time, and resulted in a thickness range of 1.2~2.1µm for different wafers.

The wafers were prebaked on a hotplate at 105°C for 2 minutes, and put in a Teflon box for 3 minutes for HMDS vapor. The photoresist Shipley 1818 was spun at 3000rpm for 30 seconds resulting in a thickness about 2.1µm. Then the wafers are softbaked at 115°C for another 2 minutes. Mask 2 was used to define the sacrificial layer. Photolithography was performed on a Karl Suss MA-6 at g-line using soft contact at a dose of 102mJ. The wafers were postbaked on a hotplate at 105°C for 1 minute, and the photoresist was developed in 351 developer (351:H<sub>2</sub>O=1:5) for 1 minute. Then the wafers were rinsed in DI water and blow

dried with a nitrogen gun. A residual photoresist clean was performed by an Asher at 150W 150sccm O<sub>2</sub> for 2 minute. The wafers were hardbaked in an oven at 120°C for 30 minutes, the reason to uses an oven instead of a hotplate is to harden the photoresist and avoid them peeling off in Buffered Oxide Etchant (BOE). This PSG layer then was etched in a 10:1 BOE solution for 13 minutes with an etch rate of 2100A/min, then the photoresist was removed by Acetone-Methanol-IPA. Another piranha clean was performed again.

The patterned PSG layer is shown in Fig. 23, and the etching channels have a width of about 20  $\mu\text{m}$ . The circular area of the PSG defined by a mask is larger than the substrate electrode, which compensates for wet-etching undercut of PSG and to avoid the polysilicon membrane contacting the substrate. One merit for using wet-etching (isotropic) here is to provide a slope, which is easy to be covered by LPCVD polysilicon.

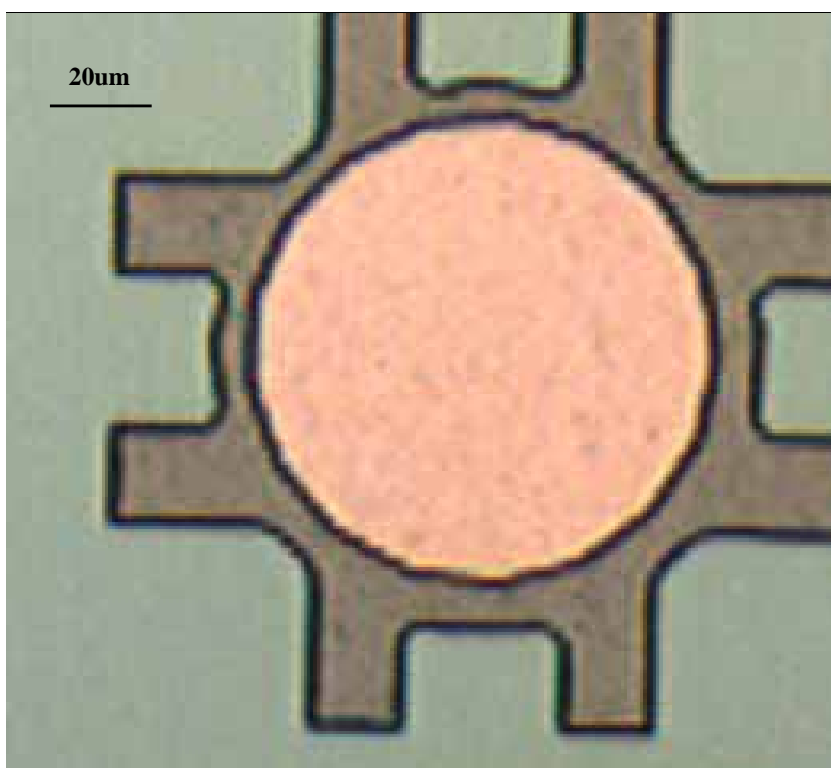


**Fig. 23. Sacrificial layer defined by LPCVD PSG.**

#### 4.4 Structure Layer (Phos-poly) Deposition and Pattern

The Phos-Poly layer was deposited by stacking up doped polysilicon layers and regular polysilicon layers using LPCVD, since Phos-Poly has a very low deposition rate (~25 Angstrom/minute). The actual deposition time is shown in Table III. This LPCVD process built up a symmetrical stack up of doped and undoped polysilicon (Fig. 24). The Phos-Poly was deposited at 640°C with 4 sccm PH<sub>3</sub> and 124.8 sccm SiH<sub>4</sub>, the deposition pressure is 250mTorr. The regular LPCVD polysilicon was deposited at 616°C without PH<sub>3</sub> flow. The chemical reactions are shown as below:



Deposited Layer	Phos-Poly (~25A/min)	Undoped Poly (~115A/min)	Phos-Poly (~25A/min)	Undoped Poly (~115A/min)	Phos-Poly (~25A/min)
Deposition Time	66min	48min	66min	48min	66min

**Table 4. Phos-poly deposition time.**

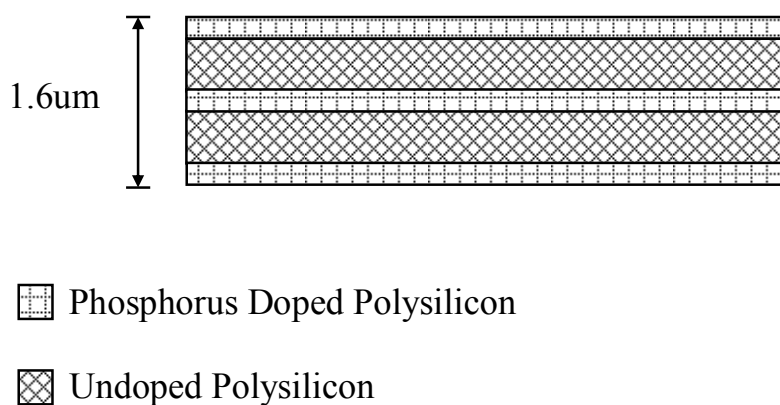


**Fig. 24. Polysilicon membrane layer stack up.**

The thickness of the stack-up polysilicon was measured under a Nanospec as 1.6 $\mu$ m. The thicker layer can actually compensate any degradation of the polysilicon, and the layer can be etched later to get the best performance. The electrical conductivity was measured by a 4-point probe as about 240 $\Omega/\square$ . The residual stress was measured by the Film Stress Measurement (FSM-900TC) as -374MPa.

The wafers with polysilicon layer were annealed by Rapid Thermal Annealing (RTA) at 1100°C with 10SLPM HiN<sub>2</sub> flow for 1 minute. Then the conductivity and film stress became 33.6 $\Omega/\square$  and -140MPa, respectively. The thickness of the polysilicon still remains the same. Here we can see how the RTA helps to release the residual stress and increase the phosphorus doping level.

The wafers were prebaked on a hotplate at 105°C for 2 minutes, and put in a Teflon box for 3 minutes for HMDS vapor. The photoresist Shipley 1818 was spun at 3000rpm for 30 seconds resulting in a thickness about 2.1 $\mu$ m. Then the wafers were softbaked at 115°C for another 2 minutes. Mask 3 was used to define the Phos-poly membranes. Photolithography was performed on a Karl Suss MA-6 at g-line using soft contact at a dose of 102mJ. The wafers were postbaked on a hotplate at 105°C for 1 minute, and the photoresist was developed in 351 developer (351:H<sub>2</sub>O=1:5) for 1 minute. Then the wafers were rinsed in DI water and blow dried with nitrogen gun. A residual photoresist clean was performed by an Asher at 150W 150sccm O<sub>2</sub> for 2 minute. The wafers were hardbaked in an oven at 120°C for 30 minutes.

Mask 3 was used to define the Phos-poly membrane layer. A Deep Trench Plasma Etcher, which is characterized as Deep Reactive Ion Etching (DRIE), was used to pattern polysilicon. It is a highly anisotropic etching process used to create deep, steep-sided holes

and trenches in wafers, with aspect ratios of 20:1 or more. In this project, a Bosch recipe was run for 8 loops, and the photoresist was removed by Acetone-Methanol-IPA. Residual photoresist was observed at the corner of the polysilicon sidewall, another O<sub>2</sub> plasma clean was performed in a STS etcher to fully remove any residual photoresist.

The polysilicon layer defined by a mask has a diameter of 130  $\mu\text{m}$ , which also provides the membrane stands. The membrane itself has a diameter of 106  $\mu\text{m}$  with 8 etching channels with a width of 20  $\mu\text{m}$ . The views under a microscope are shown in Fig. 25 and 26. A Hyphenated Systems HS200A Confocal Microscope® has also been used to examine the membrane structure. A confocal microscope is able to eliminate the out-of-focus information using a pinhole in front of the image plane, by taking multiple pictures with a different focus, the surface portfolio and 3D pictures have been obtained (Fig. 27 and 28).

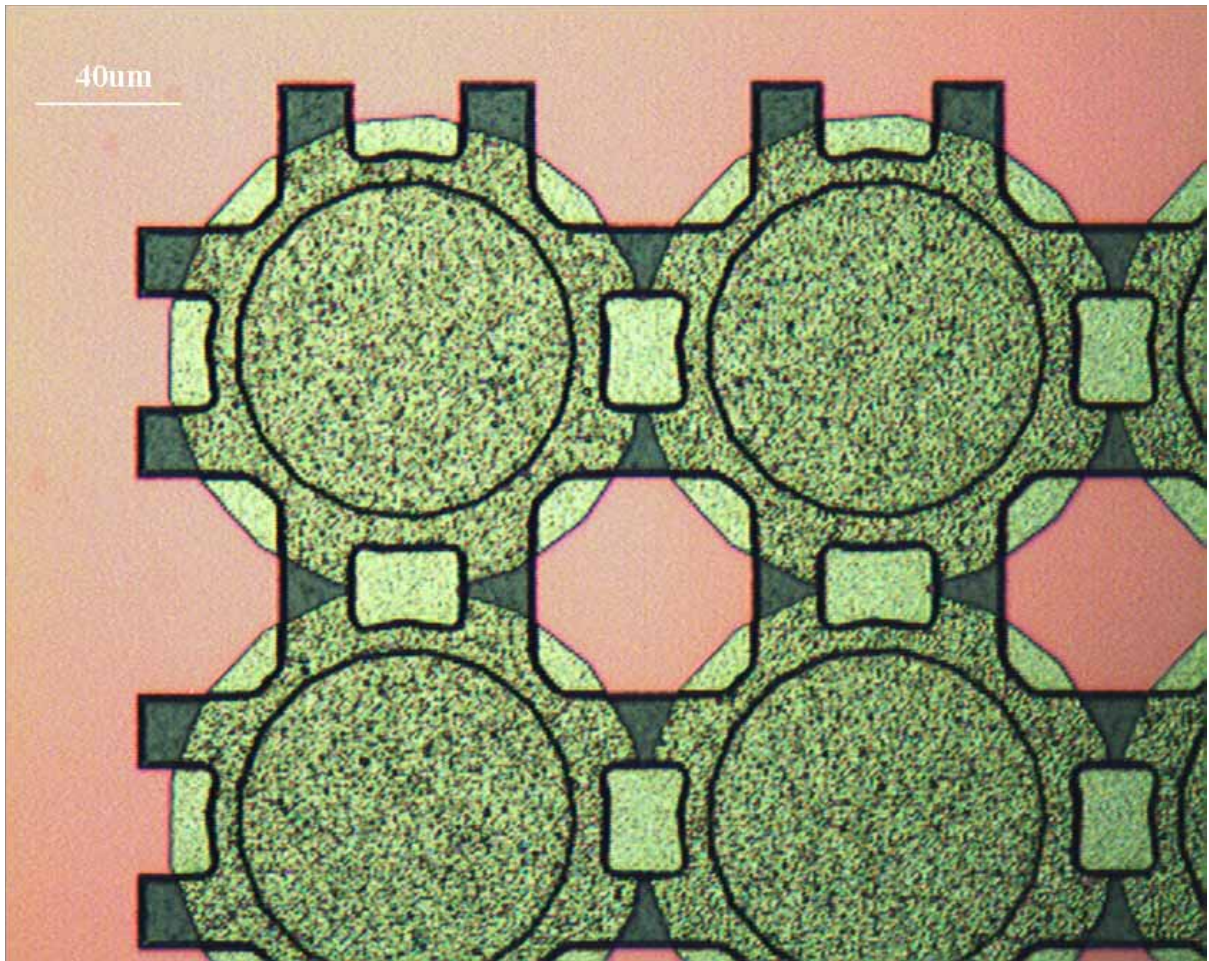
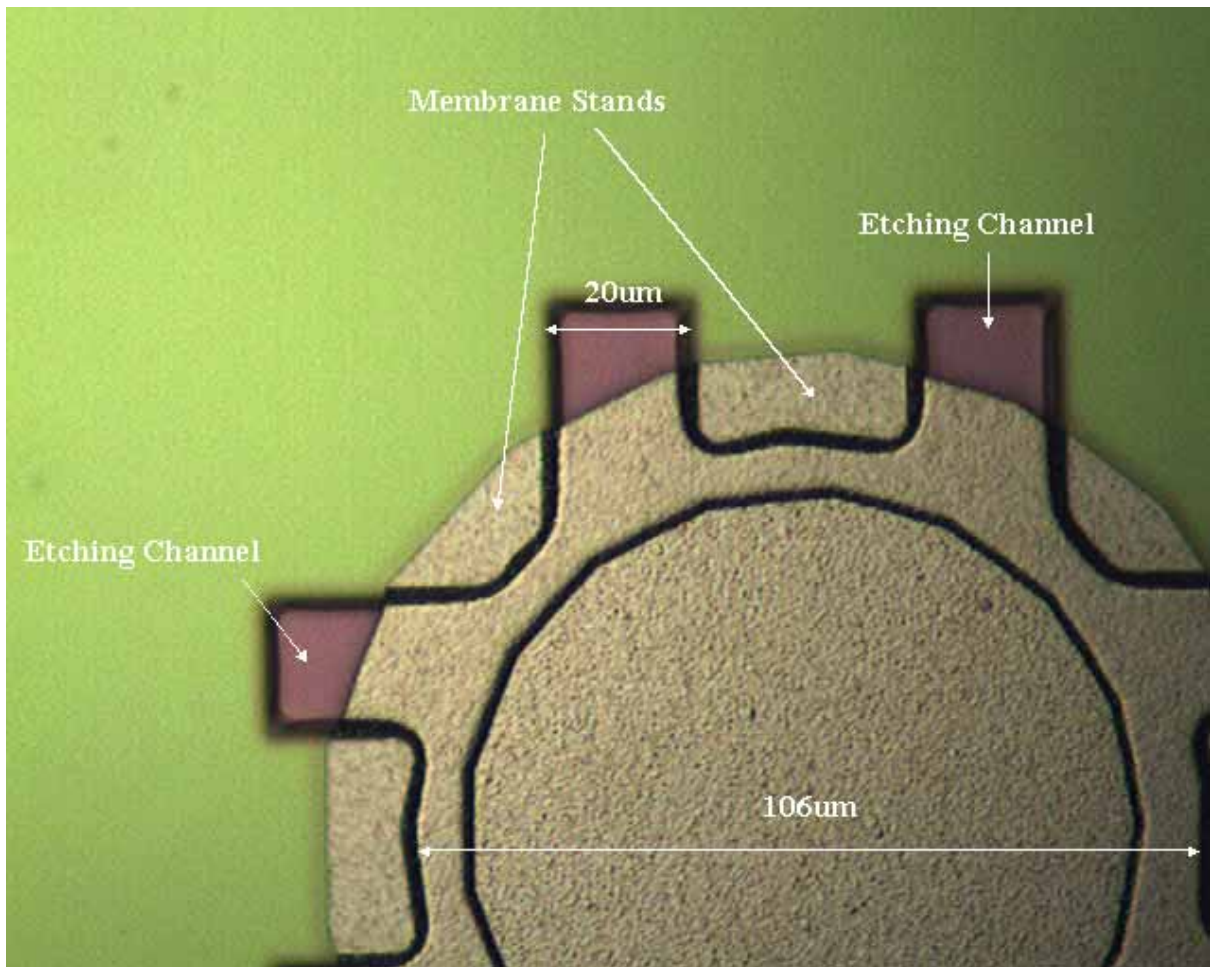


Fig. 25. Phos-Poly membrane array with PSG etching channels.



**Fig. 26. One Phos-Poly membrane with PSG etching channels.**

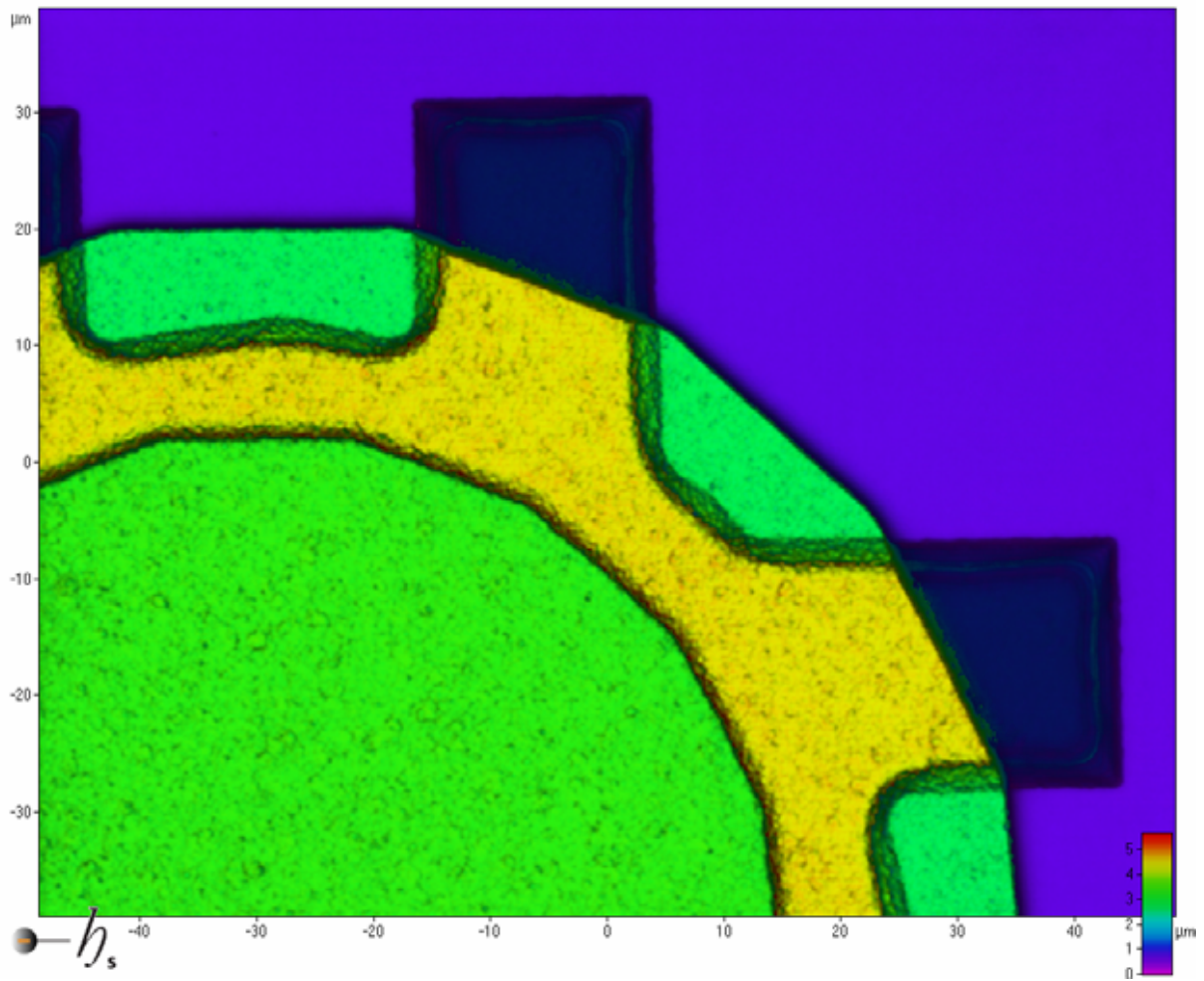
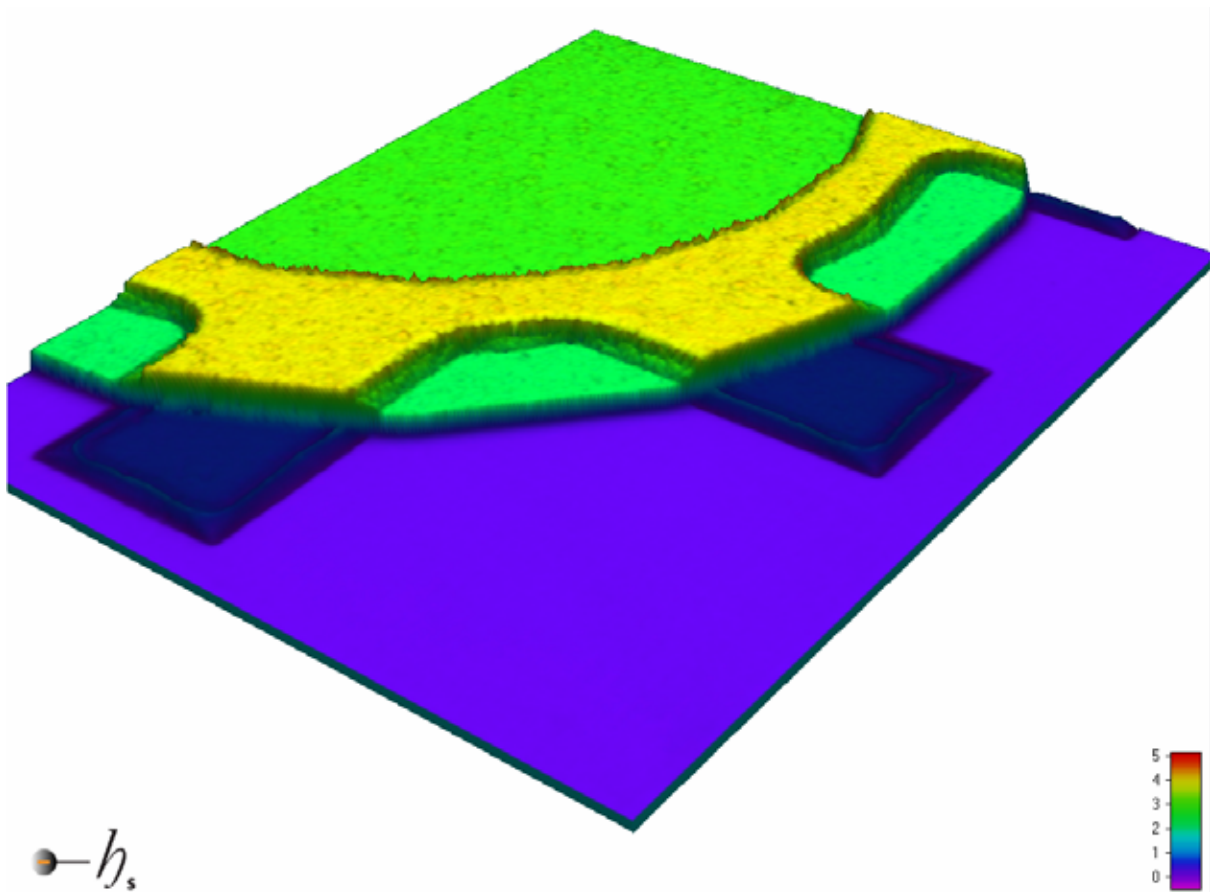


Fig. 27. Surface portfolio of one Phos-Poly membrane taken by confocal microscope.



**Fig. 28.** A 3D view of one Phos-Poly membrane taken by confocal microscope.

#### 4.5 HF Vapor Sacrificial Etching

The sacrificial etching process simply involves one Teflon box and a Teflon stand. The box was filled with a small portion of concentrated HF acid (49%) with a height of 4 centimeters. A Teflon stand then was submerged into the HF acid to provide a support for the wafer boat. The membrane sample wafers were put into the Teflon box with a Teflon cover for 15 minutes. Then the wafers were put into 10:1 BOE for 1 minute to remove any residual PSG, and rinsed 3 times in Methanol and Isopropyl Alcohol (IPA) prior to CPD releasing.

## 4.6 Critical Point Drying (CPD)

A Tousimis Model 915B Automegasamdri® CO<sub>2</sub> Critical Point Dryer (CP Dryer) uses liquid carbon dioxide (CO<sub>2</sub>) to replace the solvent used in the last rinse process. The pressure and heat are then increased to change the liquid carbon dioxide (LCO<sub>2</sub>) to a gas. The pressure is slowly decreased to atmosphere thereby not allowing carbon dioxide to condense. The lack of the liquid/vapor stage allows for the minimizing stiction in the membrane release. The membrane structure wafers were covered by IPA in the CP Dryer and a 15 minute purge time has been set for 1/4 chamber full of IPA.

A single Phos-Poly membrane and membrane arrays have been successfully released. The released structures are shown in Fig. 29 and 30. The diaphragm area is flat and no stiction has been observed. A wafer probe has been used to check whether the PSG layer has been fully etched. In our design, the PSG could remain in the center under the membrane if it has not been etched long enough (Fig. 31). The wafer probe applied a large pressure on the diaphragms among different positions on the wafer to make them peel off, the diaphragms can be broken very easily and no remaining PSG has been observed after the Phos-Poly diaphragms are gone (Fig. 32). Surface portfolio and 3D view of released membrane structures have been obtained again by a Hyphenated Systems HS200A Confocal Microscope® (Fig. 33 and 34). The different thickness of Si<sub>3</sub>N<sub>4</sub> from Fig. 27 is perhaps caused by attack of HF Vapor.

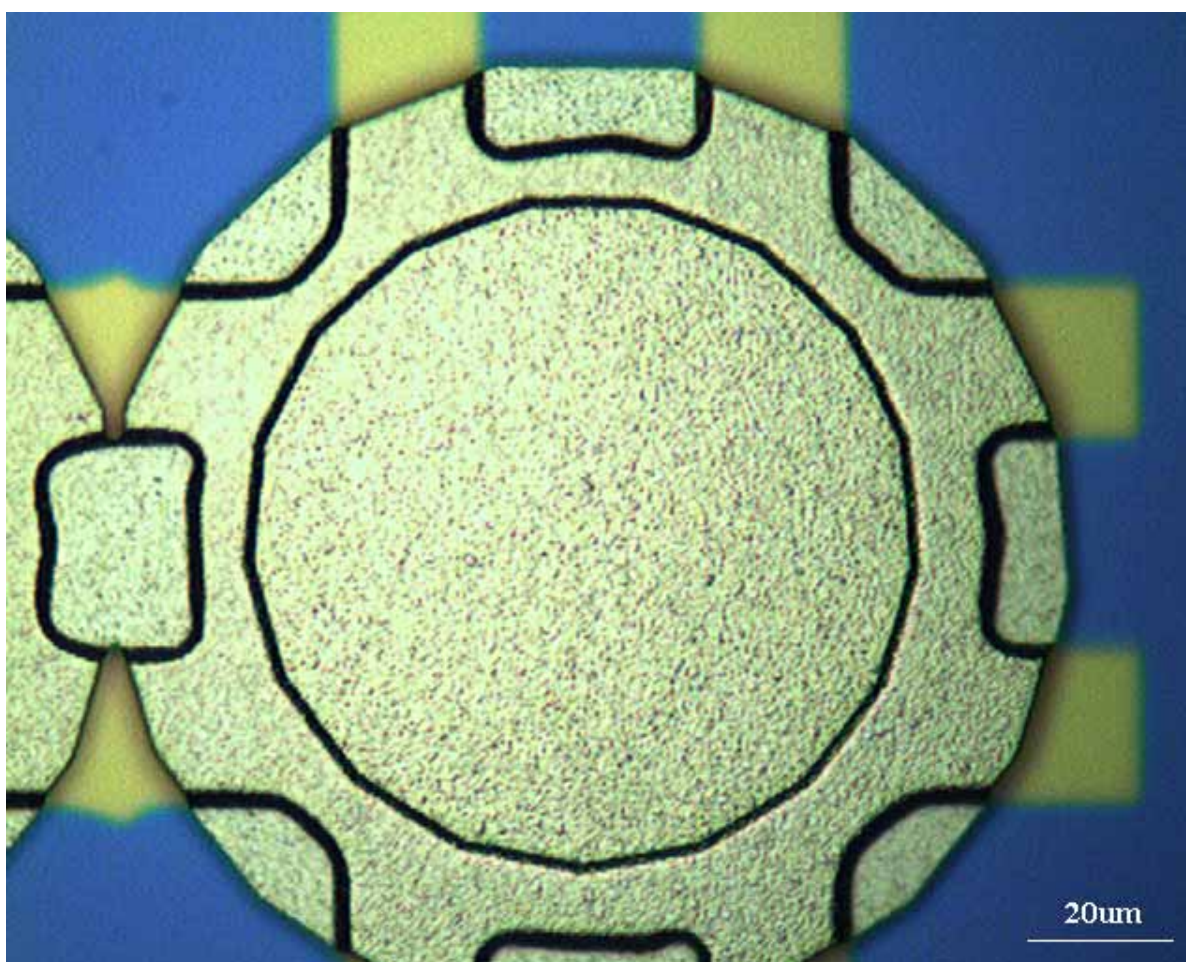


**Fig. 29. Released Phos-Poly membrane.**

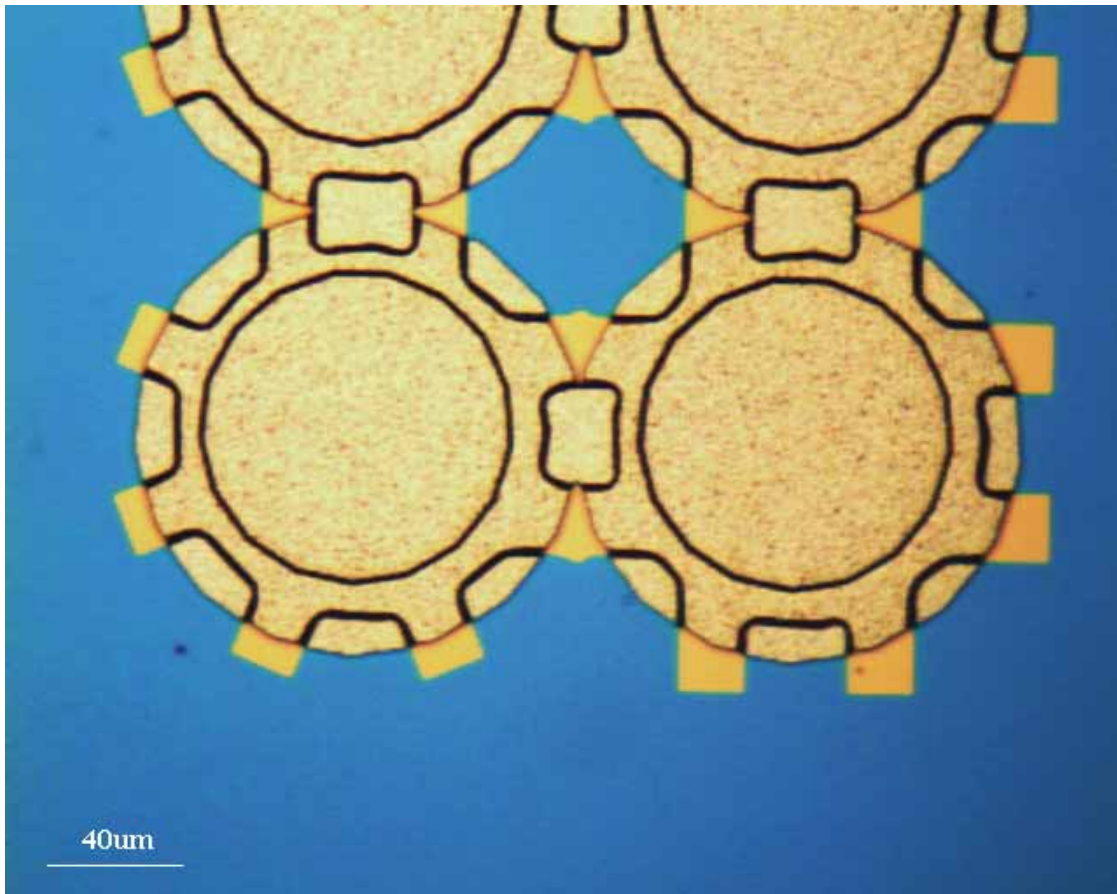


Fig. 30. Released Phos-Poly membrane array.

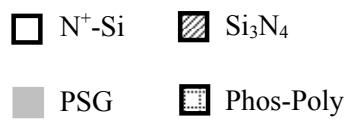
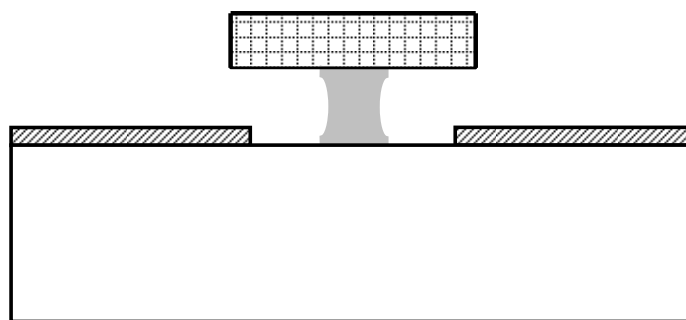
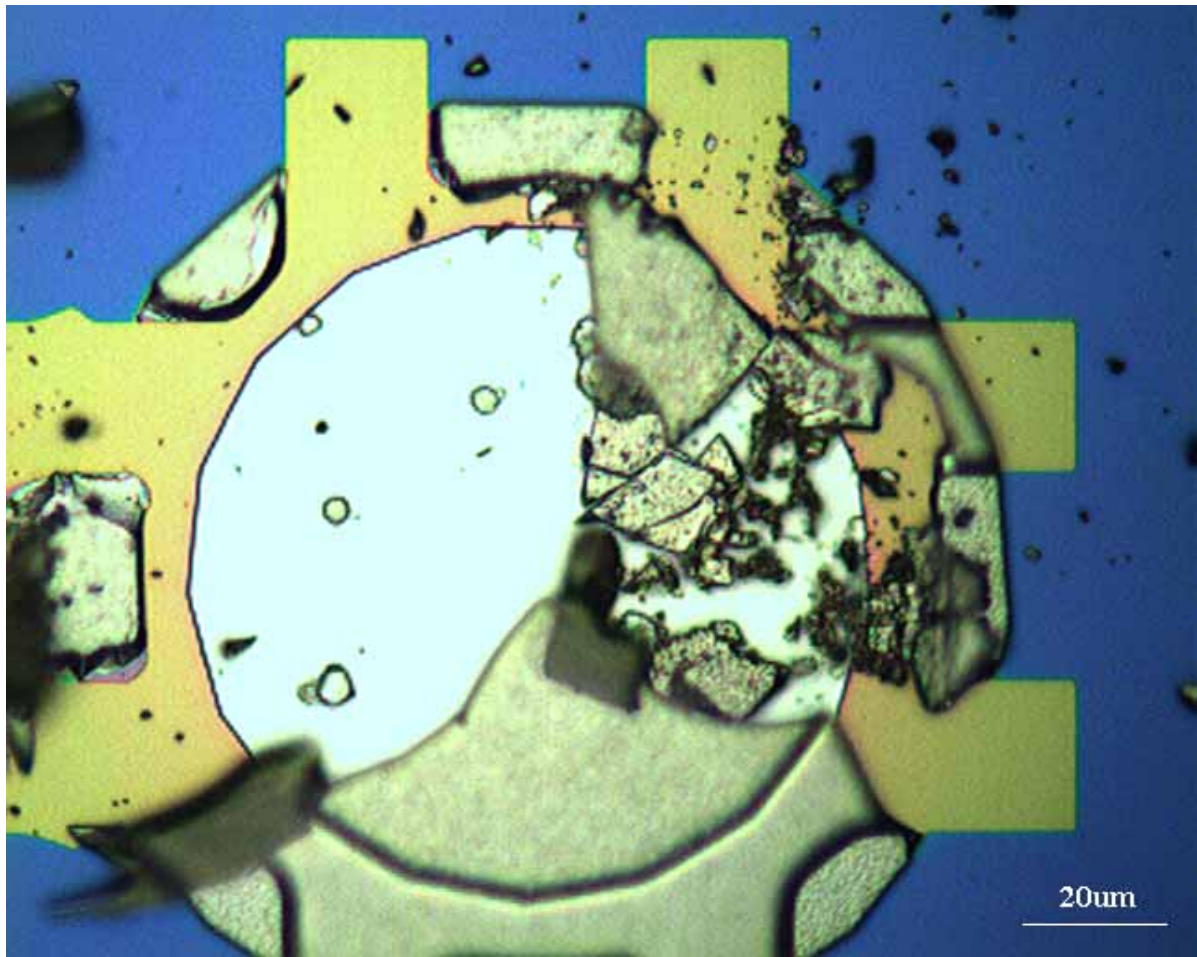
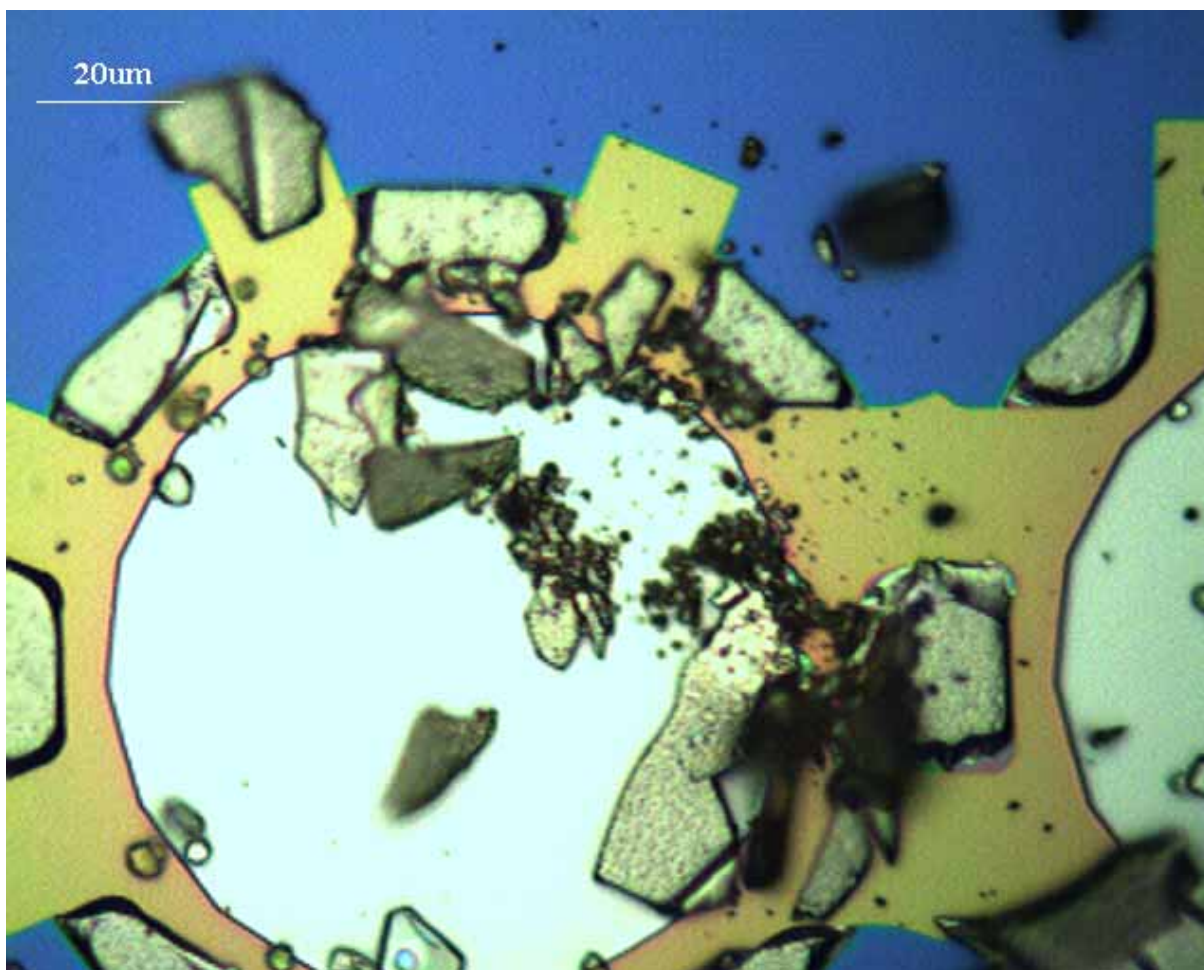


Fig. 31. Unreleased polysilicon membrane with PSG underneath.



(a)



(b)

**Fig. 32. Broken Phos-Poly membranes with no PSG underneath.**

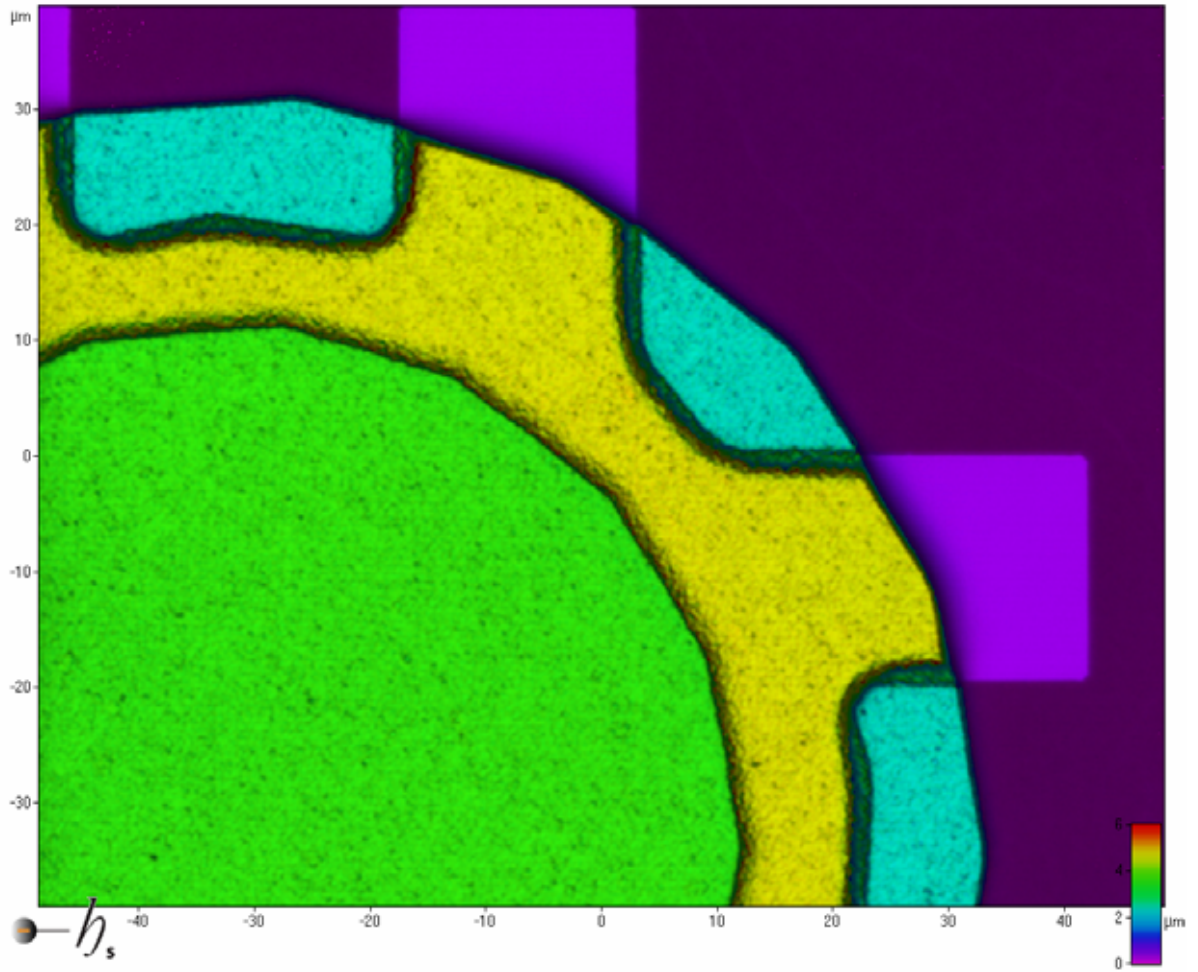


**Fig. 33. Released Phos-Poly membrane taken by confocal microscope.**

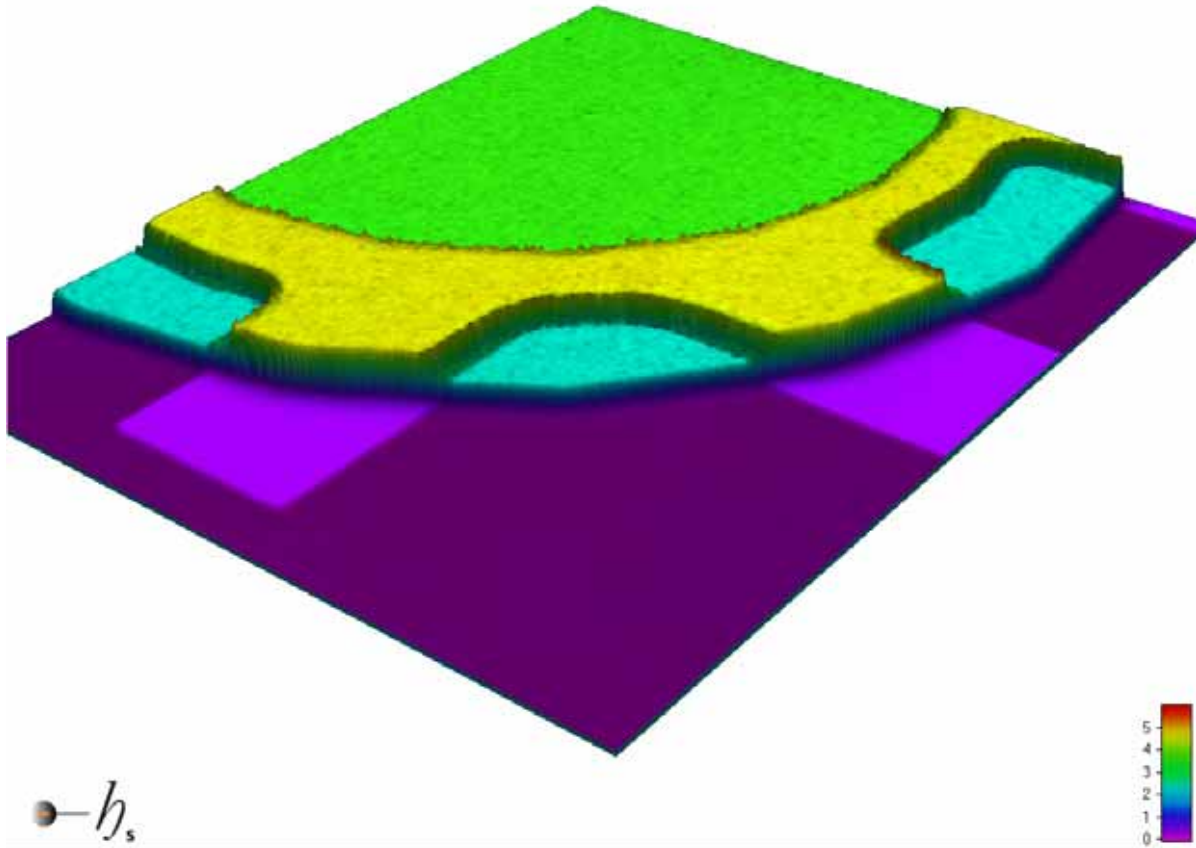


Fig. 34. A 3D view of released Phos-Poly membrane taken by confocal microscope.

#### 4.7 Cavity Sealing ( $\text{SiO}_2$ )

Since the maximum height of the membrane is larger than 2.5 $\mu\text{m}$ , in order to seal the cavity channel properly, a thick layer at least 3 $\mu\text{m}$  is need. LPCVD has better film quality but lower deposition rate, so it is not suitable for cavity sealing anymore. This project uses Plasma Enhanced Chemical Vapor Deposition (PECVD)  $\text{SiO}_2$  due to the fast deposition rate. The  $\text{SiO}_2$  layer has been deposited in PECVD system at 340°C for 90 minutes, the pressure has been set for 900mTorr with 200 sccm 2%  $\text{SiH}_4$  in He and 450 sccm  $\text{N}_2\text{O}$ , the RF power is

20W. The thickness was measured as 3.1825 $\mu\text{m}$ , which indicates a deposition rate of 353.62 $\text{\AA}/\text{min}$ .

The wafers were prebaked on a hotplate at 105°C for 2 minutes, and put in a Teflon box for 3 minutes for HMDS vapor. The photoresist SPR 220-4.5 was spun at 2000rpm for 90 seconds resulting in a thickness of about 6 $\mu\text{m}$ . Then the wafers were softbaked at 115°C for 90 seconds with 30 seconds ramping up on a hotplate. Mask 4 was used to define the sealing rings. Photolithography was performed on a Karl Suss MA-6 at g-line using soft contact at a dose of 432mJ. Since the photoresist is thicker than the normal case, the wafer was left on hold for 1 hour to allow the water to diffuse for this particular photoresist. The wafers were postbaked on a hotplate at 105°C for 2 minute, and the photoresist was developed in MF-CD-26 developer for 90 seconds. Then the wafers are rinsed in DI water and blow dried with nitrogen gun. A residual photoresist clean was performed by an Asher at 150W 150sccm O<sub>2</sub> for 2 minute. The wafers were hardbaked on a hot plate at 105°C for another 5 minutes.

The etching process combines both dry etching and wet etching techniques. Since the SiO<sub>2</sub> layer is larger than 3 $\mu\text{m}$ , if only wet etching is used, the longer time in BOE will peel off the photoresist and attack the sealing ring. Dry etching has a lower etch rate but also lower risk to attack the photoresist. The dry etching combines recipe PJNITD (10 minutes) and PJOXID (6 minutes) in a STS plasma etcher to etch down 60% of the SiO<sub>2</sub>, then the 10:1 BOE was used for 7 minutes to get a faster etch rate and better selectivity. The photoresist was removed by Acetone-Methanol-IPA and O<sub>2</sub> plasma clean.

The sealed membrane is shown in Fig. 35, good step coverage is observed at the joint of the two membranes.

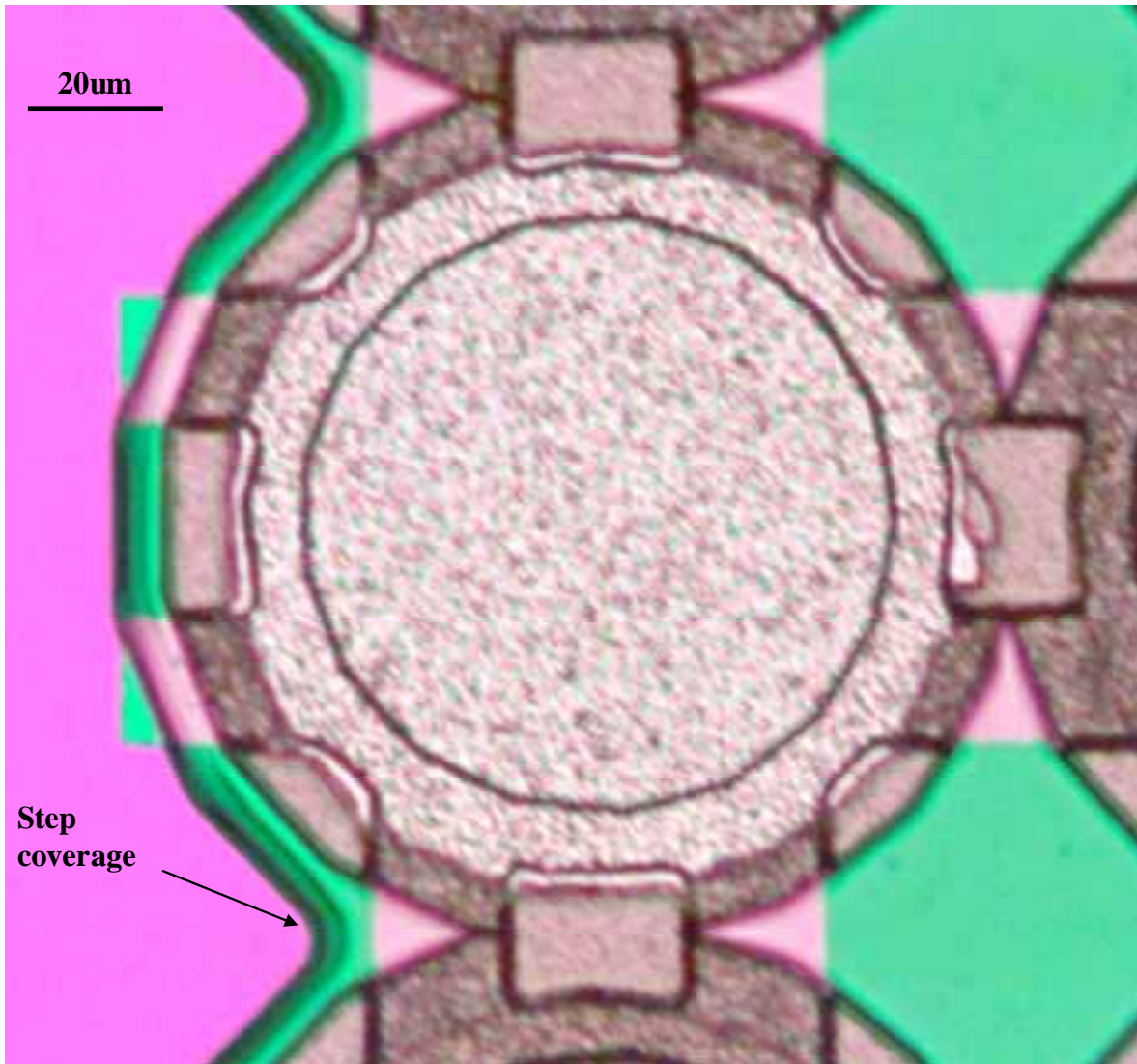


Fig. 35. Sealed membranes.

## 4.8 Metal Contact (Aluminum)

As discussed above, all the thick layers require a thick metal layer for the electrical contact. A DC Sputter (Perkin Elmer 2400) has been used to deposit an aluminum layer due to its rapid deposition rate. The deposition condition is 10sccm Argon (Ar), 5kW power (ramp up 2 minutes) at 6mTorr. The system was pre-sputtered for 2 minutes. The wafer was rotated at a speed of about 3rpm, The total deposition time is 34 minutes, which gives a thickness of about 3 $\mu$ m.

This thick metal was measured as 0.0252 $\Omega/\square$  electrical conductivity. The wafer was annealed by RTA at 400°C for 30 seconds to condense the aluminum, and the electrical conductivity was measured again as 0.0213 $\Omega/\square$ .

The wafers were prebaked on a hotplate at 105°C for 2 minutes, and put in a Teflon box for 3 minutes for HMDS vapor. The photoresist Shipley STR 1045 was spun at 1500rpm for 43 seconds resulting in a thickness about 7.8 $\mu$ m. Then the wafers were softbaked at 105°C for 30 minutes in an oven. Several experiments have been done to do the softbake on a hotplate, however due to the different thermal expansion of metal and photoresist, the photoresist peeled off after developing. Baking in an oven allows the photoresist reflow and it remained firmly attached to the aluminum. Mask 5 was used to define the aluminum contact. Photolithography was performed on Karl Suss MA-6 at g-line using soft contact at a dose of 444mJ. The photoresist was developed in 351:H<sub>2</sub>O(1:5) developer for 3 minutes. Then the wafers are rinsed in DI water and blow dried with nitrogen gun. A residual photoresist clean was performed by an Asher at 200W 150sccm O<sub>2</sub> for 15 seconds, here a short O<sub>2</sub> plasma cleaning time is needed to avoid oxidizing the aluminum. The wafers were hardbaked on a hot plate at 105°C for another minute.

The aluminum layer was etched by Al etching recipe of  $\text{H}_3\text{PO}_4:\text{HNO}_3:\text{HAc}:2\text{H}_2\text{O}=16:1:1$  at  $50^\circ\text{C}$  for 6 minutes in a glass box. The photoresist was removed by Acetone-Methanol-IPA solution.

At this point, the IOP sensor model has been successfully fabricated (Fig. 36, 37). The fabrication diagram is in Fig. 38 and a detailed fabrication flow is summarized in Appendix B.

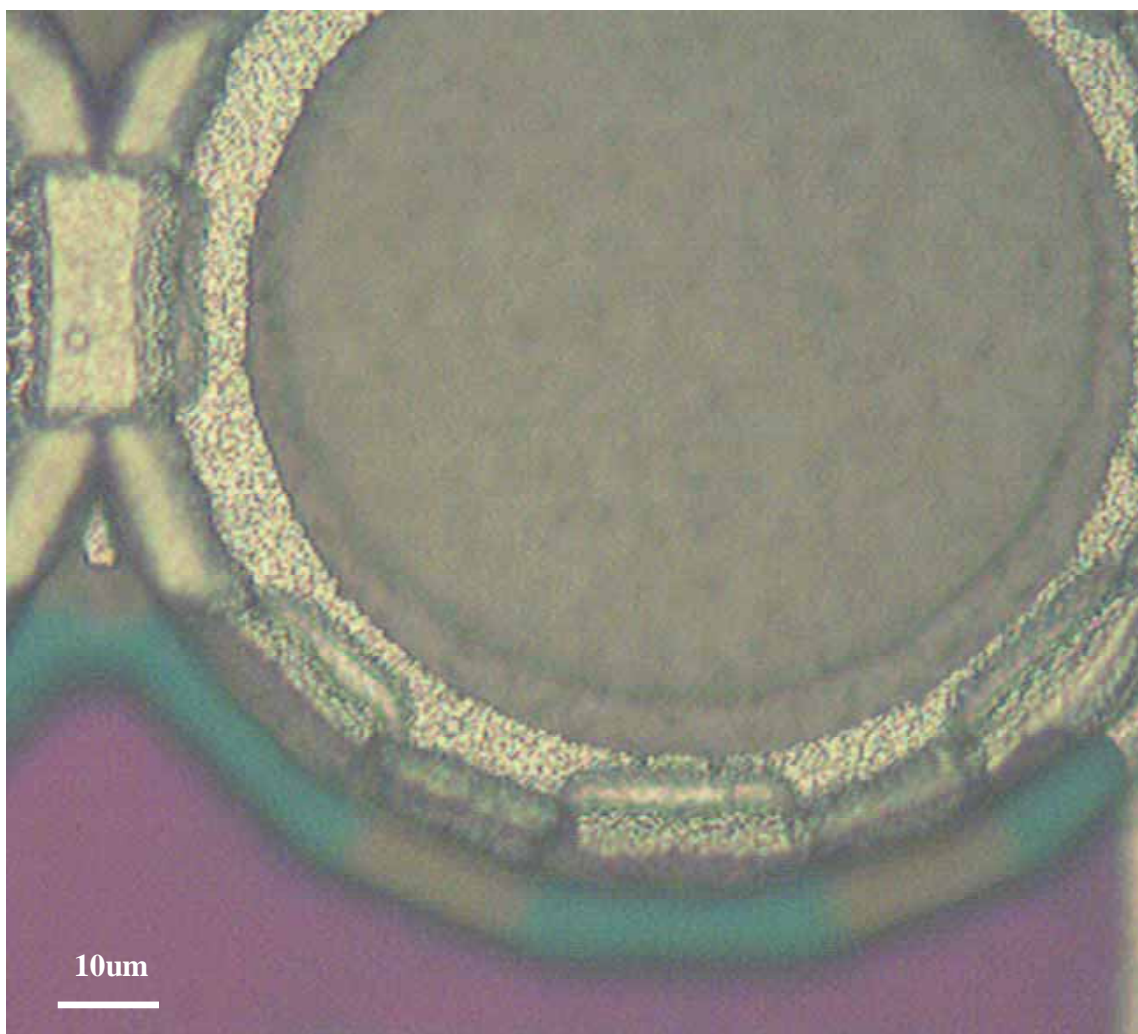


**Fig. 36. One membrane after Al pattern.**

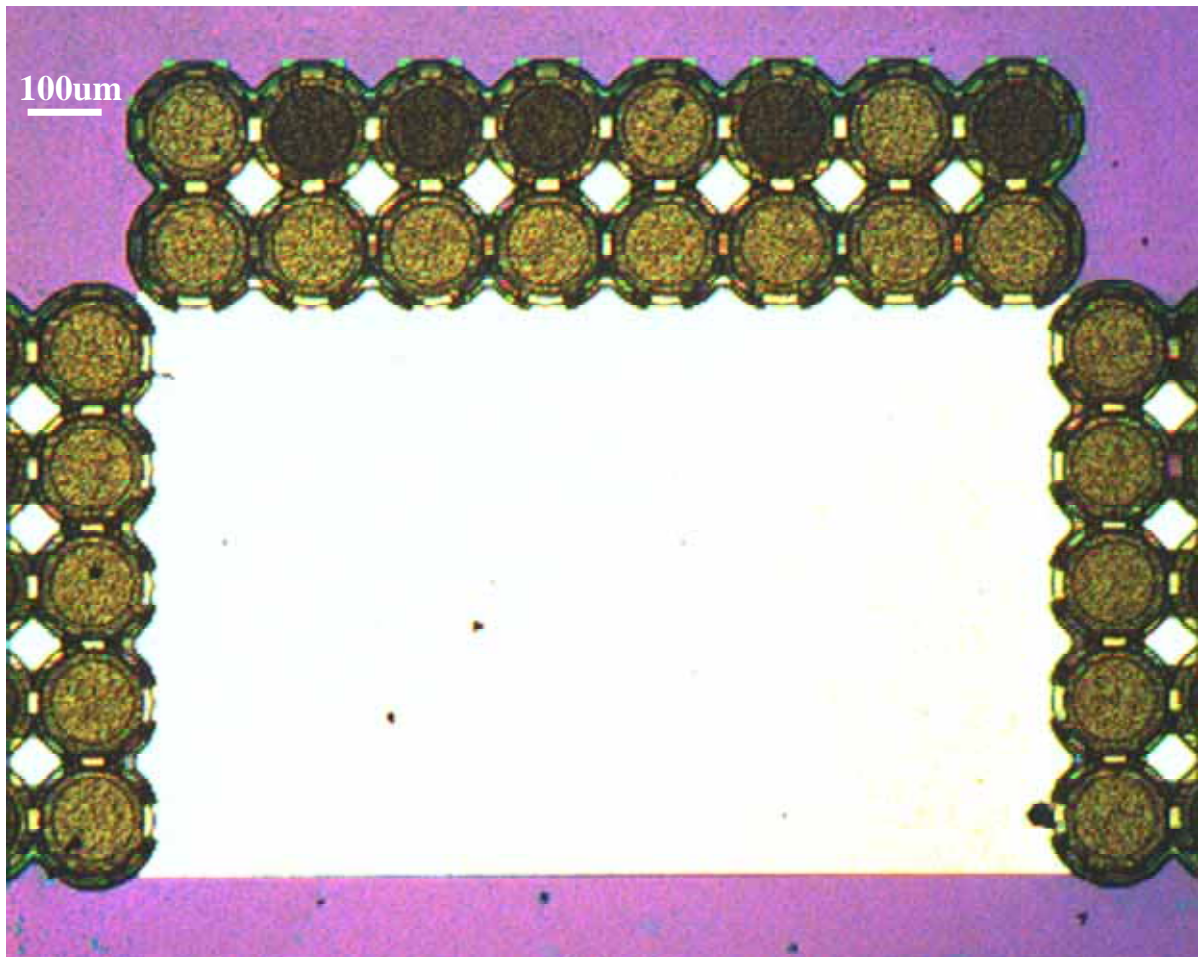
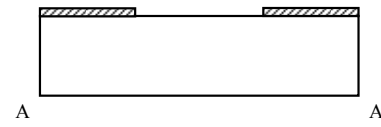
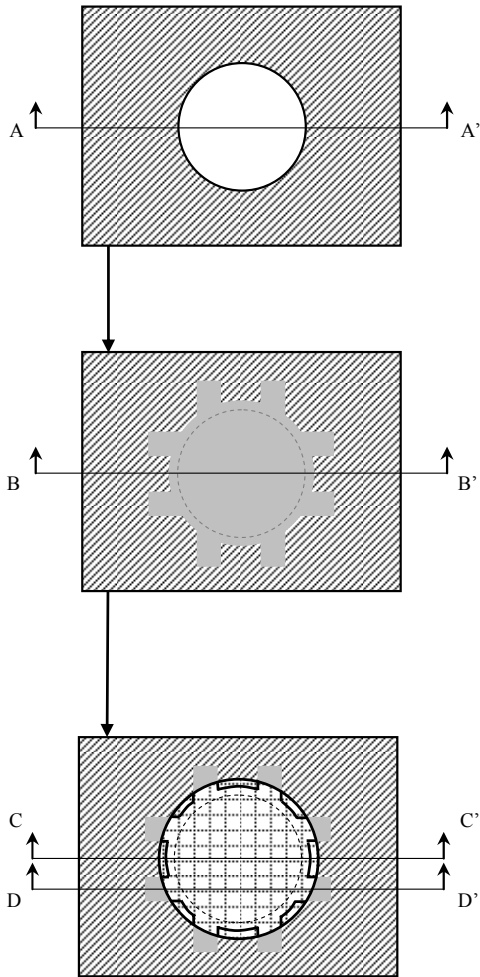
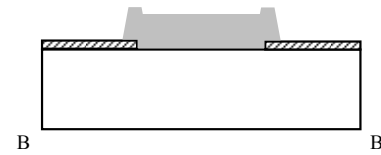


**Fig. 37. Membrane array after Al pattern.**



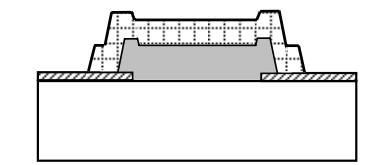
Deposit and pattern 0.5um LPCVD  $Si_3N_4$

(a)



Deposit and pattern 2um LPCVD PSG sacrificial layer

(b)



Deposit 1.6um LPCVD polysilicon stack up.

Annealed at 1100oC by RTA.

Patterned by Deep Trench Plasma Etching.

(c)

- N<sup>+</sup>-Si
- $Si_3N_4$
- PSG
- N<sup>+</sup> Poly
- $SiO_2$
- Al

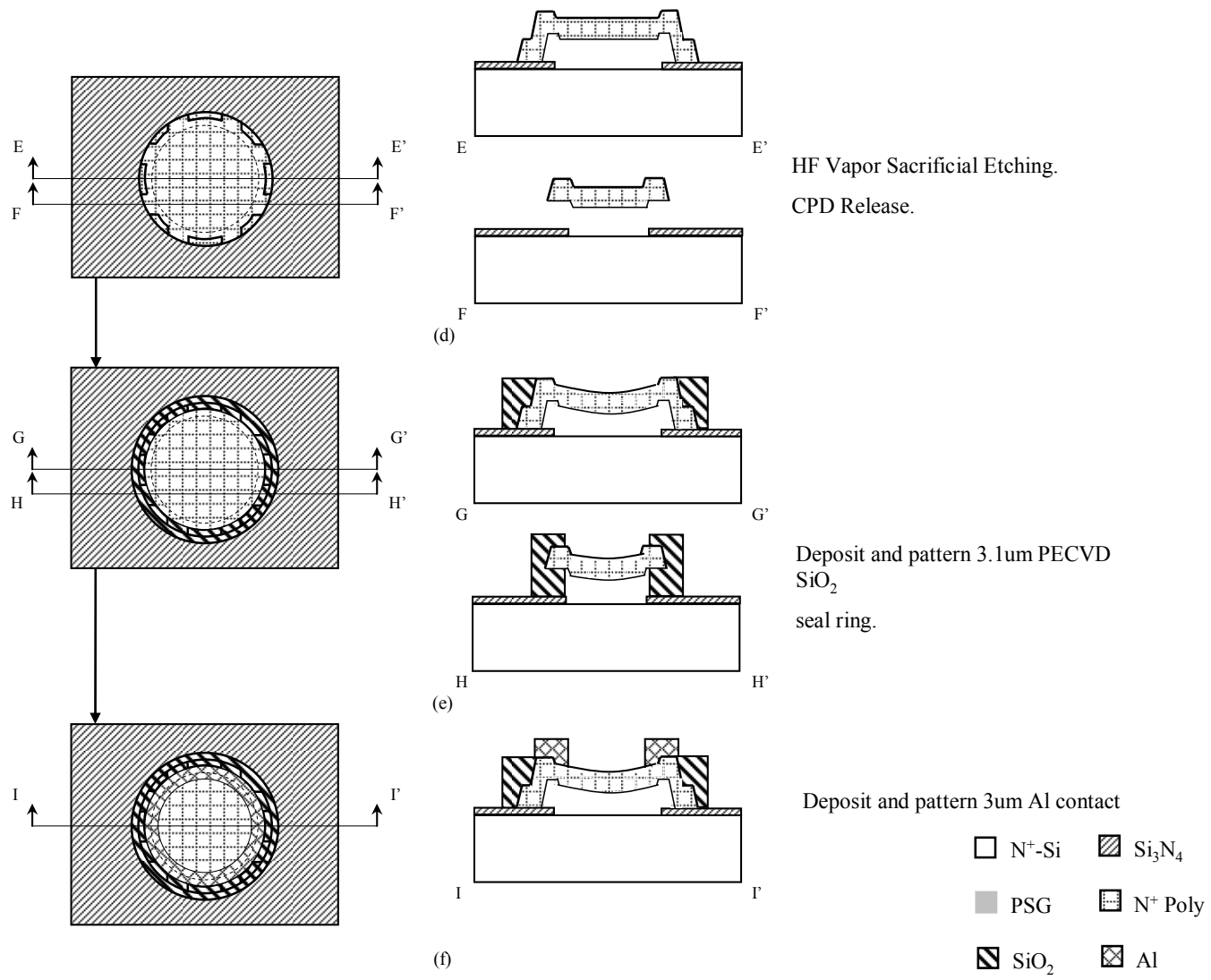


Fig. 38.IOP sensor fabrication flow.

## CHAPTER 5. INTRAOCULAR PRESSURE (IOP) SENSOR MEASUREMENT

This chapter discusses the measurement setup and results for the IOP sensors. Different types of coil detectors have been compared, and the optimum coil detector with a high permeability core is used to measure the IOP sensor remotely. A pressure sensing system consisting of pressure chamber, pressure pump and gauge, sensor probe/coil, and HP Network Analyzer has been set up to perform IOP sensor measurement. Both probe and remote (*in vitro*) measurement have been conducted and encouraging results are discussed. The IOP sensor itself can be detected by a coil detector with a high permeability core up to 4mm distance. A novel configuration using a secondary resonator is first introduced in this project. The sensing distance can be improved to 1.5cm for the IOP sensor. This is larger than most of the existing work in this area.

### 5.1 Study of Detector and Sensor Coil

Different types of detector and sensor coils have been studied. A summary of the coils is shown in Table 5 and 6, and Fig. 39-45. Different measurements and comparisons are discussed in the following sections.

Detector #1	Detector #2	Detector #3
3.3mm(H)×3.3mm(W)	1cm diameter	5cm diameter
High permeability half cylinder core	5 turns AWG32	2 turns AWG32 enamel
5 turns AWG32 enamel coil	enamel coil	coil

**Table 5. Detector Details.**

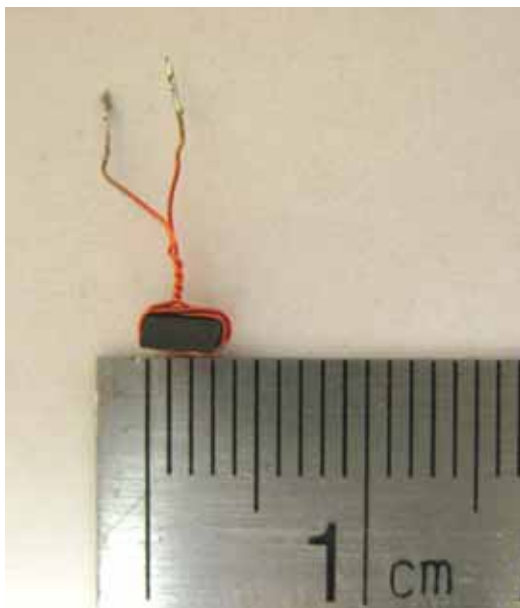


**Fig. 39. Detector #1.**

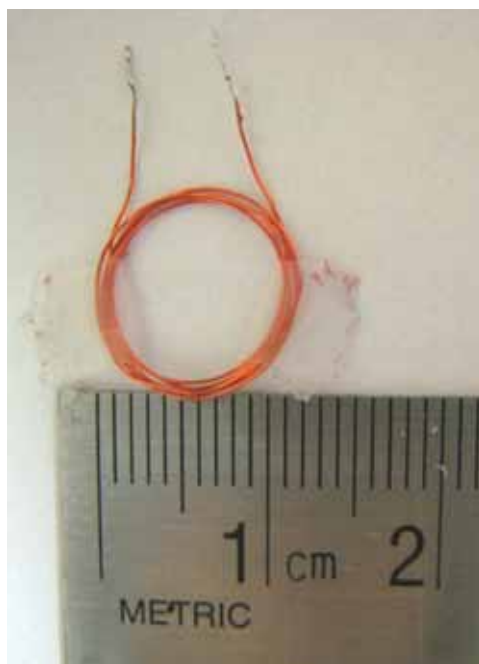


**Fig. 40. Detector #2.**

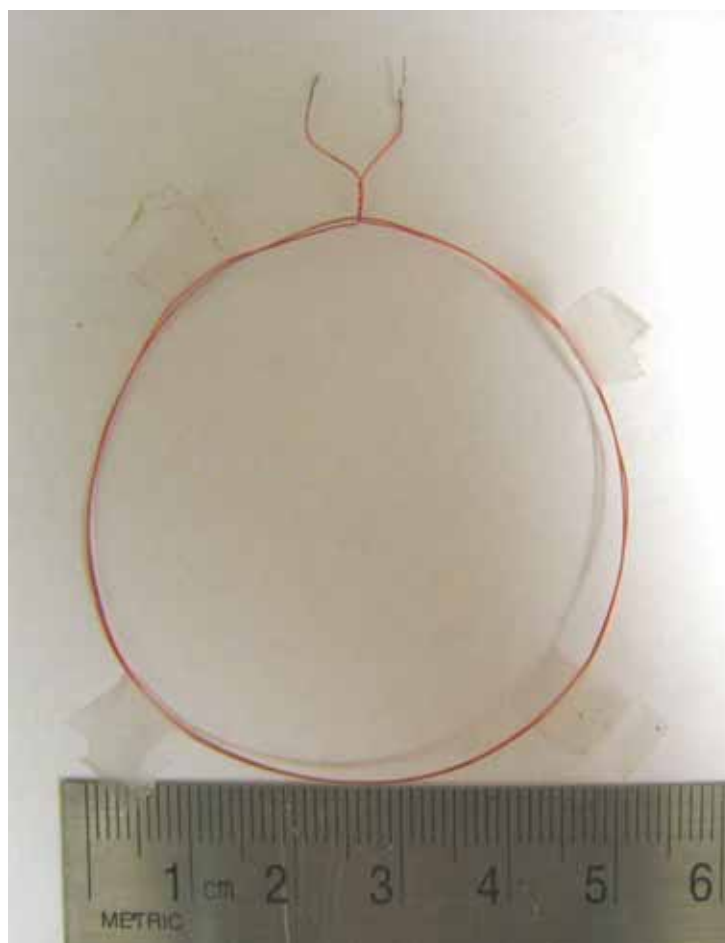


**Fig. 41. Detector #3.**

Sensor #1	Sensor #2	Sensor #3	Sensor #4
1cm diameter	1.6mm diameter	1mm diameter	0.56mm diameter
Single turn AWG32	8 turns AWG38	8 turns AWG38	8 turns AWG38
enamel coil with a	enamel coil with a 0402	enamel coil with a 0402	enamel coil with a 0402
0402 15pF capacitor	15pF capacitor	15pF capacitor	15pF capacitor

**Table 6. Sensor Kit Details.**

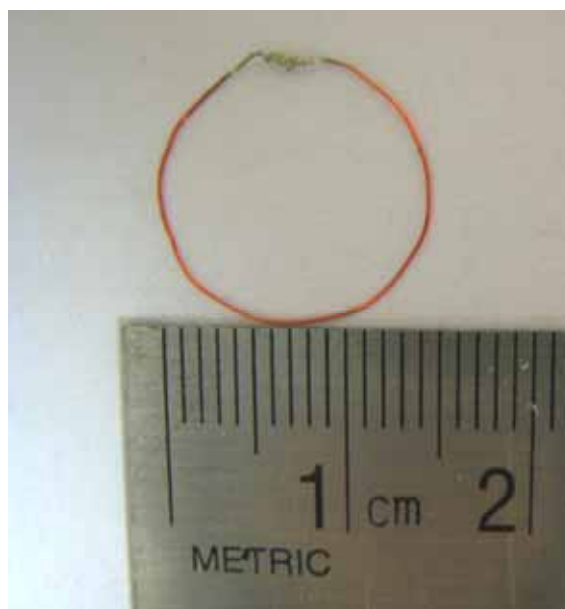


**Fig. 42. Sensor #1.**

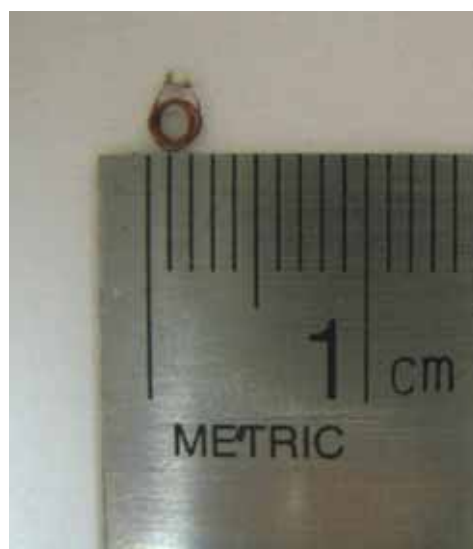


**Fig. 43. Sensor #2.**



**Fig. 44. Sensor #3.**

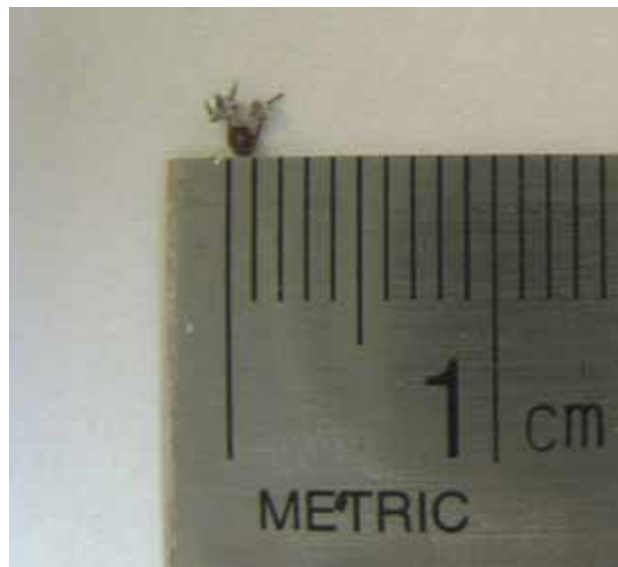


**Fig. 45. Sensor #4.**

To set up a measurement, the network analyzer is calibrated to the end of the co-axial cable, then the detector is connected by soldering. The network analyzer reads the return loss of the detector.

Firstly, Sensor #2, #3 and #4 were measured by detector #1 with a 1mm distance (Fig. 46). Sensors have different resonant frequencies due to different sizes of coils giving different

inductances. The bigger the coil is, the bigger the inductance, the lower the resonant frequency. Larger coil tends to have larger coupling effects because more magnetic flux goes through the inner area of the sensor coil, and a deeper dip return loss is observed as well.

Using detector #1 and sensor #3 as a reference, measurements were conducted with different measurement distances (Fig. 47). As the distance becomes larger, the resonant frequency of the detector sensing goes larger too, and also the return loss dip becomes shallower. The effect happens due to the variable coupling effects. As the distance becomes larger, the inductance the detector can detect becomes smaller, and the resonant frequency it is detecting becomes larger as well. Also when the distance goes up, the coupling effect goes down, which results in a shallower dip for the return loss.

In order to compare the detectors, sensor #3 has been used as a reference and measurements were conducted using different detectors with a 1mm distance (Fig. 48). Detector #1 has the best results because the high permeability core improves the magnetic flux density. Detector #2 has a shallower return loss dip because the magnetic flux density becomes less than the Detector #1 case. Detector #3 cannot detect sensor #3 anymore since at the center of the detector the magnetic flux has the lowest density. For a 2 turns coil, most of the magnetic field is concentrated around the wire instead of the center. Due to this measurement, detector #1 is the best choice to measure small sensors such as sensor #3.

However, detector #3 has its own advantage to use in the present project. It can detect sensor #1 very well due to sensor #1 having a larger diameter and a single coil has really low mutual coupling effect for the coil itself (Fig. 49). So sensor #1 can be used as a secondary resonator, and when sensor #1 and #3 both are put in a concentric circle, the resonant

frequency changes because sensor #1 and #3 are trying to couple with each other too. In this sense, detector #3 can measure sensor #3 indirectly.

From the above analysis, a coil with a diameter 1.6mm is an optimum size for this IOP sensor. Detector #1 is the optimum one to sense the IOP sensor directly. However, by using a combination of both sensor #1 and #3, a new measurement prototype is introduced and the benefits becomes obvious in the following chapter.

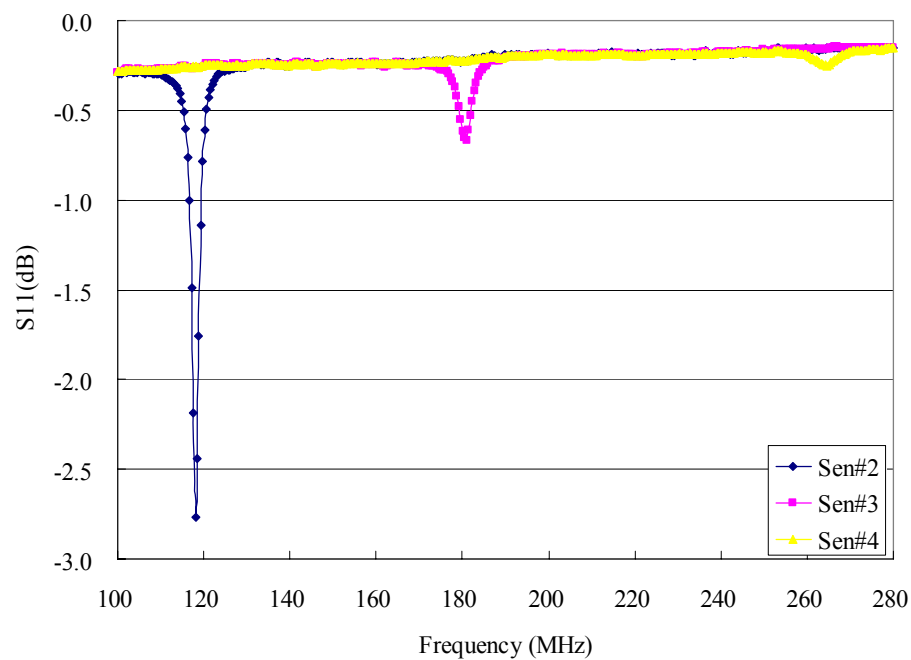


**Fig. 46. Measurement for different sensors using detector #1, measurement distance is 1mm.**

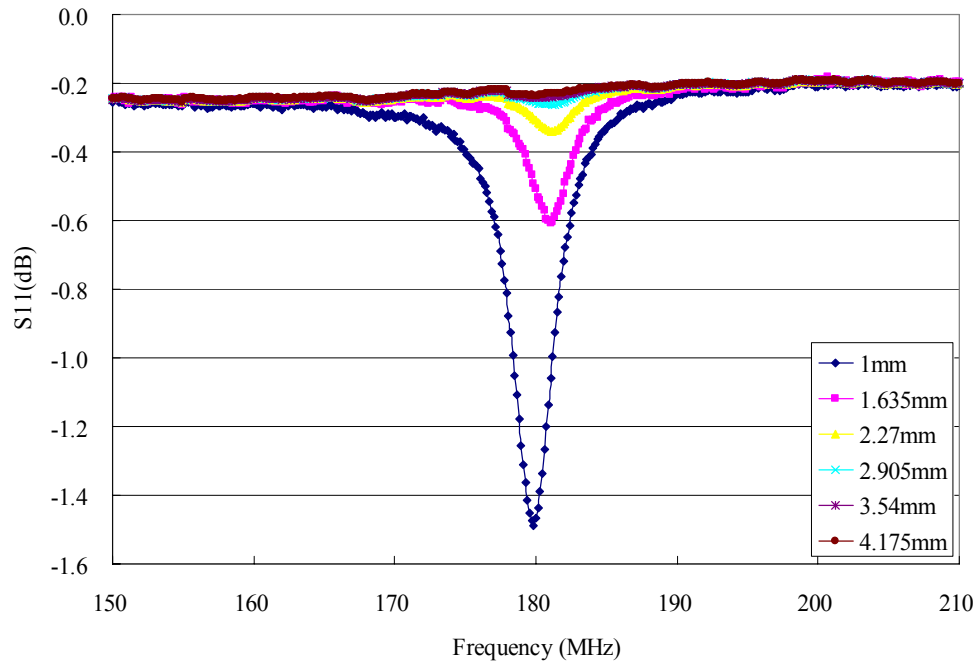


**Fig. 47. Measurement for detector #1 and sensor #3 with different measurement distances.**

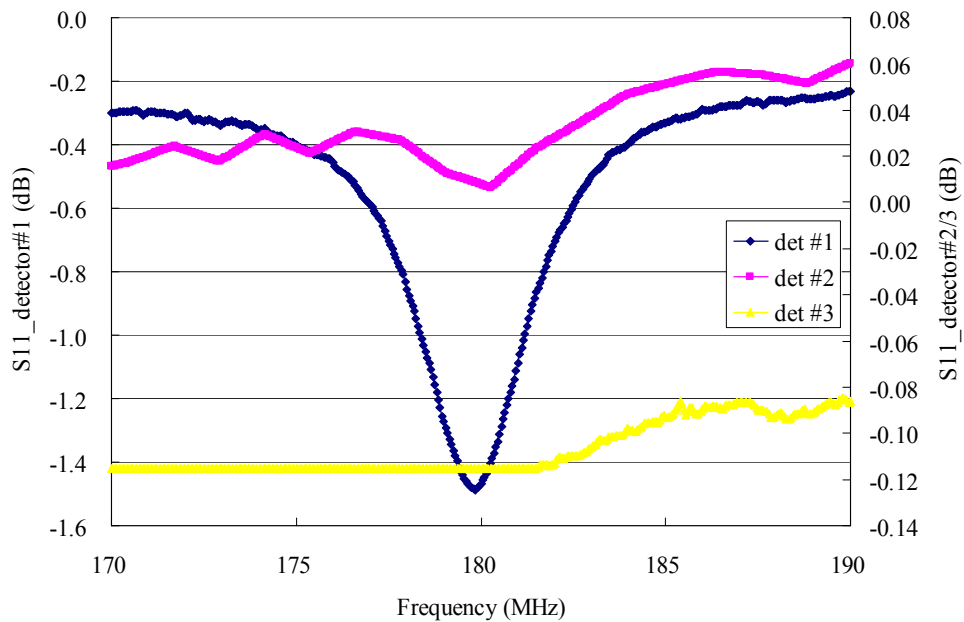


**Fig. 48. Measurement for sensor #3 with different detectors at 1mm measurement distance.**

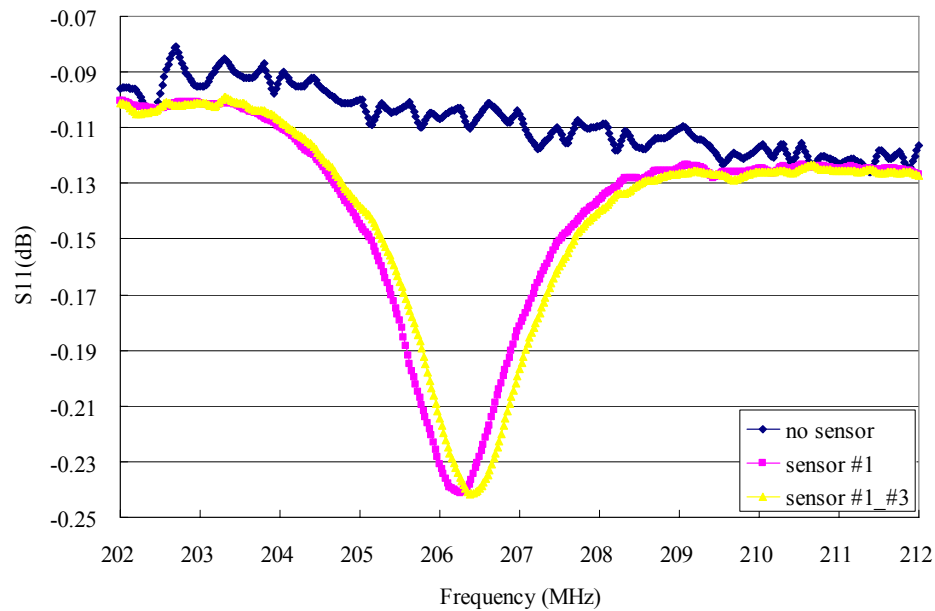


**Fig. 49. Measurement for detector #3 and sensor #1 and #3 at the same height.**

## 5.2 Measurement Setup

In the current project, high conductivity silver epoxy ( $<0.001\text{ohm-cm}$ ) has been used to attach inductor element to achieve high Q-factor parallel LC resonators on the landing pads (Fig. 50). A 6 turn AWG 38 enamel coil is attached with a 32 membrane array. The sensor has been tested in a variable pressure environment inside a pressure chamber (Fig. 51 and 52), which allows the air to be pressurized to larger than 100mmHg. The pressure gauge is used to monitor the pressure inside the chamber, and the network analyzer is used to read the input impedance of a detecting device. Hermetically sealed SMA connectors and a sealing O-ring were used.

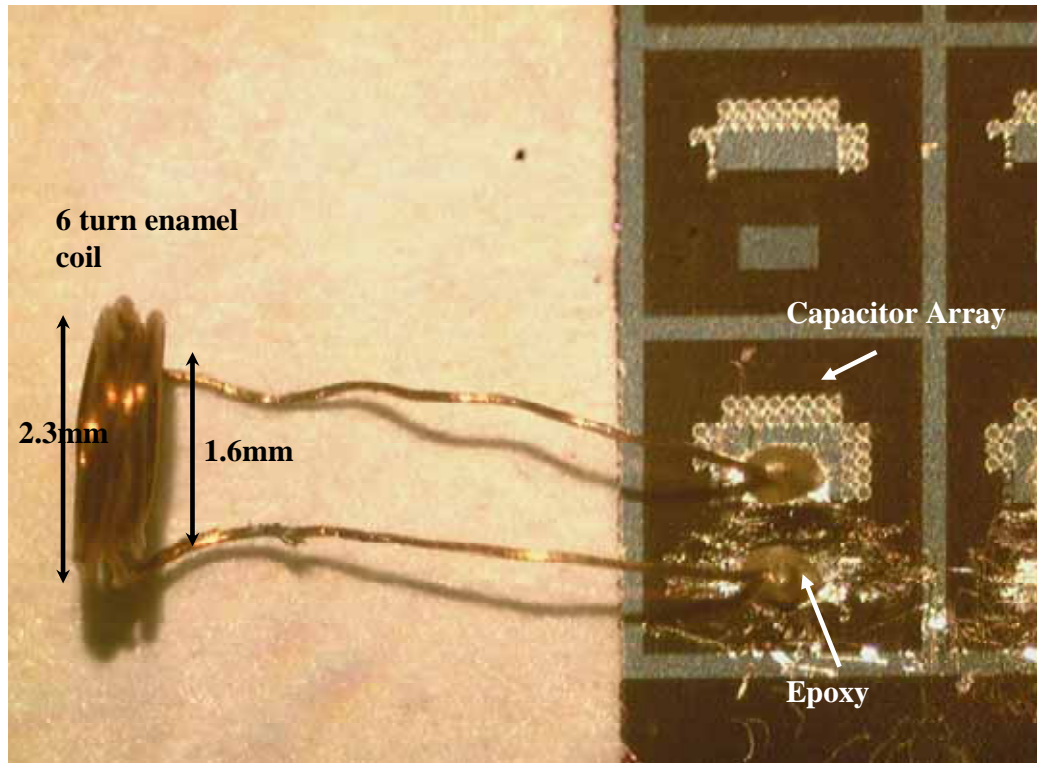


**Fig. 50.** A capacitor array integrated with a 6 turn enamel coil.

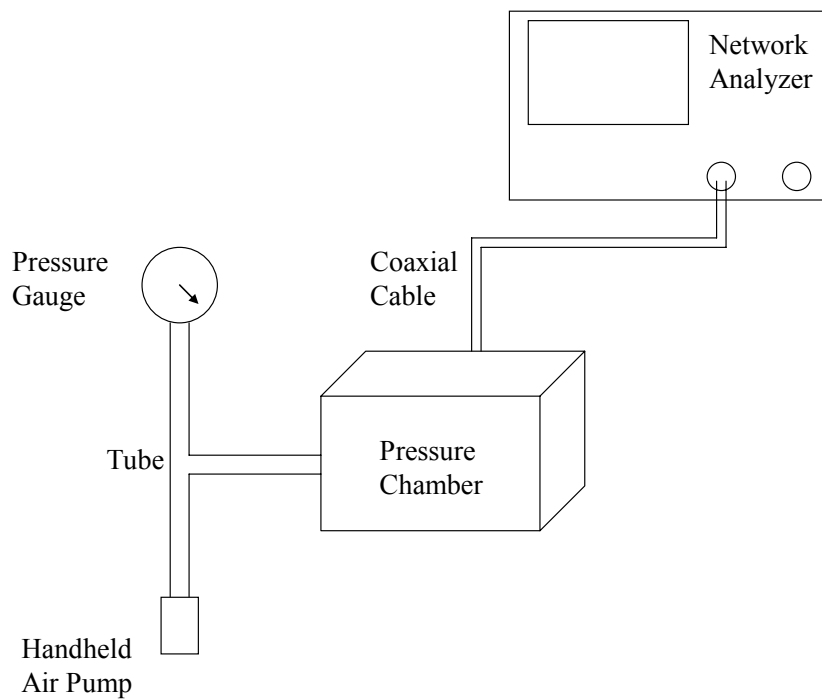


**Fig. 51.** Diagram of the variable pressure system for IOP sensor measurement.

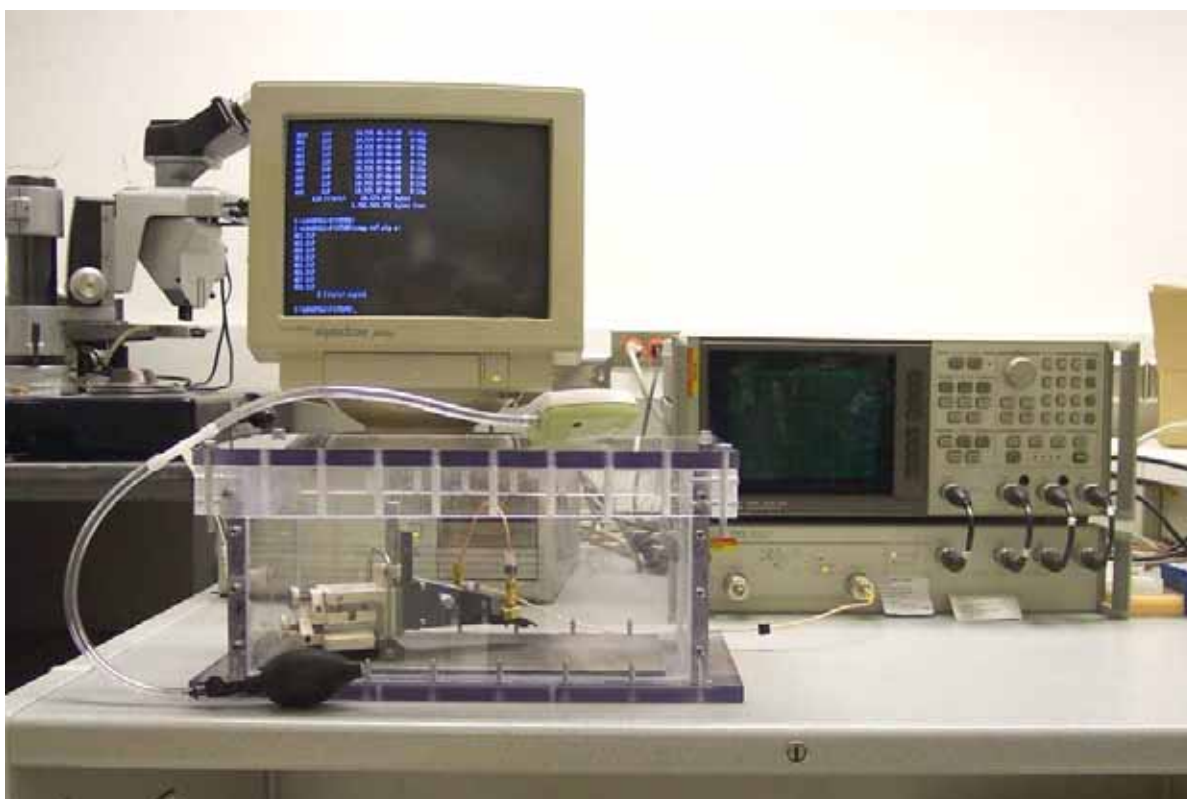


**Fig. 52. The variable pressure system setup.**

### 5.3 Probe Measurement

The purpose of probe testing is to examine the membrane's function, and direct probing can limit any noise inference. A Cascade probe ACP40-m-GSG-100 (Fig. 53) has been used for probe test. A 2 by 2 capacitor array (Fig. 54) shows a capacitance around 2.121pF with a sensitivity of  $2.616 \times 10^{-5}$  pF/mmHg for 4 membranes, although the MOM algorithm shows a capacitance around 0.321pF with a sensitivity of  $1.7 \times 10^{-5}$  pF/mmHg for 4 membranes (Fig. 55). The difference of the total capacitance is induced by the parasitic capacitance of the probe pad and Al ring structures. The difference of the sensitivity is due to few membranes and small sensitivity of the membranes comparing to the total capacitance.

The network analyzer is calibrated from 300kHz to 3GHz, and set with averaging factor of 50 and 2% smoothing aperture.

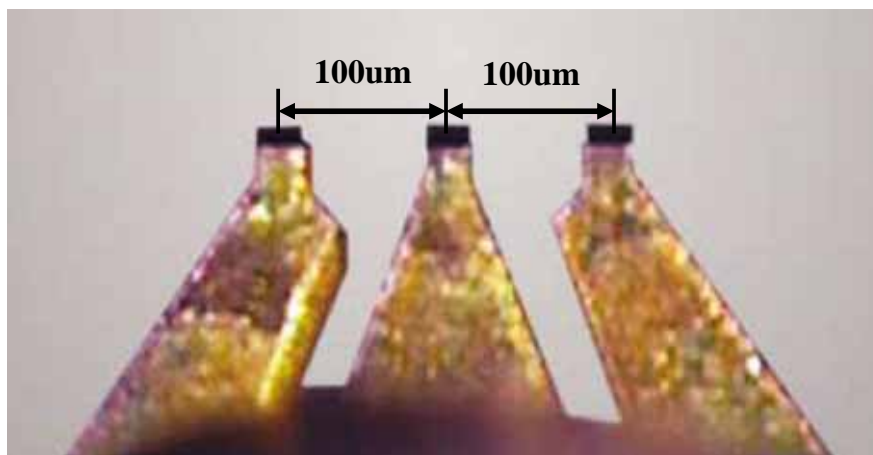


**Fig. 53.** Cascade ACP40-m-GSG-100 probe tip.

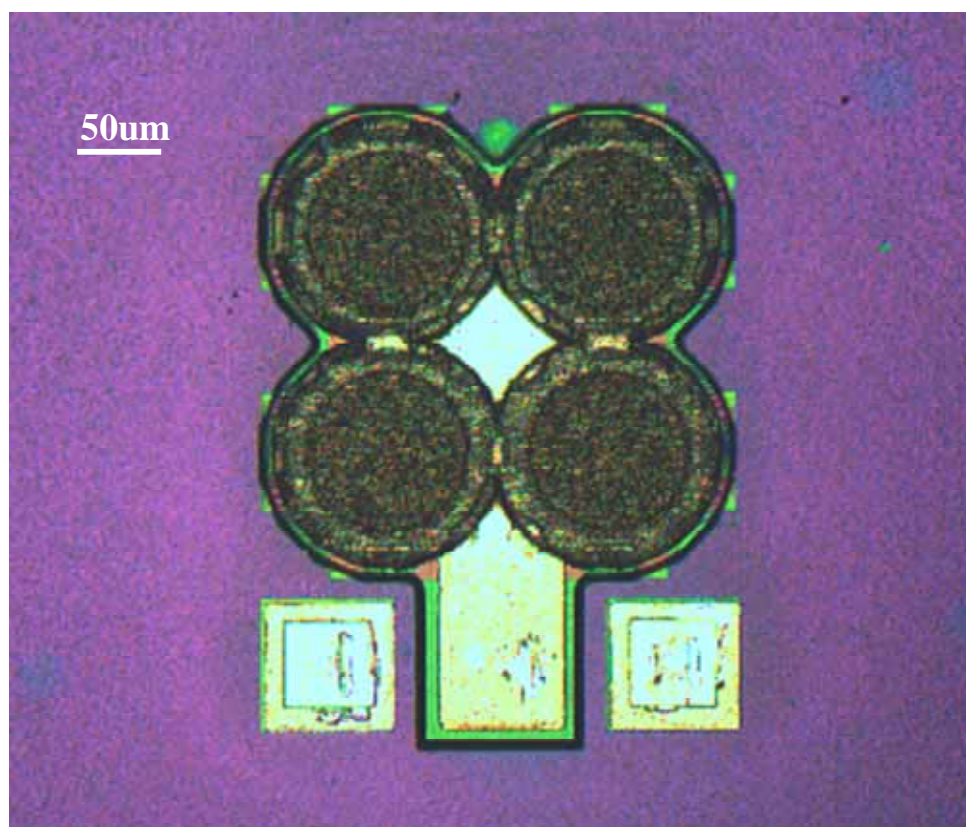


**Fig. 54.** A 2 by 2 membrane array.

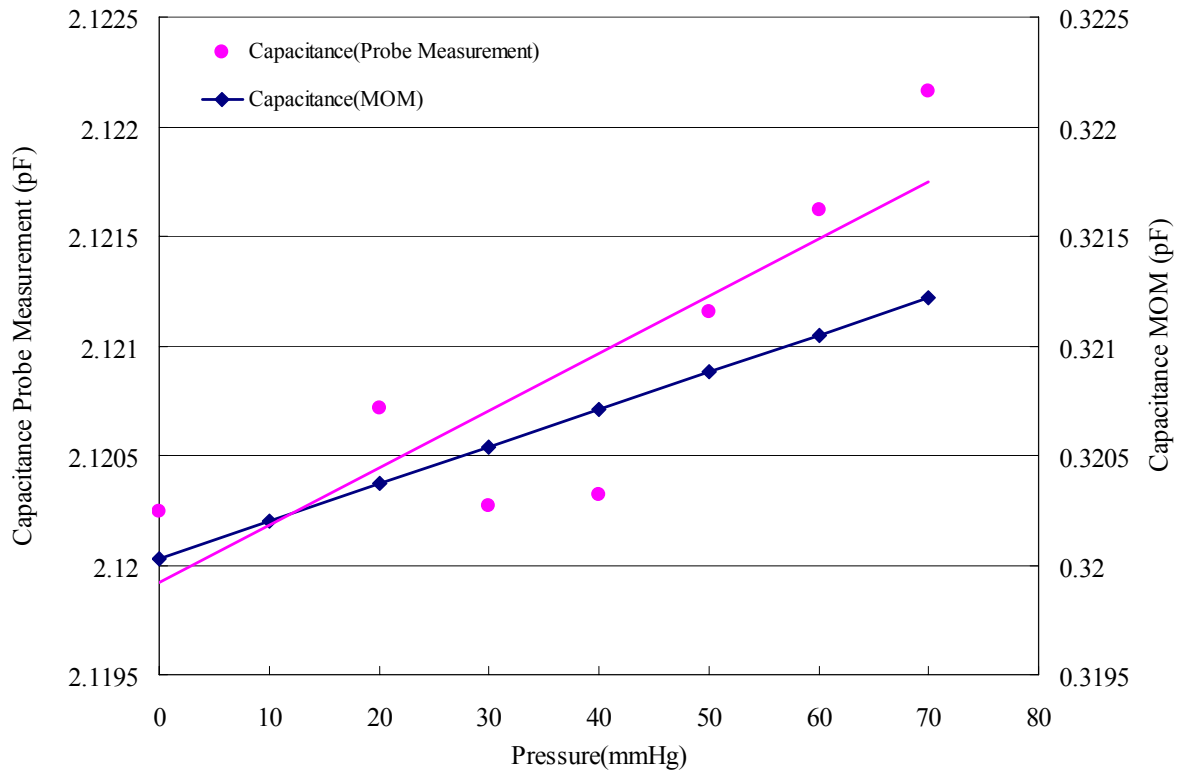


**Fig. 55. The probe measurement and MOM calculation (without parasitics) for a 2 by 2 membrane array.**

In order to measure a larger sensitivity of an array, another probe measurement was conducted for an array of 32 membranes (Fig. 50) with a 0403 1.9nH high-Q inductor (Coilcraft  $Q_{\min}=40$ ). The resonant frequency is around 26MHz and the sensitivity is about 17.2kHz/mmHg in a 50Ohm system (Fig. 56). Another probe measurement was conducted for an array of 11 membranes (7 malfunctioned) (Fig. 57) without any inductor. The structure itself resonates around 128MHz with a sensitivity of 125.56kHz/mmHg (Fig. 58).

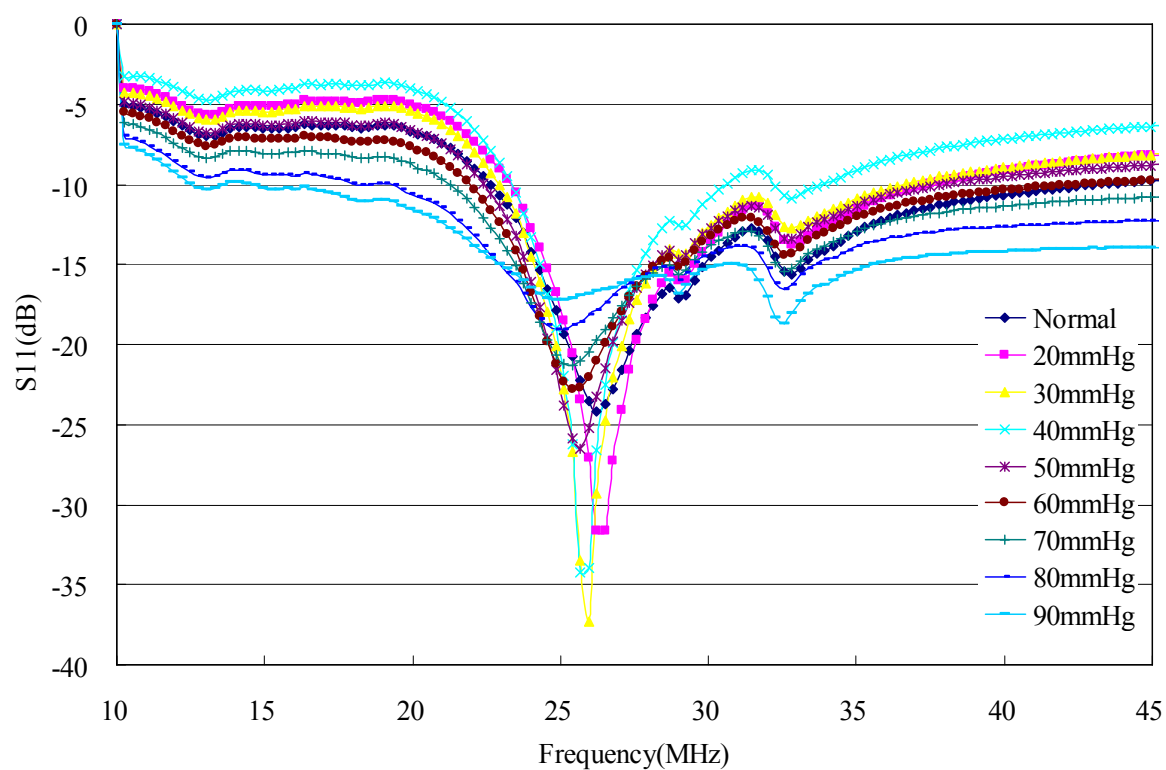


**Fig. 56.** Probe measurement of an array of 32 membranes with a 0403 1.9nH high-Q inductor (Coilcraft  $Q_{min}=40$ ).

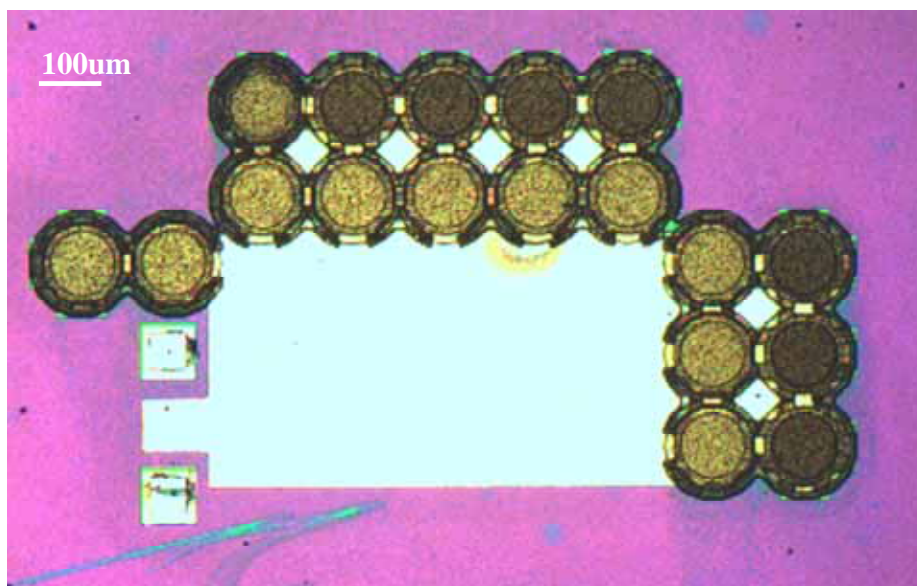


**Fig. 57.** An array of 11 membranes (7 malfunctioned).

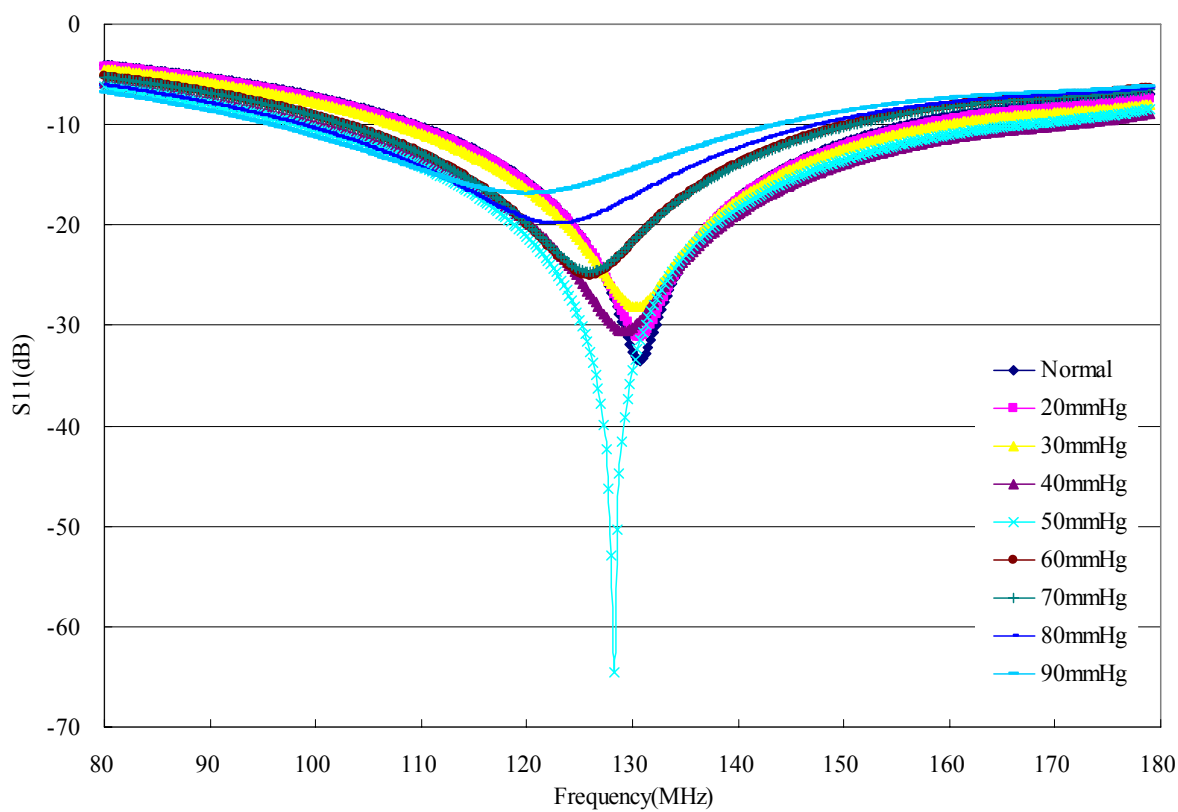


**Fig. 58. Probe measurement of an array of 11 membranes (7 malfunctioned).**

#### 5.4 Remote Measurement

The probe measurement confirms the change of membrane capacitance due to different pressure environments, The remote (*in vitro*) measurements have been performed on one of the IOP sensors. As in Fig. 50, a 6 turn AWG38 enamel coil was attached with the 32 membrane structure by high conductivity epoxy, the coil has an inner diameter of 1.6mm and an outer diameter of about 2.3mm. The detector being used is 5 turn AWG32 enamel coil with high permeability half cylinder core, which is detector #1 (Fig. 39). The network analyzer is calibrated from 300kHz to 1GHz and interpolated around the resonant frequency with 2MHz span for each measurement, and set with a averaging factor of 50 and 7% smoothing aperture.

The sensor was tested with the sensor coil being vertical to the wafer surface to make sure the magnetic field can most effectively excite the sensor (Fig. 59). The measurement results under different distances between the detector and the sensor are summarized in Table 7, the sensing distance can be achieved up to 4.04mm. When the pressure changes, the resonant frequency's change directly appears as the dip of return loss moving along to different frequencies (Fig. 60). As the sensing distance becomes larger and larger, the dip of the return loss for the detector coil becomes shallower and shallower, and it is hard to examine the dip change, so instead of examining the change of the dip of the return loss, the change of the phase has been recorded to measure the pressure change (Fig. 61-66).

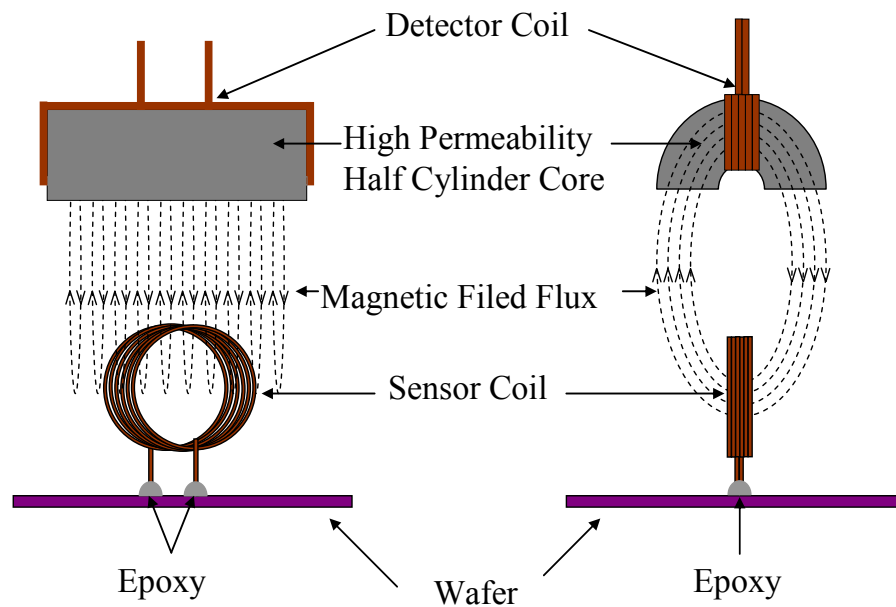


**Fig. 59.** IOP sensor is detected by a coil detector with high permeability half cylinder core.

Sensing Distance (mm)	Resonant frequency(MHz)	Detector Return Loss (dB)	Sensitivity (kHz/mmHg)
~0	~198.2	~-0.568	57.887
1	~198.7	~-0.5215	30.459
1.5	~200.7	~-0.517	16.859
2.77	~201	~-0.477	13.05
3.405	~201.1	~-0.4735	9.263
4.04	N/A	~-0.471	3.775

**Table 7.** Measurements of an IOP sensor with 32 membranes and 6 turn AWG38 enamel coil, the detector is a coil detector with high permeability half cylinder core.

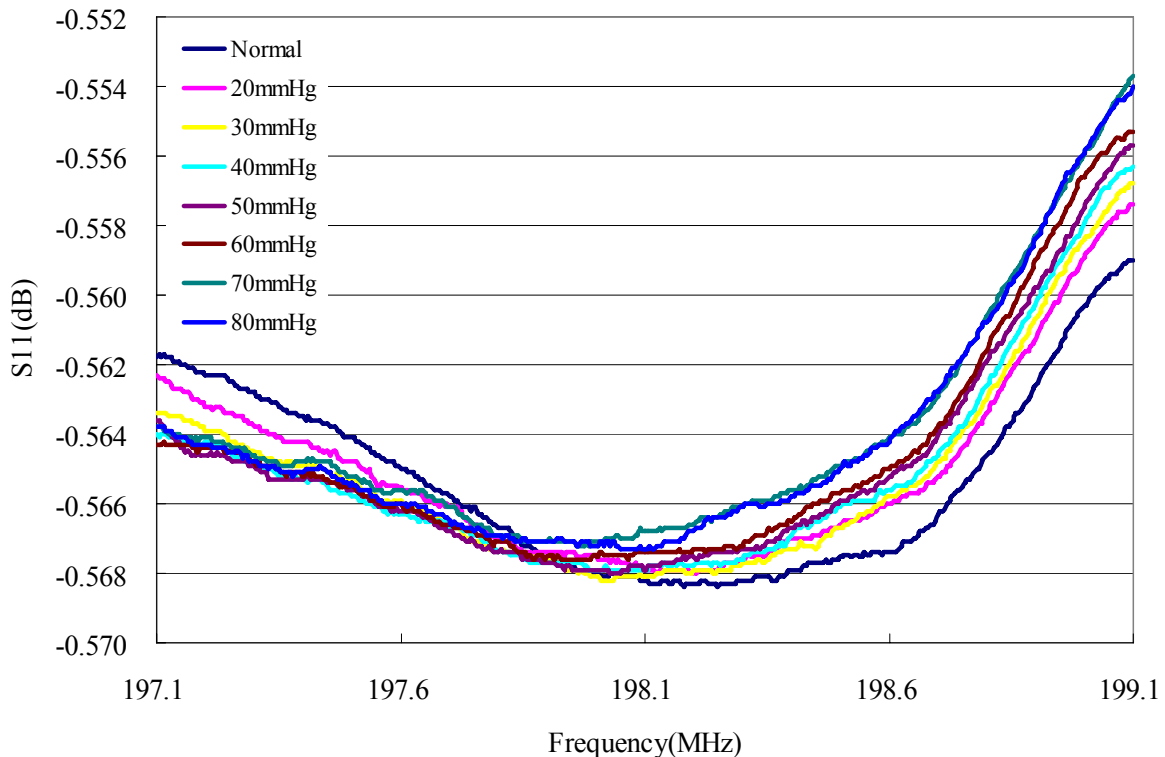


**Fig. 60.** The measurement return loss of a coil detector detecting an IOP sensor with the sensing distance is almost 0. Detector – 5 turn enamel coil with high permeability half cylinder core, IOP sensor – 32 membranes array and 6 turn AWG38 enamel coil.

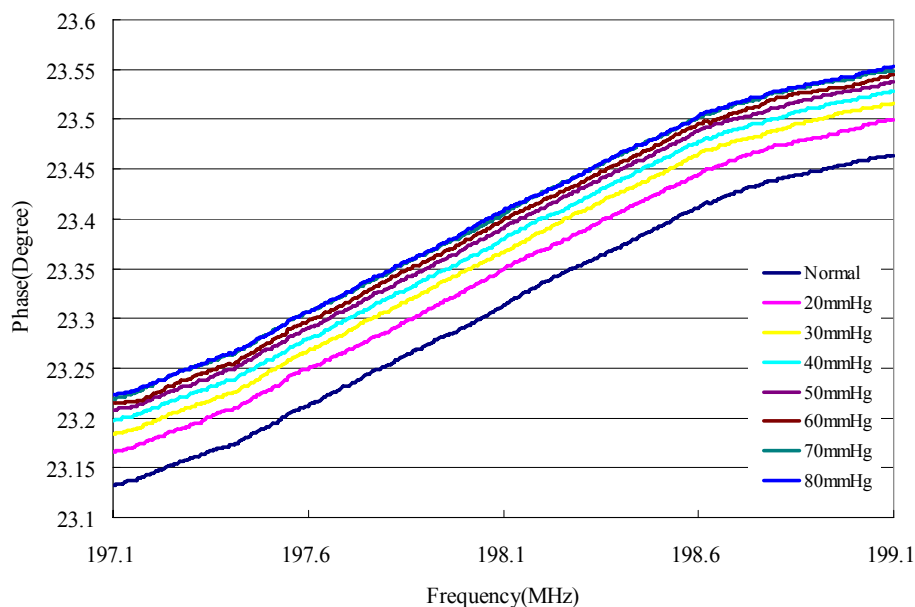


**Fig. 61.** The measurement phase of a coil detector detecting an IOP sensor with the sensing distance is almost 0. Detector – 5 turn enamel coil with high permeability half cylinder core, IOP sensor – 32 membranes array and 6 turn AWG38 enamel coil.

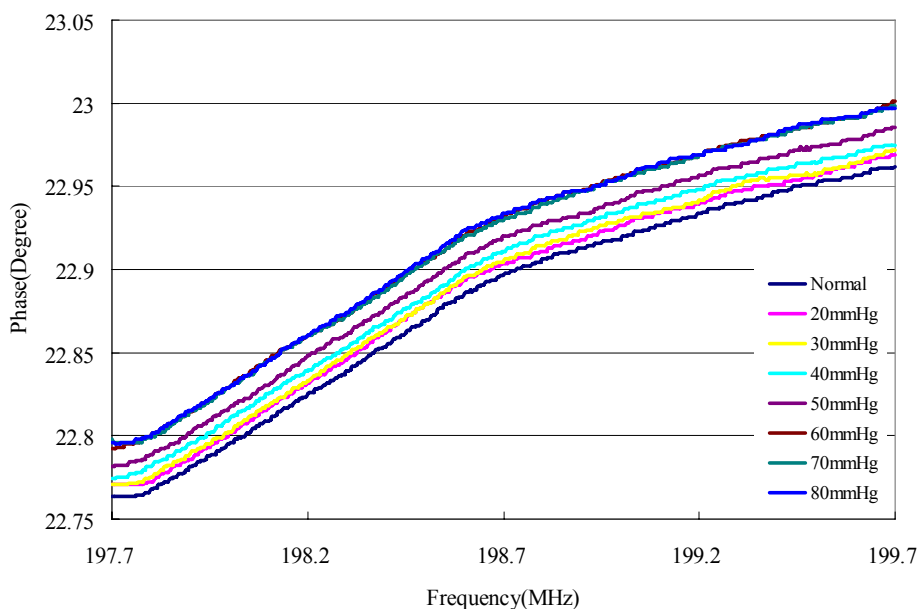


**Fig. 62.** The measurement phase of a coil detector detecting an IOP sensor with the sensing distance is 1mm. Detector – 5 turn enamel coil with high permeability half cylinder core, IOP sensor – 32 membranes array and 6 turn AWG38 enamel coil.

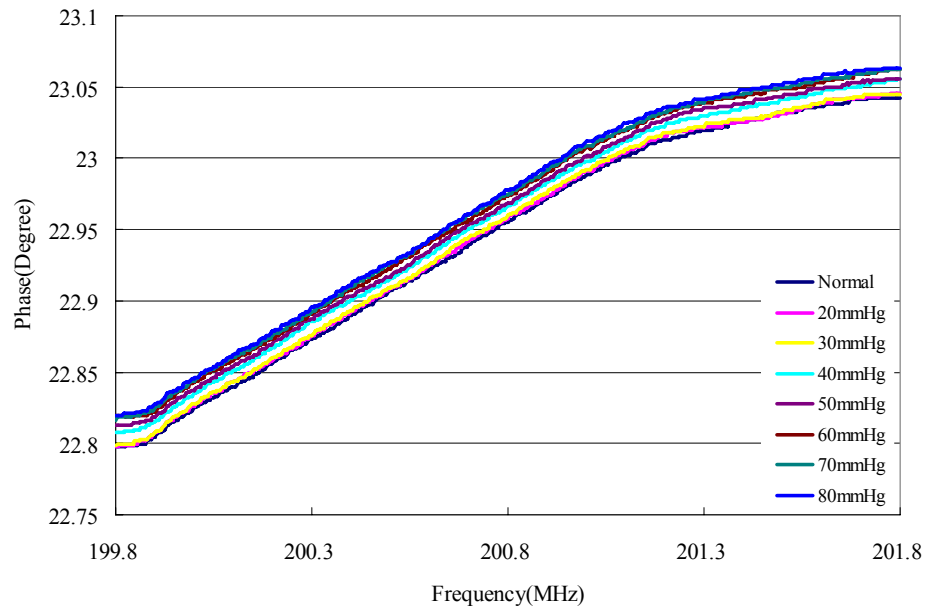


**Fig. 63.** The measurement phase of a coil detector detecting an IOP sensor with the sensing distance is 1.5mm. Detector – 5 turn enamel coil with high permeability half cylinder core, IOP sensor – 32 membranes array and 6 turn AWG38 enamel coil.

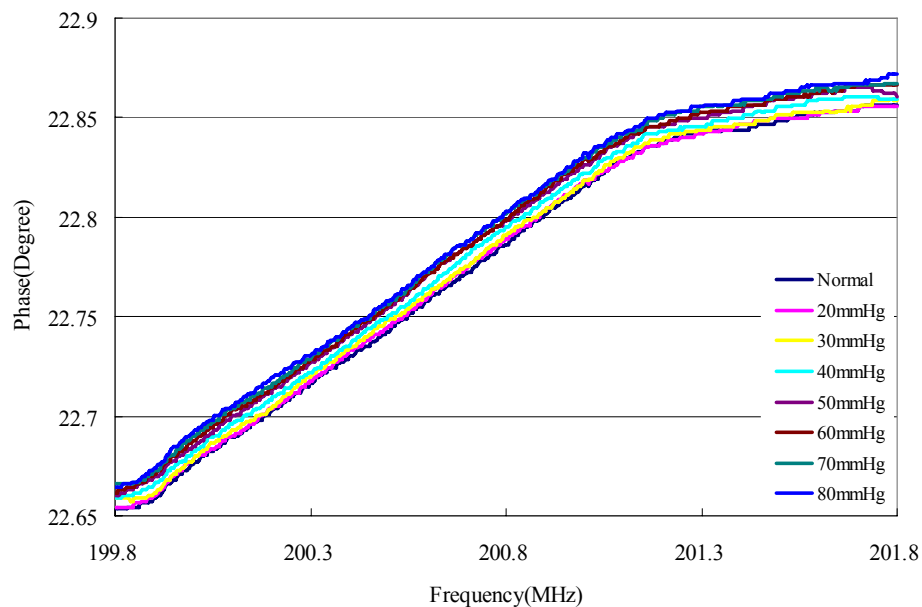


**Fig. 64.** The measurement phase of a coil detector detecting an IOP sensor with the sensing distance is 2.77mm. Detector – 5 turn enamel coil with high permeability half cylinder core, IOP sensor – 32 membranes array and 6 turn AWG38 enamel coil.

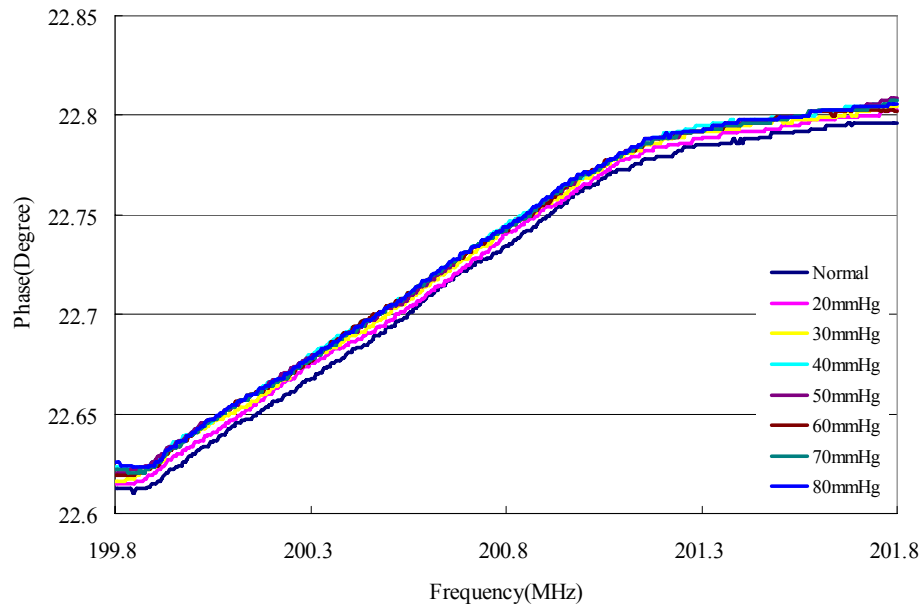


**Fig. 65.** The measurement phase of a coil detector detecting an IOP sensor with the sensing distance is 3.405mm. Detector – 5 turn enamel coil with high permeability half cylinder core, IOP sensor – 32 membranes array and 6 turn AWG38 enamel coil.

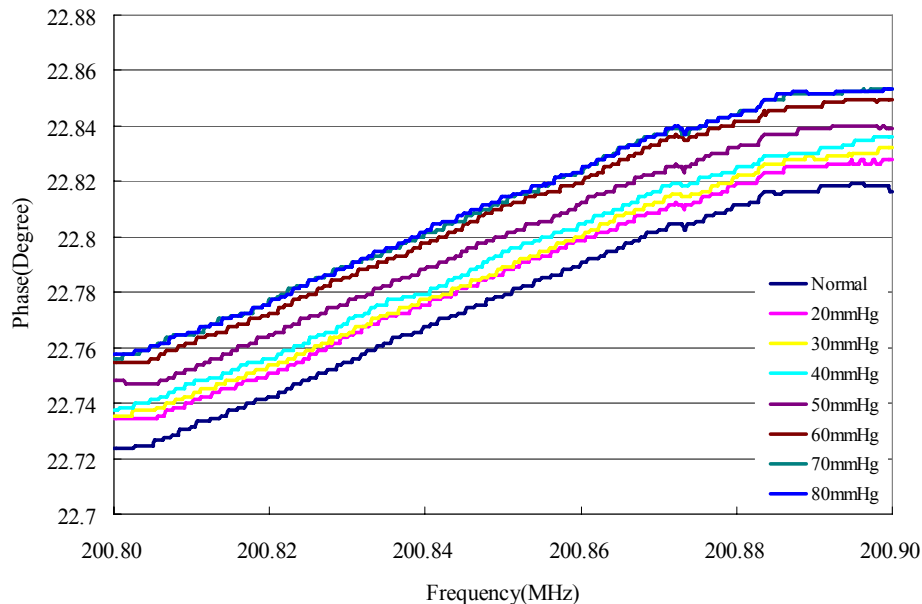


**Fig. 66.** The measurement phase of a coil detector detecting an IOP sensor with the sensing distance is 4.04mm. Detector – 5 turn enamel coil with high permeability half cylinder core, IOP sensor – 32 membranes array and 6 turn AWG38 enamel coil.

The maximum sensing distance for the above telemetry configuration is about 4mm. Further than 4mm, the results become noisy and unstable. However, 4mm is larger than most of the published results for such a small sensor.

In order to improve the sensing distance, a unique telemetry configuration is introduced in this invention as Fig. 67. In this configuration, a secondary resonator is induced between the IOP sensor and main primary detector to help the detection. The IOP sensor resonates at different frequencies under different intraocular pressures, and couples with the secondary resonator. Due to this coupling, the resonant frequency of the secondary resonator changes accordingly. Then the primary detector mainly couples with the secondary resonator instead of the small IOP sensor since larger coils tend to have stronger coupling effects. The distance between the IOP sensor and the secondary resonator is about 1mm, and the distance between the primary detector and the secondary resonator can be improved to 1.5cm. Such a large sensing distance can allow the primary detector to be integrated into a pair of spectacles, and the secondary resonator can be integrated with contact lens (Fig. 68), the coil with high permeability core can also be used as primary detector. In this invention, a 2 turn AWG32 enamel coil ( $d=5\text{cm}$ ) is used as the primary detector (detector #3), and a single turn AWG32 enamel coil ( $d=1\text{cm}$ ) with a 0402 15pF capacitor (sensor #1) is used as the secondary resonator.

Two measurements with the sensing distance of 1cm and 1.5cm are conducted, the IOP sensor coil is close to the edge of the secondary resonator to improve the coupling, and is parallel with the secondary resonator as well as the primary detector (Fig. 69). The results with fitting curves show how the phase changes due to different pressure applied to the IOP sensor. When the sensing distance is 1cm, the sensor has a sensitivity of about 203Hz/mmHg,

when the sensing distance is 1.5cm, the sensor has a sensitivity of about 185Hz/mmHg (Fig. 70 and 71).

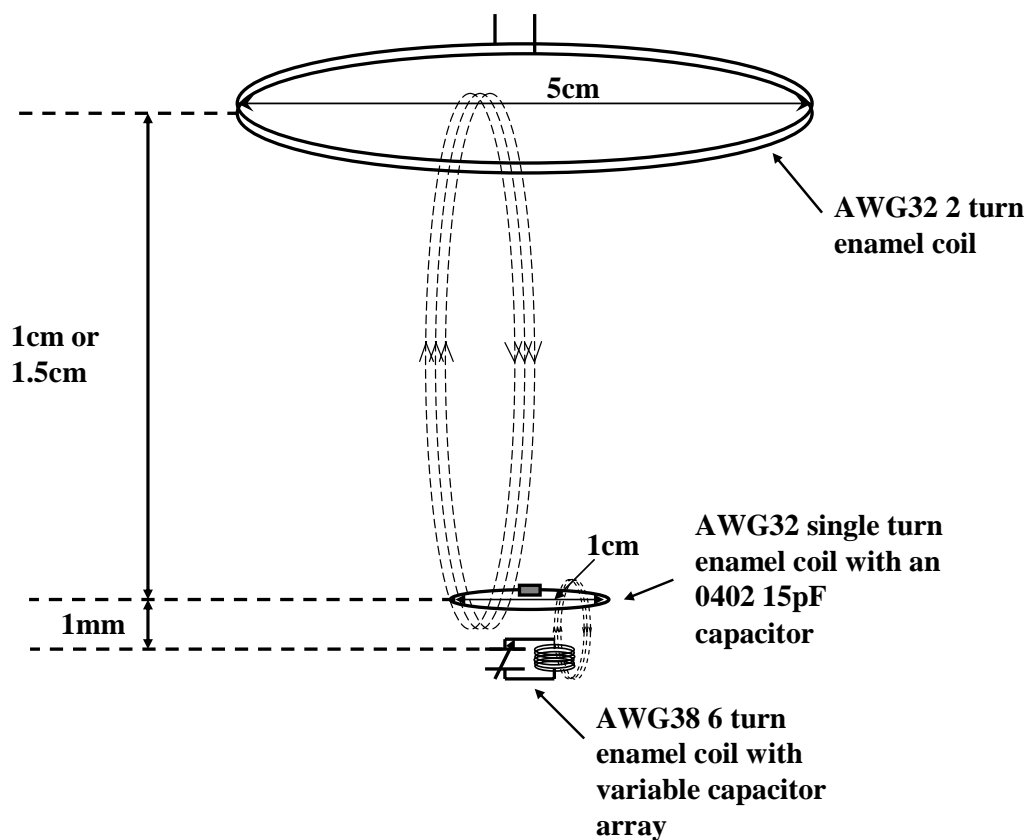
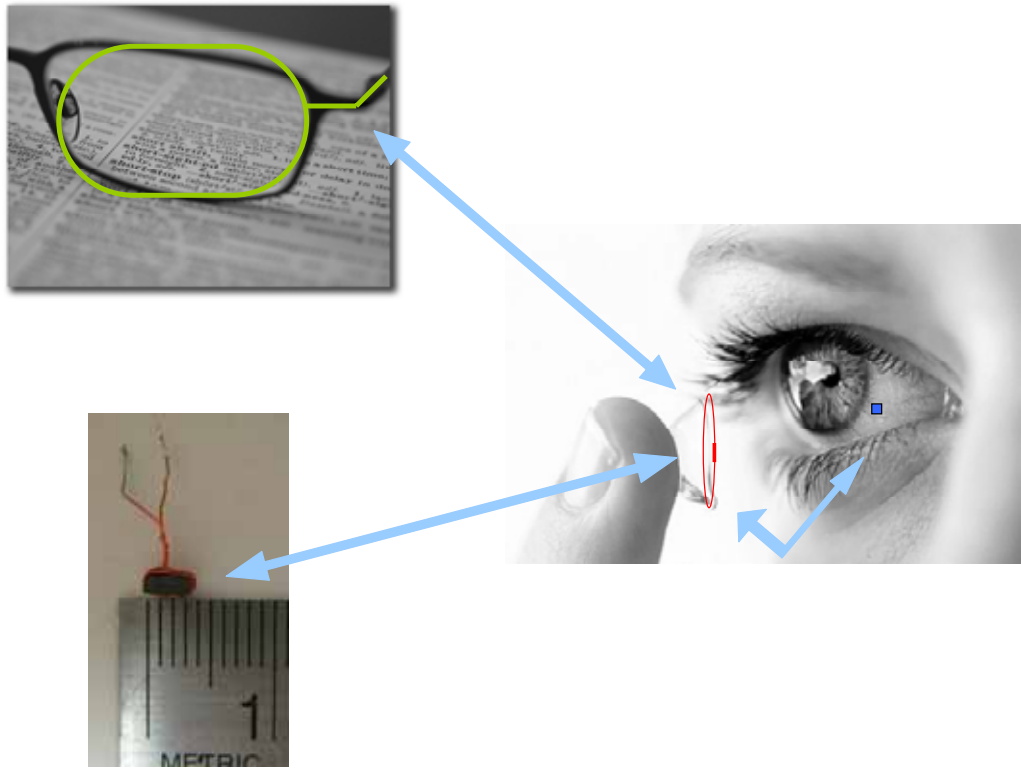


Fig. 67. The telemetry configuration using a secondary resonator.



**Fig. 68.** The telemetry configuration using a secondary resonator in realistic daily use\* .

---

\* Picture source: <http://www.dailymail.co.uk/health/article-1028876/Contact-lenses-boost-sight-sleep.html>

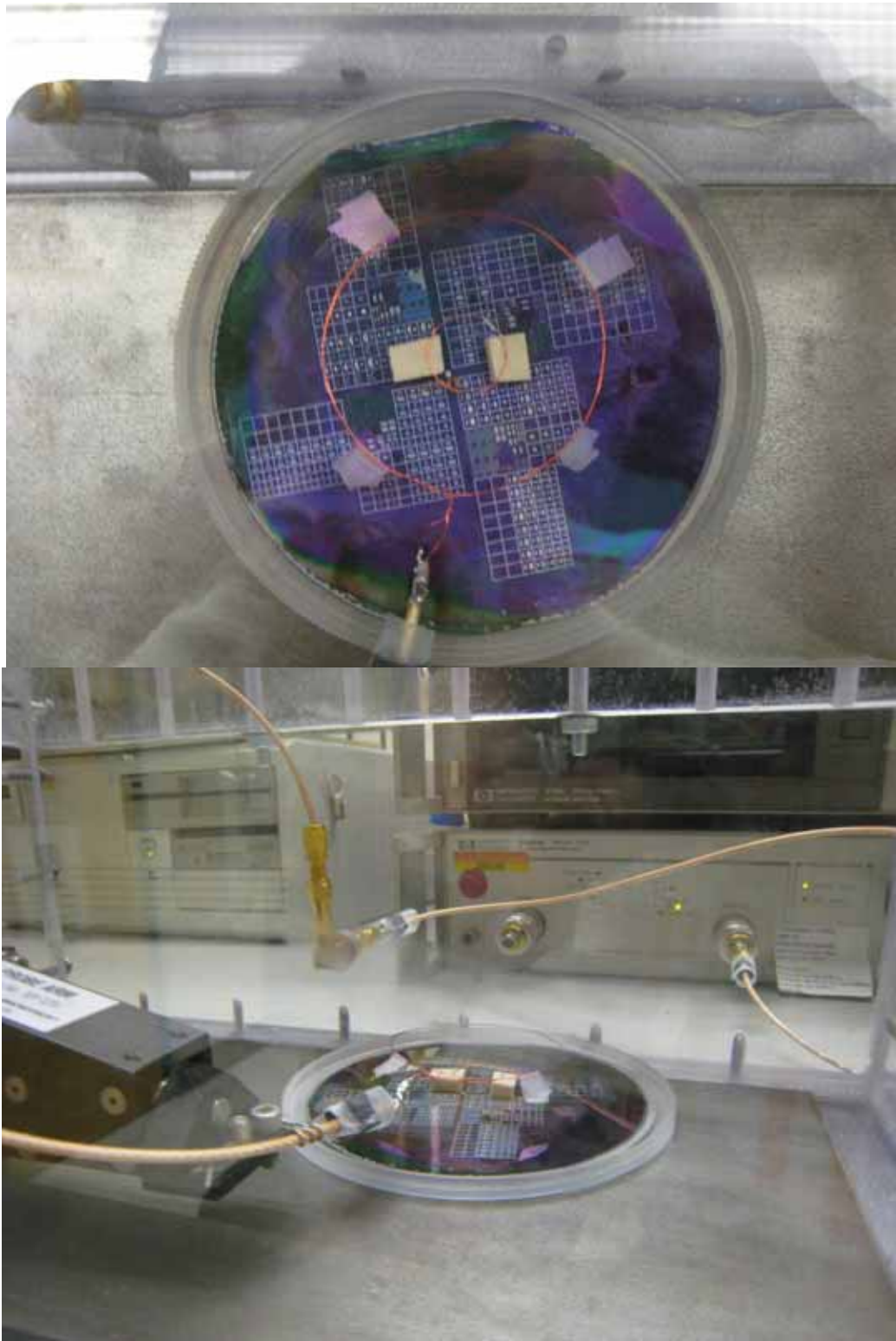


**Fig. 69. Measurement setup of the telemetry configuration using a secondary resonator.**

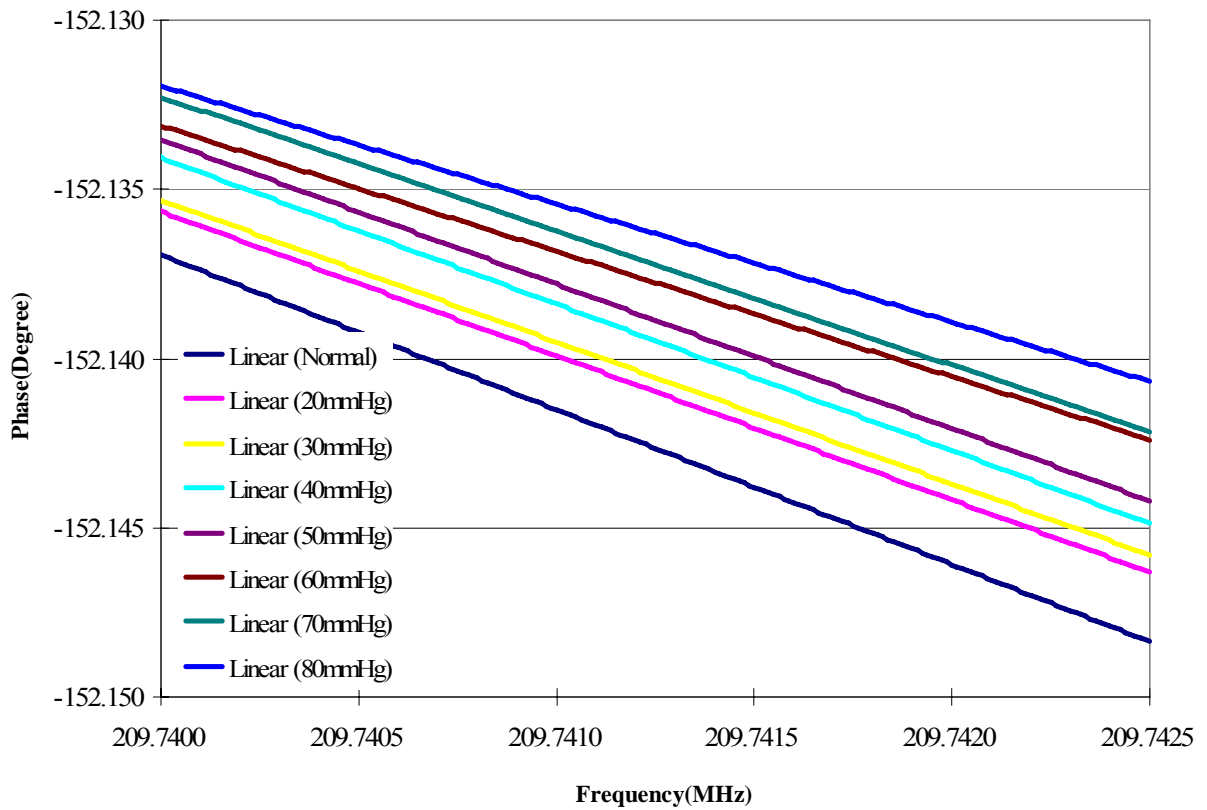


**Fig. 70.** The measurement phase (fitting) of a primary coil detector detecting an IOP sensor by using a secondary resonator with the sensing distance is 1cm. Detector – 2 turn enamel coil with a diameter of 5cm, secondary resonator – single turn enamel coil (d=1cm) with a 0402 15pF capacitor, IOP sensor – 32 membranes array and 6 turn AWG38 enamel coil.

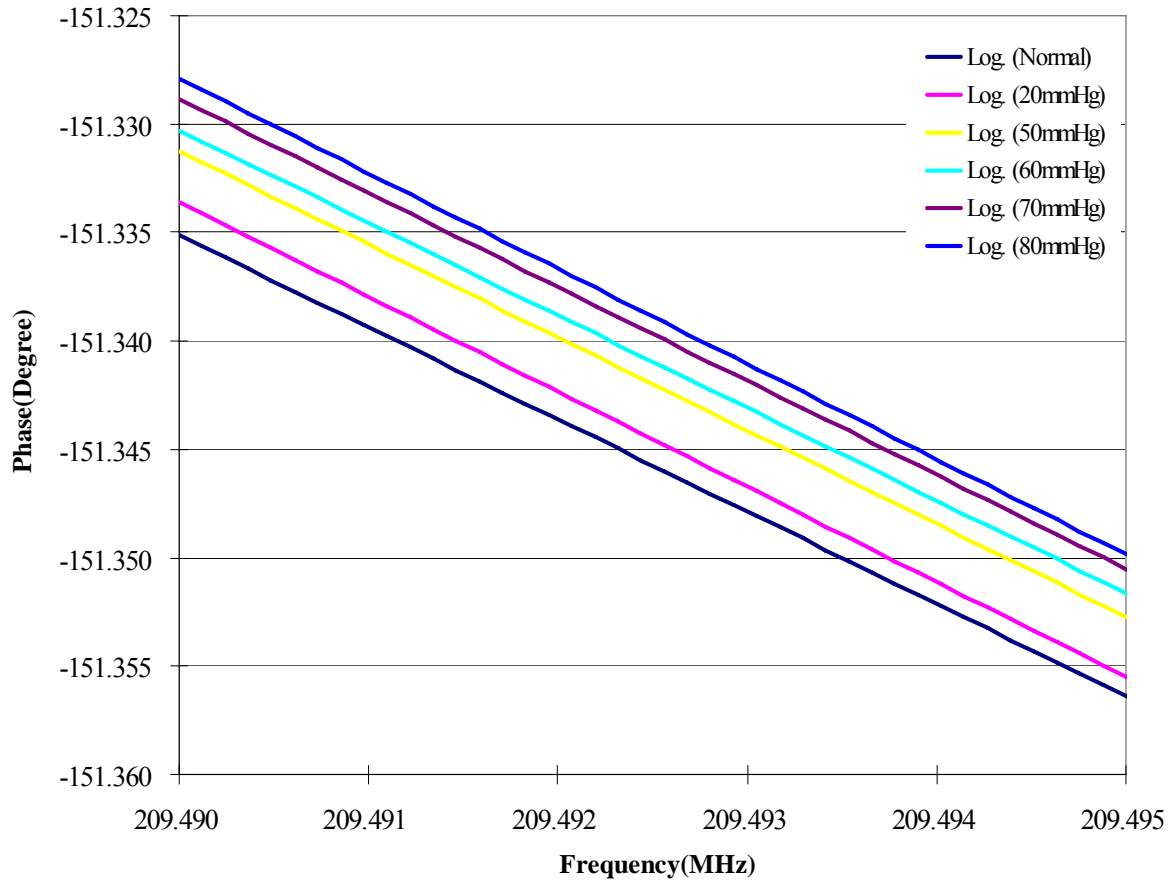


**Fig. 71.** The measurement phase (fitting) of a primary coil detector detecting an IOP sensor by using a secondary resonator with the sensing distance is 1.5cm. Detector – 2 turn enamel coil with a diameter of 5cm, secondary resonator – single turn enamel coil (d=1cm) with a 0402 15pF capacitor, IOP sensor – 32 membranes array and 6 turn AWG38 enamel coil.

## CHAPTER 6. FUTURE WORK AND CONCLUSION

### 6.1 Discussion

#### Biocompatible Coating

Most of the materials been used in this project are biocompatible materials, such as silicon, silicon nitride ( $\text{Si}_3\text{N}_4$ ), silicon dioxide ( $\text{SiO}_2$ ), and polysilicon. Aluminum is not a biocompatible material but it can be replaced or covered by another metal such as titanium. The epoxy and enamel coil need biocompatible material coatings. Silicone, PMMA or Acrylic can be used for this purpose.

#### Calibration

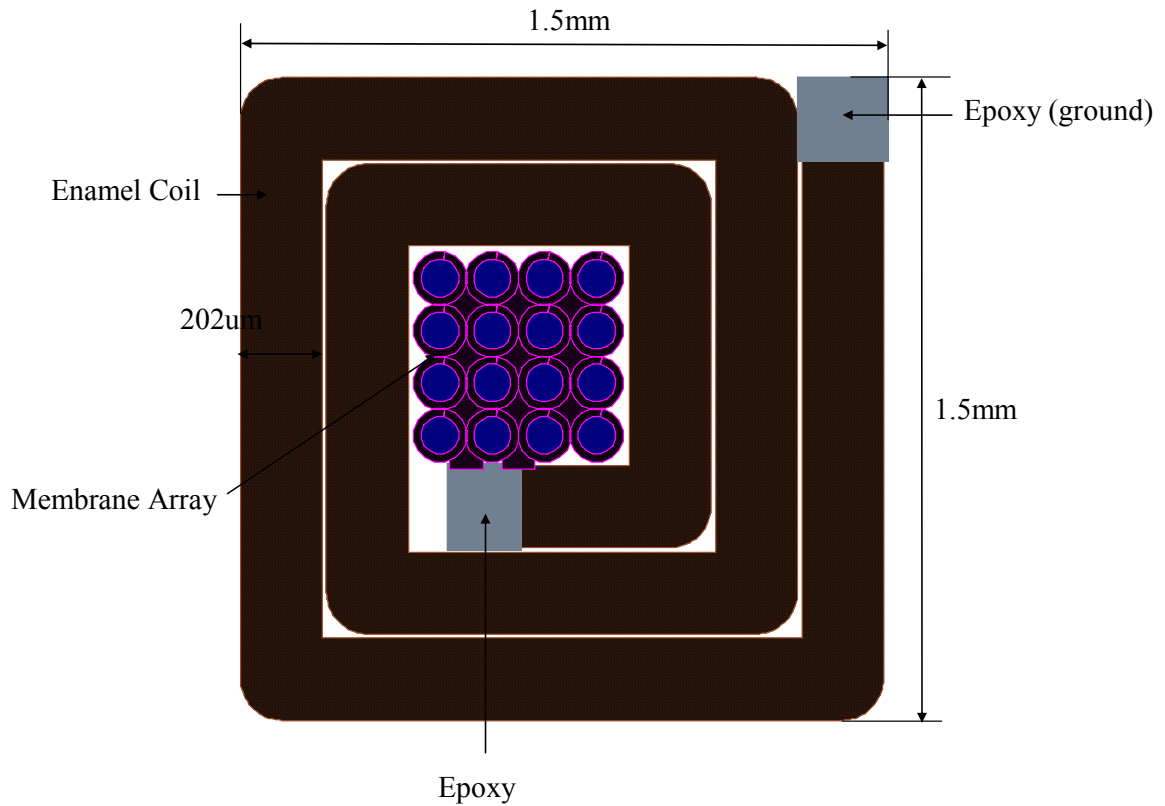
Before the sensor can be used to measure pressures, it needs to be calibrated in a variable pressure environment. Due to the fabrication variation, degradation from coating, and handling effect, each sensor can have a different resonant frequency and a different response. The calibration needs to be performed in a period of time until each measurement correlates.

#### Implantation

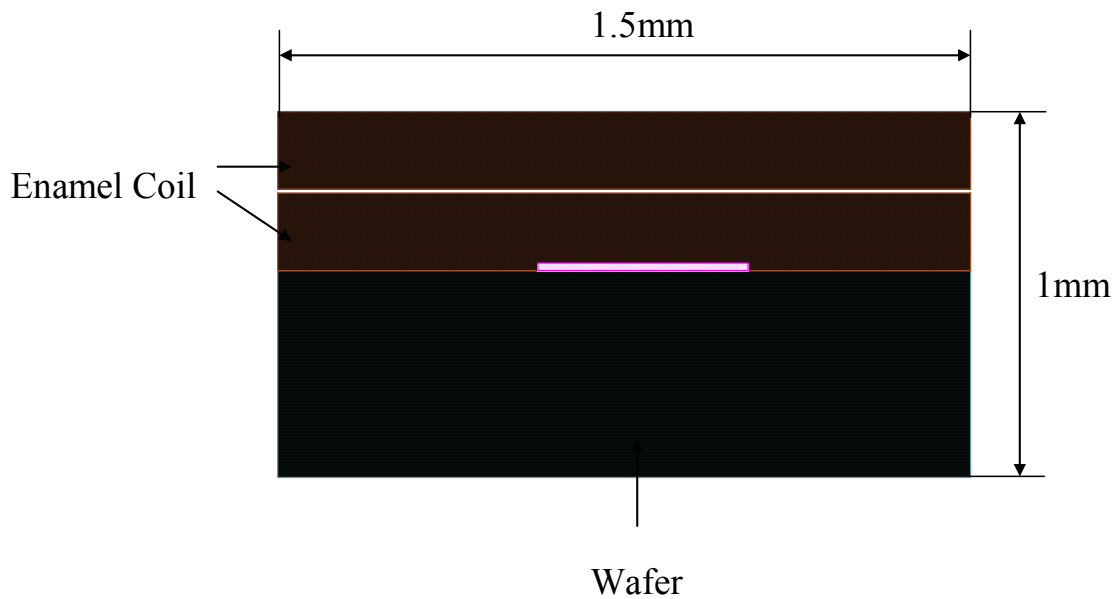
The IOP sensor can be implanted in several places inside or on the surface of the eye. It can be placed inside the anterior chamber, vitreous cavity, or posterior chamber. It can be placed on the eye surface during the tube-shunt surgery. If a noninvasive way preferred, the IOP sensor can be integrated into contact lens. In that case how the eye pressure can convert to the eye surface expansion needs to be considered.

## Size

The size of the IOP sensor in this invention can be minimized to  $1.5\text{mm} \times 1.5\text{mm} \times 1\text{mm}$  (Fig. 72) if the assembly can be well controlled. If one chooses to use fewer membranes and fewer turns of coil, the size can be shrunken even less. This implantable IOP sensor is a passive LC resonator device and does not require any external energy sources, so there is no concern to implant any power source such as batteries.



(a)



(b)

**Fig. 72.** A proposed IOP sensor structure, (a) top view, (b) side view.

## 6.2 Contributions

It is a primary contribution for this project that it provides a novel technique to use a secondary resonator to improve the IOP sensor sensing distance to 1.5cm. This distance is larger than the other published work with similar sizes.

This project provides a technique using surface micromachining technology to fabricate membrane structures, and an assembling method to integrate the membrane array with an enamel coil. It provides a high-Q low electrical loss solution for LC type of resonators.

This project provides a laboratory set-up for pressure sensor measurement, a pressure chamber can produce a pressure up to 100mmHg or even larger. The probe station and detector coils can also be used for other wireless sensor or IC sensor measurements.

This project provides a detailed process flow for IOP sensor fabrication. The HF vapor sacrificial etching and CPD release technique has been proved to be easy and effective. Careful attention has been paid to thick layer step coverage, cavity sealing and etching undercut compensation. All of these provide a good reference for other researchers who are working in the similar area.

It is also another contribution for the work that it synthesizes an 8-layer mask into a 2-layer mask, a new set of alignment markers have been designed and can reduce the budget of manufacturing cost.

Finally, this project provides an algorithm to model a circular membrane with different deformations due to different pressures. It induces a concept to use a small but finite skin depth in the membrane model, and avoids the singularity problem during the elliptic integration. It provides a fast and accurate way to calculate the capacitance for a circular membrane and derive the charge density.

### **6.3 Future Work**

There are several aspects of the present project can be improved. They are suggested as the future work for the IOP sensor design and measurement.

## **Fabrication Control**

The “seasoning” effect of the fabrication facility and process variation do produce differences between the final structure and the design specification, such as sacrificial layer (PSG) thickness and structure layer (Phos-poly) thickness. It will improve the performance of the IOP sensor if those effects can be well controlled during fabrication process. Multiple calibrations may be needed for the facilities.

## **Parasitic Model**

The MOM algorithm only calculates the capacitance for the membrane structure. However, there are parasitics for the additional structures such as the aluminum contact ring and membrane stands. The capacitance calculation can be improved if those parasitic models can be included or reduced. For the present project, due to the fabrication variation, it is difficult to properly model those parasitic structures.

## **Improved Measurement**

During the *in vitro* measurement, the sensor was tested in a whole wafer environment. There is additional electrical loss in the wafer substrate, especially for the high conductivity silicon case. The sensing distance and sensitivity can be improved if the IOP device can be sliced into dies. Due to facility limitation, this was not conducted in the present project. A wafer saw will give too much vibration and tends to break the membrane device, a suggestion using DRIE to etch the wafer is proposed as follows: the wafer is first softly bonded to another wafer carrier, and covered by Kapton tape to define the die edges, the a layer of  $Al_2O_3$  can be deposited by the ALD system to protect the membranes. Then the Kapton tape can be stripped

and the wafer can be etched by DRIE to cut the die edge. Then the  $Al_2O_3$  layer can be removed in a Trion I system and the devices got diced.

### **Detector Circuitry**

During the measurement, the network analyzer was calibrated by an averaging factor of 50 and 2% smoothing aperture. During the detector circuitry design, the averaging effect and smoothing effect need to be implemented. A phase-locked loop should be considered to track the phase response from the detector.

### **Body Environment**

In order to simulate the human body environment, the LC resonator kit (sensor #1) was immersed into a small portion of water for a remote measurement (Fig. 73). However the detector does not pick up any resonance or response from this set-up, further research should be conducted.

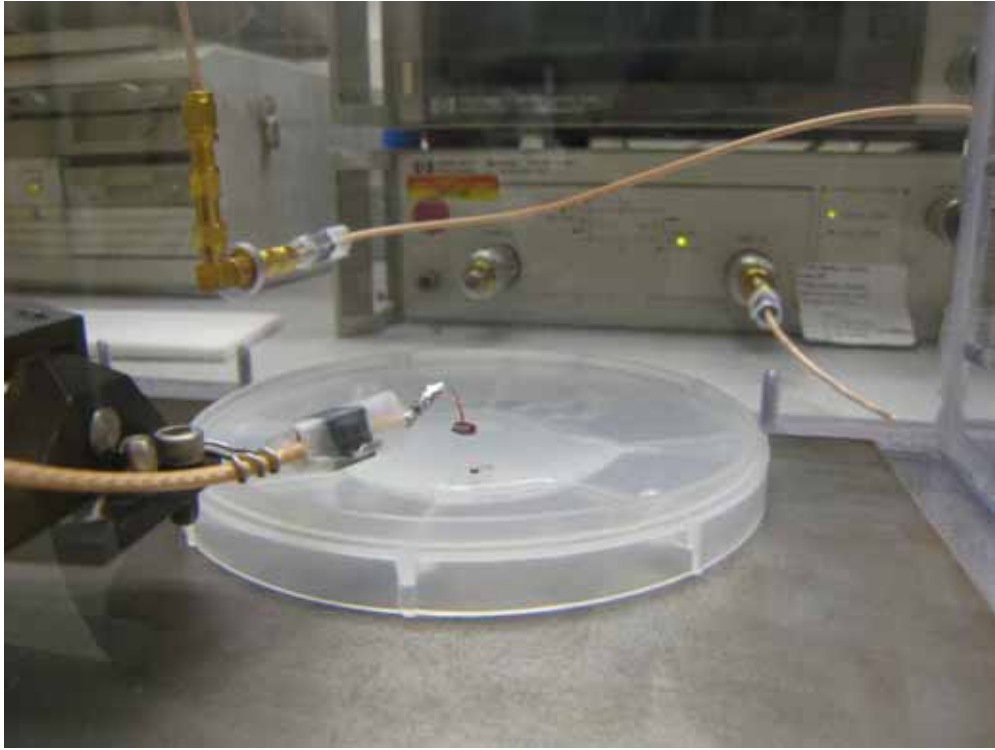


**Fig. 73. The remote measurement with sensor #1 immersed into a small portion of water.**

## APPENDIX A. METHOD OF MOMENTS MATLAB CODE

```

%% [Numerical Capacitance Calculation for Circular Membrane Structures Under
%% Different Pressure Condition by Method of Moments (MoM)] by Haibo Cao
%% and Robert J. Weber
%% Unpublished Work Copyright © 2006
%% Iowa State University Research Foundation, Inc.

clear all;
close all;
clc;

m = 55; %Number of cells
maxcell = m+1; %Number of Edges
radius = 50e-6; %Radius of the plate, a (meter)
delta = radius/m; %a/m
height = 1e-6; %Height of the cavity at outer edge, h
%(meter)

th = 1.12e-6; %Thickness of the plate, t (meter)
s = 0.005e-6; %Small distance
pressure = 800; %Absolute pressure on the plate, P0 (torr)
pressure = pressure*1.33324e2; %Unit Converting from mmHg to Pa
po = 13.3/16; %Charge ring & calculation point position
%between edges

Pmax = 3*pressure*radius^2/(4*th^2); %Maximum Pressure
Pmax

%%%%%%%%%%%%%%%%%%%%%%%%%%%%%%%%%%%%%%%%%%%%%%%%%%%%%%%%%%%%%%%%%%%%%%%%%
%%Mechanical Property of Material%%%%%%%%%%%%%%%%%%%%%%%%%%%%%%%%%%%%%%%%%%%%%%%%%%%%%%%%%%%%%%%%%%%%%%%%%
E = 120e9; %Young's Modulus of Poly, E (Pa)
v = 0.22; %Poisson's ratio of Poly, v
D = E*th^3/(12*(1-v^2)); %Flexural Rigidity of Thin plate;

%%%%%%%%%%%%%%%%%%%%%%%%%%%%%%%%%%%%%%%%%%%%%%%%%%%%%%%%%%%%%%%%%%%%%%%%%
%%Electrical Property of Material%%%%%%%%%%%%%%%%%%%%%%%%%%%%%%%%%%%%%%%%%%%%%%%%%%%%%%%%%%%%%%%%%%%%%%%%%
e0=8.854e-12; %Permittivity of free space (F/m)
coef = 4*pi*e0;

%%%%%%%%%%%%%%%%%%%%%%%%%%%%%%%%%%%%%%%%%%%%%%%%%%%%%%%%%%%%%%%%%%%%%%%%%
%%Mechanical Deflection With Respect to Pressure%%%%%%%%%%%%%%%%%%%%%%%%%%%%%%%%%%%%%%%%%%%%%%%%%%%%%%%%%%%%%%%%%%%%%%%%%
phi = 0:2*pi/m:2*pi; %Divided along angle
i = 0:1/m:1; %Divided along radius
w = pressure*((radius*i).^2-radius.^2).^2/(64*D); %Deflection for edges
t = pressure*((radius*i+delta*po).^2-radius.^2).^2/(64*D); %Deflection
%for charge rings and calculation points
hw = height-w; %Edges on the Z axis

```

```

ht = height-t;                                %Charge rings and calculation points on the
                                                %Z axis
r = radius*i;                                  %Edges

x = zeros(maxcell);                            %Position of each display cell
y = zeros(maxcell);
z = zeros(maxcell);

for i = 1:1:maxcell
    for j = 1:1:maxcell
        x(i,j) = r(i)*cos(phi(j));
        y(i,j) = r(i)*sin(phi(j));
        z(i,j) = hw(i);
    end
end
figure
mesh(x, y, z, 'MarkerSize', 50)
axis([-50e-6 50e-6 -50e-6 50e-6 0 1e-6]);
xlabel('Radius(m)');
ylabel('Radius(m)');
zlabel('Height(m)');

figure
mesh(x, y, z, 'MarkerSize', 50)
axis([-50e-6 50e-6 -50e-6 50e-6 0 1e-6]);
view([0 90 0]);
xlabel('Radius(m)');
ylabel('Radius(m)');
zlabel('Height(m)');

M = zeros(m);                                  %Moment matrix
Sigma = zeros(m,1);                            %Charge density matrix
V = coef.*ones(m,1);                          %Equal voltage potential

for i = 1:1:m
    for j = 1:1:m
        a = r(i)+delta*po;
        b = r(j)+delta*po;
        e = ht(i);
        f = ht(j);
        k = 2*(a*b/(e^2+a^2-2*e*s+s^2-2*e*f+2*f*s+f^2+2*a*b+b^2))^(1/2);
        l = real(mfun('EllipticK',k));
        p = 2*(a*b/(2*a*b+e^2+a^2+2*e*s+s^2+2*f*e+2*f*s+f^2+b^2))^(1/2);
        q = real(mfun('EllipticK',p));
    end
end

```

```

M(i,j) = b*(...
(4*((a^2+b^2-2*a*b+f^2+e^2-2*e*f-2*e*s+2*f*s+s^2)/(e^2+a^2-2*e*s+s^2-2*e*f+2*f*s+f
^2+2*a*b+b^2))^(1/2)*l/(a^2+b^2-2*a*b+f^2+e^2-2*e*f-2*e*s+2*f*s+s^2)^(1/2))-...
(4*((a^2+b^2-2*a*b+e^2+f^2+2*f*e+2*f*s+2*e*s+s^2)/(2*a*b+e^2+a^2+2*e*s+s^2+2*f*
e+2*f*s+f^2+b^2))^(1/2)*q/(a^2+b^2-2*a*b+e^2+f^2+2*f*e+2*f*s+2*e*s+s^2)^(1/2))...
);
end
end

```

```

Q = 0;
R = inv(M);
Sigma = R*V;

```

```

for n=1:1:m
    A = Sigma(n,1)*2*pi*(r(n)+delta*po);
    Q = Q+A;
end                                     %Calculate total charge (C)
C = 2*Q                                 %Calculate capacitance (F)

```

```

Figure                                  %Plot Charge Density
plot (Sigma(1:m,1));
xlabel('Radius(um)');
ylabel('Charge Density(C/m)');

```

## APPENDIX B. INTRAOCULAR PRESSURE (IOP) SENSOR

### FABRICATION FLOW

Wafer Material	Material:	4" N <sup>+</sup> <100>
Measure Wafer Thickness	Equipment: Recipe:	Fowler Ultra Digit Mark IV Record thickness in um
Piranha Clean	Equipment: Recipe:	Wet Bench Piranha Solution (H <sub>2</sub> SO <sub>4</sub> :H <sub>2</sub> O <sub>2</sub> =10:1) 120°C 10min Rinse 3 times in DI water, spin and dry
RCA Clean	Equipment: Recipe:	Wet Bench SC1: H <sub>2</sub> O:NH <sub>4</sub> OH:H <sub>2</sub> O <sub>2</sub> =8:1:1 80°C 15min rinse HF Dip: H <sub>2</sub> O:HF=10:1 Room temp 15sec rinse SC2: H <sub>2</sub> O:HCL:H <sub>2</sub> O <sub>2</sub> =6:1:1 80°C 15min Rinse 3 times in DI water, spin and dry
Conductivity Measurement	Equipment: Recipe:	4-Point-Probe ~0.3Ω/□
Si <sub>3</sub> N <sub>4</sub> LPCVD	Equipment: Recipe:	LPCVD Tube 843°C 300mTorr DCS 20sccm, NH <sub>3</sub> 80sccm 130min
Si <sub>3</sub> N <sub>4</sub> thickness Measurement	Equipment: Recipe:	Nanospec ~5100A
Prebake/HMDS	Equipment: Recipe:	Hotplate/Teflon Box 115°C 2min HMDS vapor 3min
Futurrex NR7-1500P	Equipment: Recipe:	Spinner 3000/1500/30 ~1.2um
Soft Bake	Equipment: Recipe:	Hotplate 150°C 90sec
Photolithography of Mask #1 (substrate electrode)	Equipment: Recipe:	Karl Suss MA-6 g-line, Hard Cont Dose ~150mJ
Post Bake/Develop	Equipment: Recipe:	Hotplate/Teflon Box 105°C 1min RD6 10sec Rinse with DI water and dry w/N-gun
Residual PR Clean	Equipment: Recipe:	Asher 150W, 150 O <sub>2</sub> , 1min

RIE/PR Removal	Equipment: Recipe:	STS Plasma Etcher PJSNITD: Ar 50sccm, CF <sub>4</sub> 40sccm, SF <sub>6</sub> 10sccm, 75mTorr, RF Power 150W 8min(~777A/min) O <sub>2</sub> clean 5min Acetone-Methanol-IPA Rinse/Dry
Piranha Clean	Equipment: Recipe:	Wet Bench Piranha Solution (H <sub>2</sub> SO <sub>4</sub> :H <sub>2</sub> O <sub>2</sub> =10:1) 120°C 10min Rinse 3 times in DI water, spin and dry
PSG Deposition	Equipment: Recipe:	LPCVD Tube 425°C 300mTorr O <sub>2</sub> 90sccm, SiH <sub>4</sub> 70sccm 118sccm %15 PH <sub>3</sub> in H <sub>2</sub> flow 2hr
PSG thickness Measurement	Equipment: Recipe:	Nanospec ~20000A Uniformity: ~15% in wafer, ~4% in boat
PSG Annealing	Equipment: Recipe:	Tylan Furnace 950°C 2sccm N <sub>2</sub> 1hr
PSG thickness Measurement	Equipment: Recipe:	Nanospec ~shrinks 1%
Prebake/HMDS	Equipment: Recipe:	Hotplate/Teflon Box 105°C 2min HMDS vapor 3min
Shipley 1818	Equipment: Recipe:	Spinner 3000/3000/30 ~2.1um
Soft Bake	Equipment: Recipe:	Hotplate 115°C 2min
Photolithography of Mask #2 (sacrificial layer and etching channels)	Equipment: Recipe:	Karl Suss MA-6 g-line Soft Cont Dose ~102mJ
Post Bake/Develop	Equipment: Recipe:	Hotplate/Teflon Box 105°C 1min 351:H <sub>2</sub> O(1:5) 1min Rinse with DI water and dry w/N-gun
Residual PR Clean	Equipment: Recipe:	Asher 150W, 150 O <sub>2</sub> , 2min
Hard Bake	Equipment: Recipe:	Oven 120°C 30min

BOE/PR Removal	Equipment: Recipe:	Teflon Box 10:1/13min/~2100A/min Acetone-Methanol-IPA Rinse/Dry
Piranha Clean	Equipment: Recipe:	Wet Bench Piranha Solution (H <sub>2</sub> SO <sub>4</sub> :H <sub>2</sub> O <sub>2</sub> =10:1) 120°C 10min Rinse 3 times in DI water, spin and dry
Phos-poly Deposition	Equipment: Recipe:	LPCVD Tube N+/regular stack up 66/48/66/48/66min N+: 640°C, 250mTorr 4sccm PH <sub>3</sub> , 124.8sccm SiH <sub>4</sub> Regular: 616°C, 250mTorr 124.8sccm SiH <sub>4</sub>
Poly thickness Measurement	Equipment: Recipe:	Nanospec ~16000A
Conductivity Measurement	Equipment: Recipe:	4-Point-Probe ~240Ω/□
Poly stress measurement	Equipment: Recipe:	FSM 900TC ~-374MPa
Poly Annealing	Equipment: Recipe:	RTA 1100°C 10SLPM HiN <sub>2</sub> 1min
Poly stress measurement	Equipment: Recipe:	FSM 900TC ~-140MPa
Conductivity Measurement	Equipment: Recipe:	4-Point-Probe ~33.6Ω/□
Prebake/HMDS	Equipment: Recipe:	Hotplate/Teflon Box 105°C 2min HMDS vapor 3min
Shipley 1818	Equipment: Recipe:	Spinner 3000/3000/30 ~2.1um
Soft Bake	Equipment: Recipe:	Hotplate 115°C 2min
Photolithography of Mask #3 (membrane structures)	Equipment: Recipe:	Karl Suss MA-6 g-line Soft Cont Dose ~102mJ
Post Bake/Develop	Equipment: Recipe:	Hotplate/Teflon Box 105°C 1min 351:H <sub>2</sub> O(1:5) 1min Rinse with DI water and dry w/N-gun
Residual PR Clean	Equipment: Recipe:	Asher 150W, 150 O <sub>2</sub> , 2min

Hard Bake	Equipment: Recipe:	Oven 120°C 30min
DRIE/PR Removal	Equipment: Recipe:	Deep Trench Plasma Etcher Bosch 8loops Acetone-Methanol-IPA O <sub>2</sub> plasma 5min
Sacrificial Etching	Equipment: Recipe:	Teflon Box HF Vapor 15min 10:1 BOE 1min Methanol-IPA rinse 3times
CPD	Equipment: Recipe:	Tousimis Model 915B 1/4 chamber full of IPA, 15min purge time
PECVD SiO <sub>2</sub> Deposition	Equipment: Recipe:	Plasmatherm 340 340°C, 900mTorr, 90min 200 sccm 2% SiH <sub>4</sub> in He, 450sccm N <sub>2</sub> O Power 20 Watts, ~353.62 A/min
SiO <sub>2</sub> thickness Measurement	Equipment: Recipe:	Nanospec ~31825A
Prebake/HMDS	Equipment: Recipe:	Hotplate/Teflon Box 105°C 2min HMDS vapor 3min
SPR 220-4.5	Equipment: Recipe:	Spinner 2000/500/90 ~6um
Soft Bake	Equipment: Recipe:	Hotplate 115°C 90sec/30sec ramp up
Photolithography of Mask #4 (seal rings)	Equipment: Recipe:	Karl Suss MA-6 g-line Soft Cont Dose ~432mJ
Hold	Equipment: Recipe:	NA Hold for 1hr allowing water diffuse
Post Bake/Develop	Equipment: Recipe:	Hotplate/Teflon Box 105°C 2min MF-CD-26 90sec Rinse with DI water and dry w/N-gun
Residual PR Clean	Equipment: Recipe:	Asher 150W, 150 O <sub>2</sub> , 2min
Hard Bake	Equipment: Recipe:	Hotplate 105°C 5min
RIE	Equipment: Recipe:	STS Plasma Etcher PJNITD1 10min PJOXID 6min

BOE/PR Removal	Equipment: Recipe:	Teflon Box 10:1/7min/~1500A/min Acetone-Methanol-IPA 5min O <sub>2</sub> Plasma
Al Sputtering	Equipment: Recipe:	Perkin Elmer 2400 Al (with 2% Si) 6 mTorr 10sccm Ar ~3rpm table rotation, 5 kW power 2min ramp 2min pre-sputter (@ 5 kW) 34min, 900A/min
Conductivity Measurement	Equipment: Recipe:	4-Point-Probe ~0.0252Ω/□
Al Annealing	Equipment: Recipe:	RTA 400°C 30sec
Conductivity Measurement	Equipment: Recipe:	4-Point-Probe ~0.0213Ω/□
Prebake/HMDS	Equipment: Recipe:	Hotplate/Teflon Box 105°C 2min HMDS vapor 3min
Shipley STR1045	Equipment: Recipe:	Spinner 1500/500/43 ~7.8um
Soft Bake	Equipment: Recipe:	Oven 105°C 30min
Photolithography of Mask #5 (contact rings)	Equipment: Recipe:	Karl Suss MA-6 g-line Soft Cont Dose ~444mJ
Develop	Equipment: Recipe:	Teflon Box 351:H <sub>2</sub> O(1:5) 3min Rinse with DI water and dry w/N-gun
Residual PR Clean	Equipment: Recipe:	Asher 200W, 150 O <sub>2</sub> , 15sec
Hard Bake	Equipment: Recipe:	Hotplate 105°C 1min
Al Etching/PR Removal	Equipment: Recipe:	Glass Box H <sub>3</sub> PO <sub>4</sub> :HNO <sub>3</sub> :HAc:2H <sub>2</sub> O=16:1:1, 50°C 6min Acetone-Methanol-IPA Rinse/dry

## BIBLIOGRAPHY

- [1] H. Quigley, "Number of people with Glaucoma worldwide," *Br. J. Ophthalmol.*, vol. 80, no. 5, pp. 389–393, 1996.
- [2] L. Titcomb, "Treatment of glaucoma: Part 1," *Pharmaceutical J.*, vol. 263, no. 7060, pp. 324–329.
- [3] J. M. Tielsch, J. Katz, K. Singh, H. A. Quigley, J. D. Gottsch, J. Javitt, and A. Sommer, "A population-based evaluation of glaucoma screening: The Baltimore eye survey," *Amer. J. Epidemiology*, vol. 134, no. 10, pp. 1102–1110, 1991.
- [4] R. Puers, "Capacitive sensors: When and how to use them," *Sens. Actuators A*, vol. 37-38, pp. 93-105, 1993.
- [5] C. C. Collins, "Miniature passive pressure transducer for implanting in eye," *IEEE Trans. Bio-Med. Eng.*, vol. BME-14, no. 2, pp. 74-83, Apr. 1967.
- [6] L. Rosengren, P. Rangsten, Y. Backlund, B. Hok, B. Svedbergh, and G. Selen, "A system for passive implantable pressure sensors," *Sens. Actuators A*, vol. 43, pp. 55–58, 1994.
- [7] R. Puers, G. Vandevoorde, and D. De Bruyker, "Electrodeposited copper inductors for intraocular pressure telemetry," *J. Micromech. Microeng.*, vol. 10, pp. 124–129, 2000.
- [8] J. Coosemans, M. Catrysse, and R. Puers, "A readout circuit for an intraocular pressure sensor," *Sens. Actuators A*, vol. 110, pp. 432–438, 2004.
- [9] J. Abita, B. G. Carkhuff, R. Frankel, "Method for monitoring intraocular pressure using a passive intraocular pressure sensor and patient worn monitoring recorder," US Patent 6579235 B1, 2003.

- [10] Akar, T. Akin, and K. Najafi, "A wireless batch sealed absolute capacitive pressure sensor," *Sens. Actuator A*, vol. 95, pp. 29–38, 2001.
- [11] P. Chen, D. Rodger, S. Saati, M. S. Humayun, and Y. Tai, "Implantable parylene-based wireless intraocular pressure sensor," *MEMS 2008. IEEE 21st International Conference on*, pp. 58-61, 2008.
- [12] K. Petersen, G. T. A. Kovacs, T. G. Ryan, L. G. Partamian, D. A. Lee, "Implantable continuous intraocular pressure sensor," US Patent 6939299 B1, 2005.
- [13] G. E. Waters Jr., R. L. Thommen, "Intraocular pressure sensor," US Patent 4922913, 1990.
- [14] M. Leonardi, S. Metz, D. Bertrand, P. Leuenberger, "Intraocular pressure recording system," US Patent 7137952 B2, 2006.
- [15] H. Cao, R. Weber, "Vapor HF sacrificial etching for phosphorus doped polycrystalline silicon membrane structures," *Electro/Information Technology, 2008. IEEE International Conference on*, Vol.(Issue) 18-20, pp. 289-293, May 2008.
- [16] A. C. Ugural, *Stresses in plates and shells*, Boston, WCB/McGraw-Hill, 1999.
- [17] W. N. Sharpe Jr., B. Yuan, R. Vaidyanathan, and R. L. Edwards, "Measurements of Young's modulus, Poisson's ratio, and tensile strength of polysilicon," in *Proc. of the IEEE on the 10th Annual International Workshop on Micro Electro Mechanical Systems. An Investigation of Micro Structures, Sensors, Actuators, Machines and Robots*, Nagoya, Japan, Jan. 1997, pp. 26–30.
- [18] P. Li, Design and fabrication of a MEMS passive pressure sensor, Master's Thesis in Iowa State University, 2006.

- [19] E. Weber, *Electromagnetic theory; static fields and their mapping*, New York, Wiley, 1965, ch. 4, sec. 12.
- [20] R. J. Weber, *Introduction to microwave circuits: radio frequency and design applications*, Wiley-IEEE Press, 2001, ch. 2-4.
- [21] J. N. Burghartz, A. E. Ruehli, K. A. Jenkins, M. Soyuer, and D. Nguyen-Ngoc, "Novel substrate contact structure for high-Q silicon-integrated spiral inductors," *Tech. Dig. Int. Electron Devices Meeting (IEDM)*, pp. 55-58, 1997.
- [22] J. N. Burghartz and D.C. Edelstein, "Spiral inductors and transmission lines on silicon technology using copper-damascene interconnects and low-loss substrates," *IEEE Trans. Microwave Theory Tech.* 45 (1997), pp. 1961–1968.
- [23] R. C. Jaeger, *Introduction to microelectronic fabrication*, 2<sup>nd</sup> Edition, Prentice Hall, 2002, ch. 11.
- [24] A. Sherman, *Chemical vapor deposition for microelectronics: principles, technology and applications*, Noyes Publications, 1987, ch. 3.
- [25] C. Liu, *Foundations of MEMS*, Pearson Prentice Hall, 2006, ch. 11.
- [26] G. Voskerician, M.S. Shive, R.S. Shawgo, H. von Recum, J.M. Anderson, M.J. Cima and R. Langer, "Biocompatibility and biofouling of MEMS drug delivery devices," *Biomaterials* 24:11, Elsevier, Amsterdam Netherlands (2003), pp. 1959–1967.
- [27] W. Sharpe Jr., K. Jackson, K. Hemker and Z. Xie, "Effect of specimen size on Young's modulus and fracture strength of polysilicon," *J Microelectromech Syst* 10 (2001), pp. 317–326.
- [28] J. M. Bustillo, R. T. Howe, and R. S. Muller, "Surface micromachining for microelectromechanical systems," *Proc. of the IEEE*, vol. 86, pp. 1552-1574, 1998.

- [29] C. S. Lee, J. H. Lee, C. A. Choi, K. No and D.M. Wee, "Effects of phosphorus on stress of multi-stacked polysilicon film and single crystalline silicon," *J. Micromechan. Microeng.* 9 (1999), pp. 252–263.
- [30] E. Yoshikawa, M. Tsugai, M. Horikawa, H. Otani, S. Hamada, "Influence of RTA parameters on residual stress and stress gradient of multilayered LPCVD polysilicon film," *Proc. 15th Conference Micro-Electro-Mechanical-System*, 2002, pp. 451–454.
- [31] A. Witvrouw, B. Du Bois, P. De Moor, A. Verbist, C. Van Hoof, H. Bender, and K. Baert, "A comparison between wet HF etching and vapor HF etching for sacrificial oxide removal," *Proc. SPIE Micromachining and Microfabrication Process Technology VI*, Sept.2000, vol. 4174, pp. 130-141.
- [32] H. Dudaicevs, M. Kandler, Y. Manoli, W. Mokwa and E. Spiegel, "Surface micromachined pressure sensors with integrated CMOS read-out electronics," *Sensors and Actuators A*, vol. 43(1-3), pp. 157-163, May 1994.
- [33] R. J. Weber, "RF/microwave sensed cantilevers, diaphragms, and tactile sensors for passive and active sensor systems," *Life Science Systems and Application Workshop, 2006. IEEE/NLM*, Maryland, July 2006, pp. 1-2.
- [34] D. J. Monk, D. S. Soane, and R. T. Howe, "Hydrofluoric acid etching of silicon dioxide sacrificial layers, I. Experimental Observation," *J. Electrochem Soc.*, vol. 141(1), pp. 264-269, Jan. 1994.
- [35] T. A. Lober, and R. T. Howe, "Surface micromachining processes for electrostatic motor fabrication," *3rd IEEE Solid-State Sensors and Actuators Workshop*, Hilton Head, S.C., Jun. 1988, pp. 59-62.

- [36] J. A. Walker, K. J. Gabriel, and M. Mehregany, "Mechanical integrity of polysilicon films exposed to hydrofluoric acid solutions," *J. Electron. Mater.*, vol. 20, pp. 665-670, 1991.

## ACKNOWLEDGEMENTS

First and foremost, I would like to thank Dr. Weber for his guidance, patience and support throughout this research and the writing of this thesis, also for his education in RF circuit design area. I would also like to thank Dr. Hamouche for his suggestion during the device measurement process. I would also like to thank my committee members for their efforts and contributions to this work. Last but not least, I would like to thank Mr. Tony Whipple, Mr. Mark Fisher, and Mr. Kevin Roberts for their great help during the fabrication work.